

Pulsed laser ablation and micromachining of 4H and 6H SiC wafers for high-temperature MEMS sensors

by

Saurabh Gupta

A thesis submitted to the graduate faculty
in partial fulfillment of the requirements for the degree of
MASTER OF SCIENCE

Major: Mechanical Engineering

Program of Study Committee:
Palaniappa A Molian, Major Professor
Pranav Shrotriya
Matthew Frank

Iowa State University

Ames, Iowa

2008

Copyright © Saurabh Gupta, 2008. All rights reserved

TABLE OF CONTENTS

ACKNOWLEDGEMENTS	v
CHAPTER 1 GENERAL INTRODUCTION	1
Introduction	1
Thesis Organization	2
CHAPTER 2 A REVIEW OF LASER MICROSCALE PROCESSING OF SILICON CARBIDE	3
Abstract	3
1. Introduction	3
1.1 Properties of Silicon Carbide	4
1.2 Overview of SiC Laser Processing	6
2. Additive Laser Processing	13
2.1 Doping and Annealing of Silicon Carbide	13
2.1.1 <i>In situ</i> laser doping of Silicon Carbide	14
2.1.2 Annealing of Silicon Carbide	15
2.2 Metallization of SiC Substrates	17
2.3 Pulsed Laser Deposition of Silicon Carbide Thin Films	18
2.4 Nanoparticle formation	19
3. Subtractive Laser Processing	21
4. Conclusion	25
Acknowledgement	26
References	26

CHAPTER 3 EXCIMER LASER ABLATION AND MICROMACHINING OF SINGLE

CRYSTAL 4H-SiC AND 6H-SiC	37
Abstract	37
1. Introduction	38
2. Experimental Details	40
3. Results and Discussion	43
3.1 Ablation Characteristics	43
3.2 Machining Results	61
4. Conclusion	65
Acknowledgement	66
References	66

CHAPTER 4 PICOSECOND PULSED LASER ABLATION AND MICROMACHINING

OF 4H-SiC WAFERS	72
Abstract	72
1. Introduction	73
2. Experimental Details	75
3. Results and Discussion	77
3.1 Ablation	77
3.2 Micromachining	81
4. Conclusions	84
Acknowledgement	85
References	85

CHAPTER 5 FINITE ELEMENT ANALYSIS OF SINGLE CRYSTAL 6H-SiC	
DIAPHRAGM FOR HIGH-TEMPERATURE MEMS PRESSURE SENSORS	88
Nomenclature	88
1. Introduction	88
2. Excimer Laser Micromachining	91
3. Material Properties	93
4. Mathematical Formulation of the Problem	94
4.1 Stress-Strain Relationship:	96
5. FEM Methodology	97
6. Analysis	98
6.1 Effect of Pressure and Temperature	101
7. Conclusion	103
Acknowledgement	104
References	104
CHAPTER 6 GENERAL CONCLUSION	107

ACKNOWLEDGEMENTS

I would like to thank Dr. Molian, my major professor, for his support and encouragement all through the course of my study at Iowa State University. His scholarship, vast knowledge, and openness to my ideas have helped me in believing myself and given me the mental tenacity to focus on my research work that will also help me a long way in my future career prospects. His guidance has been invaluable without which this work would not have been possible. I am also grateful to Dr. Shrotriya and Dr. Frank for consenting to be on my committee and helping me with their comments and suggestions whenever I have bothered them. Finally, I want to thank my parents for giving me the means and opportunity to come to United States to pursue further education, and my friends for all their moral support.

CHAPTER 1 GENERAL INTRODUCTION

Introduction

Silicon Carbide (SiC) possesses excellent material properties that make it ideal for fabricating Micro-Electro-Mechanical-System (MEMS) devices needed in variety of harsh environments. These properties include, but are not limited to, wider bandgap, higher breakdown voltage and Young's modulus, and much higher heat conductivity and melting temperature than silicon. Of all the MEMS based devices, pressure sensors are in a growing demand in numerous industries as transportation (automobile, diesel and aerospace), energy (power generation, petrochemical refineries and oil & gas industries), and environmental (HVAC systems).

SiC exist in number of different forms (more than 200 polytypes are known today) but only three types -- 3C-SiC, 4H-SiC, and 6H-SiC could be grown in single crystalline form suitable for use in microelectronics and MEMS industry. Amongst these three polytypes, single crystal 4H-SiC and 6H-SiC wafers are commercially available (with diameters ranging from 25 mm to 100 mm) manufactured by Cree Inc. (NC, USA). On the other hand, defect-free single crystal 3C-SiC wafers are difficult to obtain due to the rigid process control requirements. Consequently, the performance and reliability of SiC MEMS devices fabricated by laser micromachining strongly depend on the material properties used.

Laser micromachining has a great potential as a MEMS fabrication technique because of its material flexibility and 3D capabilities. Conventional fabrication methods as reactive ion etching (RIE), electron cyclotron resonance (ECR), deep reactive ion etching (DRIE) cannot easily reach the goal due to high hardness and chemical stability of SiC.

Moreover, these methods suffer from poor etch selectivity and slow etch rate, preventing large volume production of SiC MEMS devices at low cost. By using controlled laser variables as wavelength, pulse width, repetition rate, beam fluence (energy per unit area) etc. high-quality microstructures can be fabricated easily in a much lesser time frame.

The purpose of this research is to scientifically investigate the ablation behavior of single crystal 4H-SiC and 6H-SiC to improve the manufacturability and high-temperature performance of SiC based MEMS pressure sensors using laser applications. The ablation characteristics of both the polytypes were studied with a 248 nm excimer laser (pulse width 23 ns) and micromachining results were presented. The study shows the possibility of these devices capable of operating in harsh environments.

Thesis Organization

This thesis is organized into three papers, a chapter on finite element analysis and a chapter on conclusions. The first paper deals with a literature review of various laser microscale processing techniques of SiC for microelectronics and MEMS applications. The second paper deals with excimer laser ablation and micromachining of single crystal 4H and 6H SiC presenting their characteristic ablation behavior that can be categorized into three distinct regimes, and visible surface modifications indicating the extent of thermal mechanisms in the ablation process. The third paper deals with the ablation study and micromachining of single crystal 4H-SiC using ultrashort picosecond laser demonstrating their efficacy in fabricating much better micromachined features in comparison with other pulsed lasers. The last chapter deals with the details on finite element analysis (FEA) of single crystal 6H-SiC diaphragm for high-temperature MEMS pressure sensors.

CHAPTER 2 A REVIEW OF LASER MICROSCALE PROCESSING OF SILICON CARBIDE

A paper submitted to *Journal of Laser Applications*

Ben Pecholt, Saurabh Gupta, and Pal Molian

Abstract

A review of various laser techniques for microscale processing of SiC for microelectronics and MEMS applications is presented. SiC is an excellent material for harsh environments due to its outstanding mechanical, thermal, and chemical properties. However, its extreme stability and inert properties created difficulties in conventional microfabrication methods to fabricate devices and has offered an opportunity for the exploration of laser processing as an alternative. Many aspects of laser processing of SiC are investigated across the globe using wavelengths ranging from 193 to 1064 nm and pulse widths from nanoseconds to femtoseconds with results indicating that lasers can become successful tools for SiC microprocessing in the future. This paper is categorized into additive and subtractive laser techniques in order to facilitate a discussion of all processes used for fabricating microdevices.

1. Introduction

The success of microelectronics has been followed by rapid development in MicroElectroMechanical Systems (MEMS) resulting in a wide array of device applications which impact our daily life. In particular, an increased demand for devices capable of functioning at high temperatures and in harsh environments accounts for the emergence of Silicon Carbide (SiC) as a preferred material. The continued interest of SiC is primarily due

to many advancements in deposition and crystalline growth techniques and its ability to be used at high temperature in highly erosive or corrosive environments [1-4]. Many areas of industry would benefit from implementation of SiC MEMS sensors including: oil drilling, avionics and spacecraft systems, and engine, turbine, and industrial process control. SiC has already been used for high temperature pressure sensors [5-12], accelerometers [13], micromotors [14, 15], and CMOS compatible devices [6]. SiC is also of interest for high power electronics and RF and microwave applications [16, 17]. Some of the more notable properties of SiC are the high saturation drift velocity, high bandgap, high thermal stability, high thermal conductivity, low diffusion rates, and chemical inertness. Unfortunately some of these properties are also barriers to the fabrication of microelectronics and MEMS devices. Major challenges that still exist include: dielectric deposition, etching, oxidation, metallization, and doping. Laser processing has been explored in these areas as both additive (annealing, deposition, surface alteration, and doping) and subtractive (ablation) processes. Here we provide a review of SiC laser processing relevant to these areas with the expectation that continued development will lead to a proliferation of SiC devices.

1.1 Properties of Silicon Carbide

Over 200 polytypes of the SiC crystal structure are possible with different stacking of the Si-C bilayers in the [0001] direction [18]. The polytypes are named according to the configuration of Si-C double layers in the unit cell with the designation C, H, or R indicating cubic, hexagonal, or rhombohedra symmetry. However, only the 3C, 4H, and 6H polytypes can be grown as single crystal SiC and therefore are of practical importance for microelectronics and MEMS applications. 4H and 6H substrates are commercially available

as wafers up to 100 mm diameter. Work is still progressing for 3C wafers, however 3C-SiC has the versatility of being deposited via Chemical Vapor Deposition (CVD). 3C-SiC can be deposited as polycrystalline SiC (poly-SiC) on SiO₂ and Si₃N₄ substrates [19] or can be grown as a heteroepitaxial film on Si wafers [20-22]. Similarly, amorphous SiC films can be deposited using CVD techniques. Properties vary significantly between polytypes [23] such as carrier mobility and electronic bandgap. Only 3C-SiC exhibits anisotropic properties and has higher saturation velocity, and lower band gap (2.3 eV) compared to 4H-SiC (3.2 eV) and 6H-SiC (3.0 eV) [24]. Due to the difficulties in growing bulk single crystalline 3C-SiC, it has yet to be made commercially available, but ongoing research has led to limited supply of bulk single crystal wafers with polished surfaces [25]. In terms of bulk single crystals 4H-SiC is typically favored for microelectronics applications over 6H-SiC because of its higher carrier mobility. Electronic properties of SiC compared to silicon are listed in Table 1.

Table 1 Electronic properties of silicon and SiC polytypes

Property	Si	3C-SiC	4H-SiC	6H-SiC
Band Gap (eV)	1.12 [24]	2.36 [26]	3.23 [24, 26, 27]	3.0 [24, 26]
Breakdown field (V cm ⁻¹)	3 x 10 ⁵ [28]	10 ⁶ [26]	(3.5) x 10 ⁶ [26]	(3.5) x 10 ⁶ [26]
Static Dielectric Constant	11.9 [24]	9.72 [24, 26]	Typically values for 6H used [26]	$\frac{\perp}{\text{c-axis}}$ 9.7 \parallel c-axis 10 [26]
Electron Mobility @ N _d = 10 ¹⁶ cm ⁻³ (cm ² V ⁻¹ s ⁻¹)	1350 [24]	1000 [24]	$\frac{\perp}{\text{c-axis}}$ 950 \parallel c-axis 1150 [24]	$\frac{\perp}{\text{c-axis}}$ 500 \parallel c-axis 100 [24]
Hole Mobility @ N _d = 10 ¹⁶ cm ⁻³ (cm ² V ⁻¹ s ⁻¹)	480 [24]	40 [24]	120 [24]	90 [24]
Saturation Velocity (10 ⁷ cm s ⁻¹)	1.0 [24]	2.5 [24]	2.0 [24]	2.0 [24]

SiC has also been attractive for MEMS applications due to its favorable mechanical properties including high wear resistance, stiffness, and hardness; these properties have already led to the widespread use of SiC in industrial applications such as tools and abrasives. SiC is comparable to other hard materials such as diamond and Al₂O₃. Its hardness on the Moh's scale (9) is similar to that of Al₂O₃ (9) [1]. In terms of Knoop hardness SiC (2480 kg/mm²) is also comparable to Al₂O₃ (2100 kg/mm²) and is approximately three times greater than silicon [1]. In addition to its ability to be used in harsh conditions, SiC offers greater reliability in MEMS devices relative to silicon due to the lower surface reactivity. The mechanical properties of SiC compared to silicon are summarized in Table 2.

Table 2 Mechanical and thermal properties of silicon and SiC polytypes

Property	Si	3C-SiC	4H-SiC	6H-SiC
Young's Modulus (GPa)	130 [28]	433 [29]	-	-
Lattice Parameter (Å)	5.43 [24]	4.36 [24,27]	a 3.08 [24, c 10.1 27]	a 3.1 [24, c 15 27]
Density (g cm ⁻¹)	2.3 [24]	3.2 [24,27]	3.2 [24]	3.2 [24, 27]
Melting Point (°C)	1420 [24]	2830 [24]	2830 [24]	2830 [24]
Moh's Hardness	6.5	9 [24]	9 [24]	9 [24]
Bulk Modulus (dyn cm ⁻²)	9.78 x10 ¹⁰ [30]	2.5 x10 ¹² [26]	2.2 x 10 ¹² [26]	2.2 x10 ¹² [26]
Debye Temperature (K)	~650 [30]	1200 [27]	1300 [26]	1200 [26]
Thermal Conductivity (W cm ⁻¹ C ⁻¹)	1.5 [24]	3.6 [26]	3.7 [26]	4.9 [26]
Thermal diffusivity (cm ² s ⁻¹)	0.9 [28]	1.6 [26]	1.7 [26]	2.2 [26]
Thermal Expansion (10 ⁻⁶ C ⁻¹)	2.6 [24]	3.8 [24]	-	⊥ c-axis 4.3 [26] ∥ c-axis 4.7 [26]

1.2 Overview of SiC Laser Processing

Laser micromachining has several advantages over conventional microfabrication techniques due to its minimization of processing steps, its ability to be used as a CNC prototype tool, and scalability through serial or batch processing. Lasers have been explored as tools for SiC processing since the early 1980s, but yet to achieve widespread use for microelectronics and MEMS applications. Virtually every laser applicable to microfabrication has been explored: traditional excimer, Nd:YAG, and CO₂ [31, 32, 33], the more novel lasers such as the N₂ [34], Ar⁺ [35], Cu Vapor [36, 37] and the emergent picosecond [38] and femtosecond lasers [25, 39-46]. Table 3 summarizes the laser types and their applications for SiC processing.

Nanosecond pulsed UV lasers such as excimer and frequency tripled and quadrupled Nd:YAG are the most widely used [25, 33, 45, 64-69] due to their prevalence and the high optical absorption of crystalline SiC at UV wavelengths single crystalline SiC is practically transparent at visible wavelengths, but has an optical absorption on the order of 10^{-5} cm^{-1} in the UV regime due to the higher-than-band gap photon energy. On the contrary, polycrystalline and amorphous, can absorb light in the visible and near IR spectra; this is a necessary condition for the success of lasers to ablate amorphous SiC [35, 46, 55, 56] and poly-SiC [31-33]. IR pulses have also been explored for single crystalline 4H-SiC where the ability to machine is a result of photons directly interacting with the lattice rather than through electrons [33, 58, 59, 70].

Lasers with ultrashort pulse widths ($\tau_p < 1$ picosecond) have been gaining interest in the laser micromachining community due to their ability to machine virtually any material including high bandgap dielectrics irrespective of the laser wavelength. Ultrashort laser processing of SiC has been shown to machine with high precision due to

their pulses being faster than heat dissipation [25]. The occurrence of nanostructures on the surface of SiC is a unique phenomena to femtosecond lasers which is stimulating researchers to pursue further studies.

Table 3 Laser Processing Applications for SiC

Application	Laser	λ (nm)	Material	Comment
Annealing	Excimer	193, 248, 308	Ion implanted damage zones (amorphous)	Ion implanted zones recover from amorphous to polycrystalline up to 500 nm deep [45-54,]
	Nd:YAG	355 nm	Amorphous film on dielectric	direct write of amorphous SiC converted to poly-SiC ~50nm, thick [55]
	Argon (CW)	514.5 nm	Amorphous film	Direct write of recrystallized zones of a-SiC to poly-SiC [35, 56]
Via Hole Drilling	CO ₂ 30ns Q-switched	10.6 μ m	4H-SiC	High ablation rate 0.47-1.8 μ m pulse ⁻¹ [56-58]
	Excimer	248	4H-SiC	Ablation rate ~0.23 μ m pulse ⁻¹ [60]
	Ti:Sapphire (femtosecond pulses)	800	4H-SiC	Ablation rate ~0.25 μ m pulse ⁻¹ [25]
<i>In situ</i> doping	Nd:YAG	1064	4H-SiC, 6H-SiC	n-type (nitrogen) doping 600 nm deep junction p-type (Al ⁺) doping 4.3 μ m deep junction [61]
	Excimer	193	4H-SiC, 6H-SiC	n-type (nitrogen) doping 50 nm deep junction p-type (Al ⁺) doping 150 nm deep junction
Electroless Metallization	Excimer	193, 308	Single Crystal (Hexagonal)	Catalytic sites of Si nanoclusters and thermal stress facilitates [62,63]
	Cu-Vapor	510		electroless Cu and Ni contacts [35, 36]
Nanostructuring	Ti:Sapphire (femtosecond pulses)	800	3C-SiC, 4H-SiC, 6H-SiC	Circular Polarization: Spherical Nanoparticles [40-43, 112] Linear Polarization: Nanoripples

It's well known that laser micromachining can be quite complicated by collateral thermal effects such as melt, recast, and heat affected zone (HAZ) and these effects are accentuated for nanosecond pulsed lasers. Thermal heating also plays an important role for annealing, doping, and non-congruent ablation processes. In general, semiconductor light absorption is dominated by photon-induced electron transitions from the valence to the conduction band by forming electron-hole pairs, and excess kinetic energy is transferred to the lattice as phonons within picoseconds resulting in heating [70]. Therefore, it is of interest to discuss the success of the heat dissipation studies from the literature [49, 69, 71, 72, 73] where researchers have focused primarily on the use of pulsed excimer lasers for annealing. As a rule of thumb the heat flow into the material is determined by the thermal penetration length, L_e , which is defined by equation 1. From this it is evident that the thermal penetration length of nanosecond lasers should be orders of magnitude higher than that of the femto, and even picosecond lasers.

$$L_e = 2\sqrt{D\tau_p} \quad (1)$$

where

D : Material Thermal Diffusivity

τ_p : Laser Pulse Width

Detailed modeling has been employed using a modified heat diffusion equation (2) and the Beer-Lambert equation (3).

$$\frac{\partial T}{\partial t} = \frac{\alpha}{\rho C_p} I(z, t) + \frac{1}{\rho C_p} \frac{\partial}{\partial z} \left(\kappa \frac{\partial T}{\partial z} \right) \quad (2)$$

$$I(z, t) = I_o(t)(1 - R)\exp(-\alpha z) \quad (3)$$

where

T : Absolute Temperature

t : Time

ρ : Density

C_p : Specific Heat

κ : Thermal Conductivity

I_o : Laser Intensity at the Surface

R : Surface Reflectivity

α : Optical Absorption

z : Depth below Surface

$I(z,t)$: Laser intensity at a depth z below the surface

Equations (2) and (3) are commonly used for pulsed excimer laser annealing [50, 64, 65, 73], but have also been used to model heating during dopant incorporation [61]. UV lasers where the optical absorption of amorphous SiC and crystalline SiC are on the same order of magnitude which are useful for annealing SiC surfaces disordered by ion implantation. Table 4 summarizes the optical absorption of crystalline and amorphous SiC for the excimer laser family.

Table 4 Optical absorption for excimer lasers

	ArF		KrF		XeCl		
	Crystalline	Amorphous	Crystalline	Amorphous	Crystalline	Amorphous	
Reflectivity (R%)	40	34.6	28.6	33.6	24.3	32.4	[72]
optical absorption (cm^{-1})	1.50×10^6	1.10×10^6	1.40×10^5	8.70×10^5	4.50×10^4	6.00×10^5	[72]

The laser irradiation model and heating has been used to optimize laser parameters that reach the melting temperature of 4H-SiC and 6H-SiC [73] substrates for annealing where the occurrence of melting is verified through *in situ* reflectivity measurements [49]. Reitano and Baeri were able to predict the thermal evaporation of a 6H-SiC target for pulsed laser deposition (PLD) over the fluence range 0.4 to 1.6 J cm^{-2} [64]. However, beyond 1.6 J cm^{-2}

the material was removed at a higher rate than predicted by the model suggesting molten material ejection from the surface [64, 65].

SiC undergoes non-congruent sublimation during thermal processing and laser heating results in an array of seemingly contradictory results such as oxidized [36, 37, 62, 63], carbon-rich (C-rich) or silicon-rich (Si-rich) surfaces [74]. Meanwhile, PLD of SiC films under high vacuum conditions exhibit excellent stoichiometry [75]. Some researchers [45, 33] report that SiC begins to sublime at temperatures between 1800°C and 2000°C yet does not melt until 2700°C. Still many others cite the occurrence of non-congruent sublimation at temperatures as low as 1000°C in bulk heating [76-80]. The non-congruent sublimation during bulk heating in vacuum proceeds with the breaking of Si-C bonds at approximately 1000°C and thermodynamically re-arrange on the surface where near surface Si quickly begins to sublime leaving behind a carbon-rich layer [76, 78-80]. The remains of the carbon-rich layer reduce the subsequent sublimation of Si with a diffusion-limited process [80]. The primary vapor constituents of thermally decomposed SiC are Si, SiC₂, and Si₂C where an overall decrease in the Si to C ratio occurs in the vapor at higher temperature [27]. While the thermal decomposition of SiC in bulk heating has been well studied, there is no analogous, singular study reporting on the decomposition due to laser irradiation [74]. It has been shown that non-congruent sublimation is also associated with laser ablation except that, in the case of the laser as a heating source, the optical properties of SiC play an important role in selecting the constituent removed from the surface [36, 81]. As a general rule excimer lasers produce Si-rich regions while IR Nd:YAG lasers seem to produce C-rich regions. Table 5 shows an overview of various laser processing conditions and their effects on the

surface characteristics. Pehrsson and Kaplan [45] found that multiple pulses from an ArF laser over the range of 0.4 – 0.6 J cm⁻² resulted in a rise in carbon on the surface, but beyond this range resulted in a Si-rich region. They hypothesized that excimer laser pulses tend to generate a graphite layer and its subsequent removal as the energy is trapped in this layer would reveal the underlying silicon [45].

Table 5 Surface enrichment and modification of SiC

SiC	Laser	λ (nm)	Pulse Width		Atmosphere	Laser Energy (J cm ⁻²)	Effect
3C-SiC	ArF	193	14	ns	8.00E-10 Torr	<0.40	No change
						0	
						0.400-0.600	A rise carbidic then graphite surface as the number of pulses increases
						>0.60	Si-rich surface
						0	
						2000	200nm thick Si region covering an underlying C-rich region
6H-SiC	Nd:YAG (with VUV-Raman Cell)	VUV-266	8	ns	1.00E-04 Torr	1.06	Ablation: Graphitic Surface on Base
Hexagonal	ArF, XeCl	193, 308	30	ns	Air	1-3.5	Si-rich covered with SiO ₂
Hexagonal	Cu-Vapor	514	15	ns	Air, Water, or 10-1 Torr	10-20	Si-rich surface
6H-SiC	Nd:YAG	1064	-	-	Argon (30 psi)	6.65	C-rich (back side of wafer)
95% relative density SiC	KrF	248	30	ns	Air	1.8	Disorderd region with oxidized surface

On the contrary, the Nd:YAG laser with its photon energy below the band gap results in a poor coupling with the material and mostly thermal effects causing evaporation of silicon [36, 81]. This has been explained as the reason why Nd:YAG lasers at 1064 and 532 nm result in C-rich surfaces [36, 81]. A notable exception to this hypothesis is the formation of

graphite surfaces when ablating 6H-SiC using a vacuum UV Raman cell with a frequency-quadrupled Nd:YAG laser (VUV-266 nm) [67]. As expected, oxide formation is associated with the processing of SiC in the presence of oxygen [82]. For example the excimer ablation of SiC on the range of 1-3.5 J cm⁻² in the presence of oxygen leads to the formation of a surface oxides and an underlying Si-rich layer [62] where only the enrichment of Si was reported under high vacuum conditions [46].

2. Additive Laser Processing

Additive laser processing for SiC microelectronics and MEMS research is being driven the challenges in traditional processing of SiC such as doping, annealing, and deposition on insulating substrates. Additive laser processing, as defined here, involves the addition of material or to meet a specific functionality of the surface through laser processing. This includes traditional techniques namely, laser annealing, pulsed laser deposition, and *in situ* laser doping, but also includes techniques unique to SiC such as metallization, electroless metal deposition, and nanoparticle formation.

2.1 Doping and Annealing of Silicon Carbide

Carriers are introduced into SiC using group III and V elements to form the respective p-type and n-type conducting materials. The most commonly investigated elements are boron and aluminum as acceptors and nitrogen and phosphorus as donors [24]. Conventional diffusion process for SiC remains impractical because temperatures greater than 2000°C are required [24]. Ion implantation results in a disordered surface requiring thermal annealing to partially recover the crystal at temperatures as high as 1100°C [126] and activation of impurities requires temperatures in excess of 1500°C [55]. These elevated temperatures are problematic

due to both the thermal damage incurred on the SiC and the fact that conventional furnaces used in the semiconductor industry are typically limited to 1300°C [24].

2.1.1 *In situ* laser doping of Silicon Carbide

In situ laser doping has been explored as an alternative to these conventional processes; principally nitrogen and aluminum have been the most investigated dopants. Laser doping exhibits high diffusion rates, orders of magnitude over conventional thermal diffusion methods [74] as summarized in Table 6. Functional devices and structures such as Schottky diodes, Ohmic contacts [81], p-n junctions, and LEDs [83, 84] have been demonstrated. Metallized contacts also exhibited an increase of 40% reflectivity suggesting it may be useful for optics and optoelectronic applications [71].

Table 6 Diffusion coefficients

Process	Material	Doping Constituent	Diffusion Coefficient (cm ² s ⁻¹)		Temperature	Laser		
			Fast Branch	Slow Branch		Type	Wavelength	
In Situ laser doping	6H-SiC	Nitrogen	2.4 x 10 ⁻⁵	9.26 x 10 ⁻⁶	-	Nd:YAG	1064 nm	[69]
	4H-SiC	Al	1.2 x 10 ⁻⁵	1.3 x 10 ⁻⁶	-	KrF	248 nm	
Thermal Diffusion	6H-SiC	Nitrogen	-	5 x 10 ⁻¹²	1800-2450°C	-	-	[24]
	6H-SiC	Al	-	3 x 10 ⁻¹⁴ – 6 x 10 ⁻¹²	1800-2300°C	-	-	

Three major categories of laser doping are: laser thermal processing (LTP), gas immersion laser doping (GILD), and laser-induced solid phase doping (LISPD). LTP involves a shallow ion implantation followed by laser heating to distribute and activate the carriers. GILD involves the use of a gaseous precursor which is thermally decomposed by the beam and incorporated into the molten surface as an impurity. LISPD is a category of laser doping

whereby the substrate is heated under the beam but does not achieve the melt. It can be carried out with either a dopant film or gaseous precursor similar to that used for GILD. Solid-state diffusion is aided by the deliberate formation of vacancies that facilitate the diffusion of impurities through the material, known as effusion-diffusion. Trimethylaluminum ($(\text{CH}_3)_3\text{Al}$) (TMA) was used for introduction of aluminum with LTP and GILD methods and N_2 gas for doping nitrogen. The principal lasers investigated for *in situ* laser doping are Nd:YAG lasers operating at 1064 nm and pulsed excimer lasers. Nd:YAG and excimer lasers act as bulk heating and surface heating tools respectively. As a result Nd:YAG lasers have been shown to generate much deeper dopant profiles for both aluminum and nitrogen [61].

2.1.2 Annealing of Silicon Carbide

Annealing of amorphous and poly-crystalline SiC is of interest for recovering surfaces damaged by ion implantation and specifically for MEMS applications where annealing amorphous SiC layers can achieve epitaxial and insulating layers [17]. In comparison to bulk thermal annealing, laser annealing has the advantage of being highly selective and rapidly heating to reduce the thermal effects of non-congruent sublimation. Epitaxial growth reactors have been used for doping, however, ion implantation has been shown to be successful [24].

There has been controversy regarding whether laser-induced recrystallization takes place through solid [48, 49, 50] or liquid phase recrystallization [46, 47, 49, 50, 51, 53, 55]. For example independent findings by Hishida *et al.* [48] and Ahmed *et al.* [51] revealed opposition effects with the same laser. Both groups used XeCl lasers to anneal Al^+ ion-implanted 6H-SiC, however, Hishida reported solid-phase recrystallization while Ahmed

reported liquid phase recrystallization. Both researchers used laser energy densities well above the melting threshold of XeCl lasers for both crystalline and amorphous SiC [73]. Hishida also reported a percentage of dopant activation over 4 orders of magnitude lower than that of Ahmed.

Solid-phase recrystallization has been reported for conventional thermal annealing of ion-implanted 6H-SiC at 940°C proceeding with epitaxial regrowth [85]. However there is no such phenomenon in laser annealing where solid phase recrystallization proceeds after either a single pulse just below the melt threshold or multiple pulses well below the melt threshold [48]. It is still uncertain that epitaxial solid-phase recrystallization is possible. Hishida *et al.* suggested that the recrystallization may be seeded by nucleation sites of un-damaged crystal structure if the surface is not completely amorphitized by the ion-implantation [48].

In contrast melt-phase annealing has been shown to be seeded by the underlying SiC crystal [47, 51], but the ability to fully recover the crystal through annealing has been disputed due to the poly-crystalline nature of the annealed surfaces [50]. The presence of melt phase during laser irradiation has been experimentally verified using *in situ* reflectivity measurements [49, 51] and is supported by the uniform impurity profile which cannot be explained by diffusion models [47, 51]. Melt phase can be achieved within a single shot, however the depth of the melt zone is affected by the heat diffusion characteristics of the material as discussed in Section 1.4. Polycrystalline layers exhibit higher resistance to melting and heat damage compared to the underlying amorphous layer, thus a multi-pulse approach where the energy is increased can lead to greater amount of recovery [55]. For

example a comparison between Ahmed *et al.* [51] who used a single pulse energy to achieve recrystallization layer (75 nm thick) versus Boutupoulos *et al.* who used the multi-pulse method to achieve a recovered layer 240-280 nm thick [55].

Crystallization of CVD amorphous SiC films has been achieved for insulating layers such as SiO₂ and high-temperature glass [35, 46, 56, 86]. Visible lasers have been used for this purpose due to the high optical absorption of amorphous SiC [35, 49, 86]. Also novel, combined UV-IR lasers have been used for this type of work [54].

2.2 Metallization of SiC Substrates

Perhaps one of the more intriguing phenomena in laser processing of SiC is the formation of metal-like surfaces through non-congruent ablation. Contacts are formed by laser heating via the formation of either C-rich or Si-rich depending upon the processing conditions [62, 74, 81] and have been shown to demonstrate ohmic properties [36, 74, 81]. Formation of C-rich contacts can be achieved through the use of frequency-doubled Nd:YAG lasers and Si-rich contacts through the use of pulsed excimer lasers [81]. The mostly thermal nature of the Nd:YAG lasers with its photon energy below the band gap leads to thermal evaporation of Si and excimer lasers result in the selective ablation of carbon [36, 81]. Salama et al. reported the formation of ohmic contacts with resistance over the range of 0.04-0.12 Ω -cm for both 4H-SiC and 6H-SiC substrates [81]. Regions ablate by pulsed excimer lasers have also been shown to facilitate the deposition of electroless Cu and Ni metals [36, 37, 62, 63]. Laser ablation causes the formation of two different catalytic centers that facilitate the deposition of metals from electroless solutions: Si nano-clusters and bending of conduction band from

mechanical stresses [36]. These catalytic sites remain stable over a long period of time and the metallization layers can be stripped and deposited repeatedly [63].

2.3 Pulsed Laser Deposition of Silicon Carbide Thin Films

An array of conventional growth techniques for single crystalline SiC are available such as Chemical Vapor Deposition (CVD), Carbonization [87], Molecular Beam Epitaxy (MBE) [88] and photo, plasma or laser CVD [89] but these methods suffer from poor film quality due to contamination with hydrogen compounds caused by high substrate temperature in the process. Pulsed Laser Deposition (PLD) is an alternative technique with advantages such as low substrate temperature, high deposition rate, and relative ease of producing stoichiometric films [75]. Processing conditions for PLD films are summarized in Table 7.

Table 7 Pulsed laser deposition parameters

Deposited Film	Laser	λ (nm)	τ (ns)	Repitition Rate (Hz)	Pulse Energy (mJ)	Energy Density (J cm^{-2})	Substrate Temperature	Annealing Temperature	
4H-SiC	XeCl	308	23	-	-	-	850°C	1100°C - 1400°C	[7]
3C-SiC	ArF	193	17	3	150-200	-	800°C	980°C	[20]
6H-SiC		266		-	-	-	1100°C - 1200°C	-	[98]
3C-SiC	KrF	248	25	5, 10	-	2.5	700°C	-	[92]
-	KrF	248	25	100	-	5	250°C	-	[123]
-	KrF	248		5-10	500	-	500°C	-	[124]
3C-SiC	XeCl	308	20	1	520	-	800°C	-	[125]
3C-SiC	KrF	248	20	10	-	5	370°C	800-1200°C	[94]
3C-SiC	KrF	248	20	10	-	3.2	400-950°C	1100°C	[126]

3C-SiC films have been deposited on Si at lower substrate temperature [90-95]. Interestingly, Soto et al. found for SiC films deposited under argon environment exhibited better stoichiometry than those grown under nitrogen or even vacuum conditions [96]. The PLD films are greatly affected by the surface preparation and the processing

conditions [97, 98]. High-quality epitaxial films were dependent on type of substrate used (α -SiC or β -SiC), substrate temperature, laser parameters such as photon energy, frequency, wavelength and pulse width. Films exhibiting crystallinity were observed when substrate temperature was between 700°C [90] and 800°C [94, 99]. All films deposited between 400 and 800°C are extremely smooth with roughness on the order of 0.40 ± 0.2 nm. Roughness increases substantially with temperature. Roughness of 4.70 ± 0.8 nm for the film deposited at 950°C was attributed to the formation of large crystallites [93]. Annealing following deposition has also been reported to facilitate the conversion from polycrystalline to single crystalline films [94, 95, 99]. Conversion of amorphous to 3C-SiC films occurs at 980°C [95] while conversion to 4H-SiC occurs in the range of 1100°C to 1400°C [99].

2.4 Nanoparticle formation

Nanostructured surfaces are useful for applications in quantum electronics, opto-electronics, tribiology, and NEMS. Laser-induced nanostructures on 6H-SiC were demonstrated to have decreased reflectivity and increased optical absorption by as much as 39% [100]. *In situ* formation of nanoripples under laser irradiation was first reported on the surface of germanium using a ruby laser [101]. More recently femtosecond lasers have been reported to form spherical nanoparticles and periodic nanoripples on a variety of dielectrics and semiconductor materials with feature size from $\lambda/3$ - $\lambda/10$ where λ is the wavelength [102-110].

Nanostructure formation occurs at low energy fluences well below that required for inducing melt and ablation. Spherical nanoparticles form under circularly polarized beams while nanoripples are associated with linearly polarized beams. The nanoripples are oriented

perpendicular to the electric field of the laser beam [102, 105, 108, 109]. Similar results were also reported for crystalline SiC [40, 41, 100, 111, 112, 113]. There is still controversy over the exact mechanism that causes the formation of nanoripples but it has been attributed to phenomena such as Coulomb explosion [40, 41], self assembly [106, 107], and laser beam interference with the plasma [103].

The majority of the work carried out in femtosecond laser-induced formation of nanoparticle has been the irradiation of small regions of the surface with multiple pulses. The high peak power of the femtosecond laser and Gaussian profile of beam lead to a large energy fluence distribution across the beam. Nanoparticles have been found to form within discrete regions associated with the varying energy density resulting in concentrically aligned regions of nanoparticles [40, 112, 113]. Dong and Molian determined threshold regimes for three distinct nano-structured zones under a circularly polarized beam. The structure regions are: a transition zone, a ripple zone with ripples parallel to the electric field, and a center zone caused by heat, melt, and recast [39, 41]. Similarly, Tomita *et al.* also observed regions associated with the energy density of the beam on 4H-SiC using a linearly polarized beam with more pronounced nanoripples [112]. The formed nanoripples were oriented parallel to the electric field of the beam only at the center, and the peripheral zones formed perpendicular to it [112]. In the interest of developing surfaces useful for device applications, long range coverage of surfaces with nanostructures have also been explored with linearly polarized beams [114] and circularly polarized beams [43] to create a long range array of nanostructures in the beam tracks. Juodkazis *et al.* established a region greater than 10 x 10 mm region of nanoripples by raster scanning a beam [114]. Spherical nanoparticle

formation in the beam tracks were reported with a track width of several microns over a length of tens of microns [43].

3. Subtractive Laser Processing

Material removal of SiC through laser ablation has been investigated extensively on all polytypes – single, polycrystalline, and amorphous - SiC. Conventional MEMS and microfabrication techniques involve the use of masking, wet etching of specific crystal orientations or dry etching using reactive ion etching. However, the chemical inertness and hardness of SiC slow down wet etching and dry etching methods although DRIE has enjoyed the most success as subtractive micromachining process for SiC with etch rates of $2 \mu\text{m min}^{-1}$ [115]. The interest in etching SiC has also inspired the exploration of more novel processing methods such as PhotoElectroChemical (PEC) etching which has achieved etch rates of $25 \mu\text{m min}^{-1}$ [116]. In contrast laser ablation of SiC is capable of high etch rates on the order of hundreds of microns per second [57-59], reduces the number of processing steps by avoiding the need for masking, machining is independent of crystal structure, and curved surfaces are possible. However, laser micromachining of structures on SiC has principally been limited to via hole formation [25, 44, 57, 58, 59, 60]. Only a few MEMS structures have been laser micromachined. Laser ablation for micromachining of SiC is certainly a promising area of microfabrication. Not only can lasers achieve etch rates on the order of hundreds of $\mu\text{m min}^{-1}$, but material removal of SiC through laser ablation has been demonstrated to be consistent over tens to hundreds of pulses [58, 60, 116] for UV, IR, and femtosecond lasers with few special exceptions [116]. Ablation rates are summarized in Table 8.

Table 8 Laser ablation rates

Material	Wavelength (nm)	Pulse Width		Fluence (J cm ⁻²)	Ablation Rate (nm/pulse)	Repetition Rate (Hz)	Temporal Ablation Rate (μm/min)	Atmosphere		
3C- SiC	248	14	ns	2	40	100	240*	8.00E-10	Γ _{orr}	[45]
	248	34	ns	8	100	100	600*	Air		[25]
	193	25	ns	8	100*	100	600*			
	1026	400	fs	1.2	60*	-	-			
	1040	300	fs	10.60	-	-	600-900			
-	<20 0	fs	105- 180	-	50,000	33000- 15600	-			[44]
4H- SiC	1060	30	ns	-	470-1800*	8	229-870	N ₂ Flow		[57- 59]
	248	30	ns	-	230	100	1380*	Air		[117]
	800	120	fs	20	250	-	-	Air		[43]
	355, 532, 1064	-		-	-	60 x 10 ³	3000	Air		[120]
355, 532, 1064	30	ns	-	-	8	120-840	-			[121]
6H- SiC	266	8	ns	1.06	35	1	2.10	1.00E-04	Γ _{orr}	[66- 68]
	308	15	ns	2.20	60	100	360*	1.00E-06	Γ _{orr}	[64, 65]
a-SiC	193	5	ns	-	200*	100	1200*	Air		[119]

* Interpolation of reported data

Laser ablation of the crystalline SiC polytypes is principally investigated using UV-lasers [34, 25, 66, 60] due to the high optical absorption. Similar behavior was noted in amorphous SiC [73]. Using an excimer laser, Desbiens and Masson were able to machine deep structures up to 200 μm in amorphous SiC wafers [119]. They determined that machining conditions were optimized for low energy and high repetition rates with high scan speeds [119]. Thin diaphragm structures as seen in Figure 1 were machined using fluence of 5 J cm⁻², repetition rate of 100 Hz, and scan speed of 170 μm s⁻¹ [119].

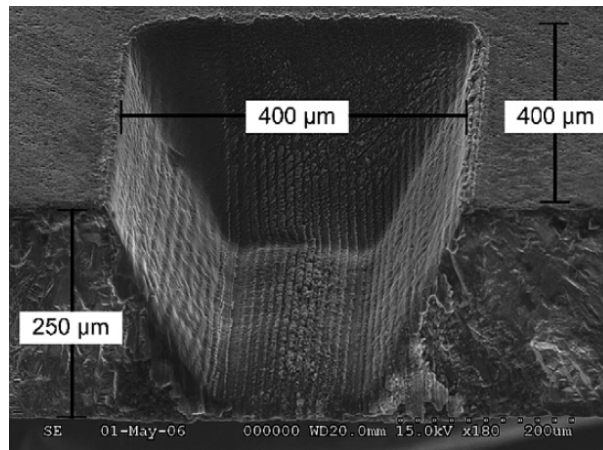


Figure 1 ArF laser micromachined trench on amorphous SiC [119]

Excimer lasers are advantageous because of their large beam size and uniform energy distribution and ability to be used with masking operations, however there has yet to be a SiC structure formed using masking techniques. Despite the poor optical absorption of single crystalline SiC, visible [36] and IR [33] photons are capable of coupling directly with the lattice and generating absorbing species resulting in high etch rates. Kim, Pearton, and co-workers reported high etch rates $229\text{-}870\ \mu\text{m min}^{-1}$ on single crystalline 4H-SiC using a $10.6\ \mu\text{m}$ laser with repetition rate of 10 Hz for drilling via holes [57-59]. Similarly, high etch rates were reported for a Nd:YVO₄ laser at wavelengths 355, 532, 1064 nm and 30 ns pulse widths, however the lower wavelengths produced better sidewalls, and the lowest amounts of debris [120, 121]. In contrast to single crystals, amorphous and polycrystalline SiC enjoys more machining versatility with these lasers due to the high optical absorption in this regime. This has allowed for highly selective control of the depth and thereby enable the machining of complex 3D structures aided by the use of high repetition rates [37, 82]. Kruezt *et al.* used Q-switched Nd:YAG ($\lambda = 1064\ \text{nm}$ $\tau_p = 10\ \text{ns}$) to machine complex 3D structures in poly-SiC stock material such as 3D semi-spherical depression and thread structures [82]. Surface

quality was optimized when using a fluence less than 15 J cm^{-2} and scan speeds less than 10 mm s^{-1} [82].

Femtosecond pulses have been shown to have excellent machining properties because of their ultrafast interaction times resulting in low thermal diffusion, and their multi-photon absorption which negates the requirement for matching a specific laser wavelength to a material. Femtosecond lasers have been have produced low HAZ and fast etch rates in via hole formation [25, 43, 44], 3C-SiC thin film scribing [43] and 4H-SiC bulk material removal [122]. Dong and Molian reported high quality femtosecond laser micromachining of single crystalline 3C-SiC [43, 122]. Pulse energy ranging from (1-10 μJ) was found to be optimal for producing high resolution, damage free features. In this range, high quality 3C-SiC micro-rotors were patterned [43]. Figure 2 shows SEM micrographs of the micro-rotor before and after KOH release. It was found that as the energy increases ($>20 \mu\text{J}$) more damage was done to the structure. Lower pulse energy produces a well defined profile with little contamination and minimal thermal damages as shown in Figure 2. Similarly diaphragm structures as deep as $100 \mu\text{m}$ were formed on 4H-SiC by trepanning the beam with respect to the substrate [122]. Femtosecond lasers are not immune to thermal effects. For pulse energies greater than $50 \mu\text{J}$ significant amount of recast layer and damaged fragments [43] were observed are attributed to the formation of plasma. However, high repetition (50 MHz) rates have been shown by Farsari et al. to have little impact on the thermal saturation of 3C-SiC.

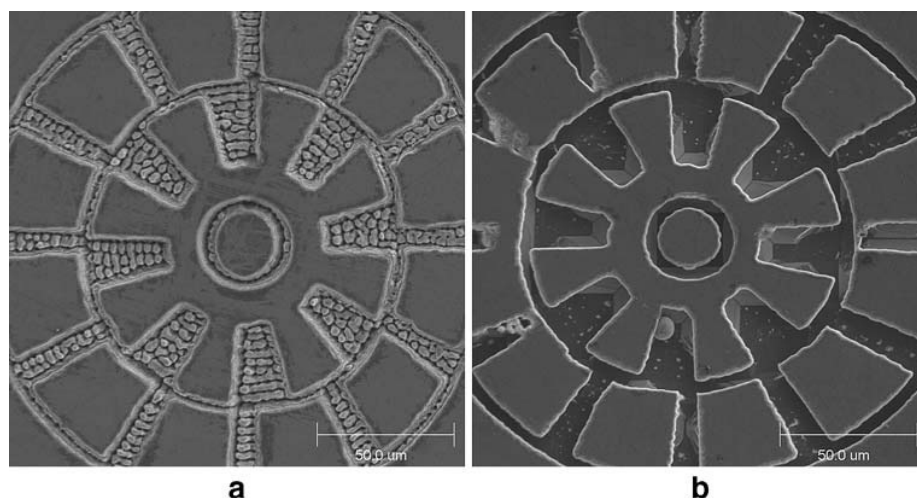


Figure 2 Femtosecond laser micromachined rotor in 3C-SiC thin films deposited on silicon before and after partial release from substrate [43].

4. Conclusion

Due to its outstanding properties, SiC is highly desirable for microelectronics and MEMS applications in harsh and hostile environments. However, the development of these devices are limited by the inability to use conventional microfabrication techniques. Laser microprocessing of silicon carbide has been explored for both additive and subtractive processes. Effective laser processing has been demonstrated in numerous areas of SiC microfabrication as a flexible means of processing. With fewer steps and is capable of parallel processing. Nanosecond lasers in the UV regime have been investigated more widely in the literature with some indication that the IR-spectrum could be used for appropriate applications such as via hole drilling and contact formation. Femtosecond lasers have yet to enjoy the same widespread commercial success as of the nanosecond lasers, but have been successfully shown to produce precision SiC structures with minimal HAZ and formation of stoichiometric nanoparticles and nano-ripples on the surfaces of crystalline SiC.

Acknowledgement

This material is based in part upon work supported by the National Science Foundation under Grant Number CMMI-0619115. Any opinions, findings, and conclusions or recommendations expressed in this material are those of the authors and do not necessarily reflect the views of the National Science Foundation.

References

- [1] M. Mehregany and C.A. Zorman: *Thin Solid Films* , 355-356 (1999) 518.
- [2] C.A. Zorman and M. Mehregany: *IEEE, Sensors Proceedings, Cleveland, OH, USA. ,* (2002) 1109.
- [3] P.M. Sarro: *Sensors and Actuators A*, 82 (2000) 210.
- [4] "Silicon Carbide Micromechanical Systems for Harsh Environments" ed. by Rebecca Cheung, (Imperial College Press, London, 2006) p.128.
- [5] J.V. Berg, R. Ziermann, W. Reichert, E. Obermeier, M. Eickhoff, G. Krotz, U. Thoma, Th. Boltshauser, C. Cavalloni, and J.P. Nendza: *Materials Science Forum*, 264-268 (1998) 1101.
- [6] L.S. Pakula, H. Yang, H.T.M. Pham, P.J. French, and P.M. Sarro: *Journal of Micromechanical Microengineering*, 14 (2004) 1478.
- [7] D.J. Young: *IEEE Journal*, 4 (2004) 464.
- [8] H-I. Kuo, C.A. Zorman, M. Mehregany: *12th International Conference on, TRANSDUCERS, Solid-State Sensors, Actuators and Microsystems, Cleveland, OH, USA.* (2003) p.742.

- [9] R.S. Okojie, A.A. Ned, A.D. Kurtz, and W.N. Carr: International Electron Devices Meeting, San Fransico, CA, USA., (1996) 20.2-1.
- [10] R.S. Okojie, P. Nguyen, V. Nguyen, E. Savrun, D. Lukco, J. Buehler, and T. McCue: 45th annual IEEE international Reliability physics symposium proceedings, NASA Glenn Res. Center, Cleveland, OH. (2007) p.429.
- [11] A.A. Ned, A.D. Kurtz, G. Beheim, F. Masheeb, and S. Stefanescu: J. Appl. Phys., 82 (1997) 4310.
- [12] R.S. Okojie: Sensors and Actuators A, 66 (1998) 200.
- [13] A.R. Atwell, R.S. Okojie, K.T. Kornegay, S.L. Roberson, and A. Beliveau: Sensors and Acutators A, 104 (2003) 11.
- [14] K.A. Lohner, K-S. Chen, A.A. Ayon, and S.M. Spearing: Materials Research Symposium Proceedings (1999) p.85.
- [15] A.A Yassen: IEEE Electron Device Letters, 21 (2000) 164.
- [16] J. Hornberger, A.B. Lostetter, K.J. Olejniczak, T. McNutt, S. Magan, and A. Mantooth: 2004 IEEE Aerospace Conference Proceedings (2004) p. 2538.
- [17] J.M. Melzak: IEEE MTT-S International Microwave Symposium Digest, FLX Micro, Solon, OH, USA. (2003) p.1629.
- [18] X-B. Li , E-W. Shi , Z-Z. Chen, and B. Xiao: Diamond & Related Materials, 16 (2007) 654.
- [19] S. Nakashima and K. Kisoda: J. Appl. Phys., 75 (1994).
- [20] C.H. Wu, C.A. Zorman, and M.Mehregany: Thin Solid Films, 355-356 (1999) 179.

- [21] J. von Berg, R. Ziermann, W. Reichert, E. Obermeier, M. Eickhoff, G. Krötz, U. Thoma, Th. Boltshauser, C. Cavalloni, and J.P. Nendza: Materials Science Forum, 264-268 (1998) 1101.
- [22] R. Yakimova, G. Reza Yazdi, N. Sritirawisarn and M. Syvajarvi: Materials Science Forum, 527-529 (2006) 283.
- [23] F. Bechstedt, P. Käckell, A. Zywietz, K. Karch, B. Adolph, K. Tenelsen, and J. Furthmüller: Phys. Stat. Sol. (b), 202 (1997) 35.
- [24] "Process Technology for Silicon Carbide" ed. by Carl-Mikael Zetterling, (INSPEC, London, 2002).
- [26] "Properties of Advanced Semiconductor Materials" ed. by M.E. Levinshtein, S.L. Rumyantsev, M.S. Shur, (John Wiley and Sons, New York, 2001) p.93.
- [27] "Properties of Silicon Carbide" ed. by Gary L. Harris, (INSPEC, London, 1995).
- [28] "Semiconductor Sensors" ed. by S.M. Sze, (John Wiley and Sons, New York, 1994).
- [29] J. D. Reddy, A.A. Volinsky, C.L. Frewin, C. Locke, S.E. Sadow: Material Research Society.
- [30] "Properties of Crystalline Silicon" ed. by Robert Hull, (INSPEC, London, 1999).
- [31] I. Shigematsu, K. Kanayama, A. Tsuge, and M. Nakamura: Journal of Material Science Letters, 17 (1998) 737.
- [32] D. Sciti and A. Bellosi: Key Engineering Materials, 206-213 (2002) 305.
- [33] R.F. Wood and D.H. Lowndes: Crystal Lattice Defects and Amorphous Materials, 12 (1985) 475.
- [34] A. Medvid and P. Lytvyn: Materials Science Forum, 457-460 (2004) 411.

- [35] C. Palma, M.C. Rossi, and C. Sapia : Electronics Letters, 34 (1998) 1430.
- [36] A.A. Lyalin, E.D. Obraztova, A.V. Simakin, I.I. Vlasov, and G.A. Shafeev: Fourth International High Temperature Electronics Conference HITEC, Albuquerque, NM, (1998) p.308.
- [37] S.I. Dolgaev, V.V. Voronov, G.A. Schafeev, C. Fauquet-Ben Ammar, J.M. Themlin, and A. Cros, W. Marine: Applied Surface Science, 109-110 (1997) 559.
- [38] J. Jandeleit, A. Horn, R. Weichenhain, E.W. Kreutz, and R. Poprawe : Applied Surface Science, 127-129 (1998) 885.
- [39] Y. Dong and P. Molian: Applied Physics A, 77 (2003) 839.
- [40] Y. Dong and P. Molian: Applied Physics Letters, 84 (2004) 10.
- [41] Y. Dong and P. Molian: Physica Status Solid A, 202 (2005) 1066.
- [42] Y. Dong, C. Zorman, and P. Molian: Journal of Micromechanical Microengineering, 13 (2003) 680.
- [43] B. Pecholt, M. Vendan, Y. Dong, and P. Molian: The International Journal of Advanced Manufacturing Technology.
- [44] M. Farsari, G. Filippidis, S. Zoppel, G.A. Reider, and C. Fotakis: Journal of Micromechanical Microengineering, 15 (2005) 1786.
- [46] S. Urban and F. Falk: Applied Surface Science, 184 (2001) 256.
- [47] S.Y. Chou, Y. Chang, K.H. Weiner, and T.W. Sigmon, and J.D. Parsons: Applied Physics Letters, 56 (1990) 530.
- [48] Y. Hishida, M. Watanabe, K. Nakashima, and O. Eryu: Materials Science Forum, 338-342 (2000) 873.

- [49] P. Baeri, C. Spinella, and R. Reitano: *International Journal of Thermophysics*, 20 (1999) 1211.
- [50] A. Hedler, S. Urban, F. Falk, H. Hobert, and W. Wesch: *Applied Surface Science*, 205 (2003) 240.
- [51] S. Ahmed, C.J. Barbero, and T.W. Sigmon: *Applied Physics Letters*, 66 (1995) 712.
- [52] D. Sands, P.H. Key, M. Schlaf, C.D. Walton, C.J. Anthony, and M.J. Uren: *Materials Science Forum*, 338-342 (2000) 655.
- [53] P.H. Key, D. Sands, M. Schalf, C.D. Walton, C.J. Anthony, K.M. Brunson, and M.J. Uren: *Thin Solid Films*, 364 (2000) 200.
- [54] N.I. Cho, Y.M. Kim, J.S. Lim, C. Hong, Y. Sul, and C.K. Kim: *Thin Solid Films*, 409 (2002).
- [55] C. Boutopoulos, P. Terzis, I. Zergoiti, A.G. Kontos, K. Zekentes, K. Giannakopoulos, and Y.S. Raptis: *Applied Surface Science*, 253 (2007) 7912.
- [56] C. Palma and C. Sapia: *Journal of Electronic Materials*, 29 (2000) 607.
- [57] S.J. Pearton, C.R. Abernathy, B.P. Gila, F. Ren, J.M. Zavada, and Y.M. Park: *Solid-State Electronics*, 48 (2004) 1965.
- [58] S. Kim, B.S. Bang, F. Ren, J. D'Etremont, W. Blumenfeld, T. Cordock, and S.J. Pearson: *Journal of Electronic Materials*, 33 (2004) 477.
- [59] S. Kim, B.S. Bang, F. Ren, J. D'Etremont, W. Blumenfeld, T. Cordock, and S.J. Pearson: *Journal of Semiconductor Technology*, 4 (2004) 217.
- [60] E.W. Krutz, R. Weichenhain, R. Wagner, and A. Horn: *RIKEN Review, Journal* (2003) 83.

- [61] Z. Tian, I.A. Salama, N.R. Quick, and A. Kar: *Acta Materialia*, 53 (2005) 2835.
- [62] G.A. Shafeev, L. Bellard, J.M. Themlin, C. Fauquet-Ben Ammar, and A. Cros, W. Marine : *Applied Physics Letters*, 68 (1996) 773.
- [63] G.A. Schafeev, L. Bellard, J-M, Themlin, C. Fauquet-Ben Ammar, and A. Cros, W. Marine: *Surface Coatings Technology*, 80 (1996) 224.
- [64] R. Reitano, P. Baeri, and N. Marino: *Applied Surface Science*, 96-98 (1996) 302.
- [65] R. Reitano, P. Baeri, and N. Marino: *Nuclear Instruments and Methods in Physics Research B*, 116 (1996) 369.
- [66] J. Zhang, K. Sugioka, S. Wada, H. Tashiro, and K. Midorikawa: *Applied Surface Science*, 127-129 (1998) 793.
- [67] J. Zhang, K. Sugioka, S. Wada, H. Tashiro, K. Toyoda, and K. Midorikawa: *Applied Physics A*, 64 (1997) 367.
- [68] K. Suioka and K. Midorikawa: *First International Symposium on Laser Precision Microfabrication* (2000) p.110.
- [69] Z. Tian, N.R. Quick, and A. Kar: *Acta Materialia*, 54 (2006) 4273.
- [70] "Laser Ablation: Principal and Application" ed. by editor: J.C. Miller, (Springer-Verlag, New York, 1994).
- [71] Z. Tian 2006 Ph.D. Thesis University of Central Florida.
- [72] B. Garcia, M. Estrada, F. Cruz-Gandarilla, M.N.P. Carreno, and I. Pereyra: *Proceedings of the Fifth IEEE International Caracas Conference on Devices, Circuits and Systems*, Dominican Republic, Nov. 3-5 (2004).
- [73] C. Dutto, E. Fogarassy, and D. Mathiot: *Applied Surface Science* , 184 (2001) 362.

- [74] I.A. Salama, N.R. Quick, and A. Kar: International Symposium on Compound Semiconductors, Orlando, FL, USA, (2004) p.1.
- [75] D. Dijkkamp and T. Venkatesan: Applied Physics Letters, 51 (1987) 619.
- [76] L. Muehlhoff, W.J. Choyke, M.J. Bozack, and J.T. Yakes Jr.: Journal of Applied Physics, 60 (1986) 2842.
- [77] Y. Song and F.W. Smith: Applied Physics Letters, 81 (2002) 3061.
- [78] W.H. Soe, K.H. Rieder, A.M Shikin, V. Mozhaiskii, A. Varykhalov, and O. Rader: Physical Review B, 70 (2004) 115421-1.
- [79] S. Adachi, M. Mohri, and T. Yamashina: Surface Science, 161 (1985) 479.
- [80] J.J. Bellina Jr. and M.V. Zeller: Applied Surface Science, 25 (1986) 380.
- [81] I.A. Salama, N.R. Quick, and A. Kar: Materials Research Society Symposium Proceedings (2003) p.75.
- [82] E.W. Kreutz, R. Weichenhain, and A. Horn: MEMS design, fabrication, characterization, and packaging; 30 May-1 June 2001 (2001) p.109.
- [83] S. Bet, N. Quick, and A. Kar: Phys. Stat. Sol. A, 204 (2007) 1147.
- [84] Z. Tian, N.R. Quick, and A. Kar: Journal of Electronic Materials, 34 (2006) 430.
- [85] I-T. Bae, M. Ishimaru, and Y. Hirotsu: Japanese Journal of Applied Physics, 44 (2005) 6196.
- [86] H. Hobert, H.H. Dunken, S. Urban, F. Falk, and H. Stafast: Vibration Spectroscopy, 29 (2002) 117.
- [87] H. Nagasawa and K. Yagi: Phys. Stat. Sol. (b), 202 (1997) 335.

- [88] Tomoaki Hatayama, Yoichiro Tarui, Takashi Fuyuki, and Hiroyuki Matsunami: *Journal of Crystal Growth*, 150 (1995) 934.
- [89] S.J. Toal, H.S. Reehal, N.P. Barradas, and C. Jaynes: *Applied Surface Science*, 138-139 (1999) 424.
- [90] M. Malooch, R.J. Tench, W.J. Seikhaus, M.J. Allen, and A.L. Connor: *Applied Physics Letters*, 57 (1990) 1540.
- [91] C. Gica, C. Ristoscu, G. Socol, D. Brodoceanu, L.C. Nistor, I.N. Mihailescu, A. Klini, and C. Fotakis: *Applied Surface Science*, 252 (2006) 4672.
- [92] Valentin Craciun, Eric Lambers, Nabil D. Bassim, Ronald H. Baney, and Rajiv K. Singh: *Journal of Vacuum Science Technology A*, 19 (2000) 2691.
- [93] M. Tabbal, A. Said, E. Hannoun, and T. Christidis: *Applied Surface Science*, 253 (2007) 7050.
- [94] Y.S. Katharria, Sandeep Kumar, Ram Prakash, R.J. Choudhary, F. Singh, D.M. Phase, and D. Kanjilal: *Journal of Non-Crystalline Solids*, 353 (2007) 4660.
- [95] J. Huang, L. Wang, J. Wen, Y. Wang, and C. Lin, M. Ostling: *Diamond and Related Materials*, 8 (1999) 2099.
- [96] G. Soto, E.C. Samano, R. Machorro, and L. Cota: *Journal of Vacuum Science Technology A*, 16 (1998) 1311.
- [97] Alok Chauhan, Wilton Moran, Shouren Ge, Weidong Si, and Henry J. White: *Scripta Materialia*, 52 (2005) 735.
- [98] Hachizo Muto, Shin-ichiro Kamiya, and Takeshi Kusumoi: *Optical Materials*, 23 (2003) 43.

- [99] Yuxia Wang, Jun Wen, Zhen Guo, Yeqing Tang, Honggao Tang, and Jianxin Wu: *Thin Solid Films*, 338 (1999) 93.
- [100] Q.Z. Zhou, F. Ciobanu, S. Malzer, and L.J. Wang: *Applied Physics Letters*, 91 (2007) 12110.
- [101] M. Birnbaum: *Journal of Applied Physics*, 36 (1965) 3688.
- [102] N. Yasumaru, K. Miyazaki, and J. Kiuchi, : *Applied Physics A*, 76 (2003) 983.
- [103] Y. Shimotsuma, P. Kazansky, J. Qiu, and K. Hirao: *Physical Review Letters*, 91 (2003) 247405.
- [104] A. Ozkan, A. Malshe, T. Railkar, W. Brown, M. Shirk, and P. Molian: *Applied Physics Letters*, 75 (1999) 3716.
- [105] Q. Wu, Y. Ma, R. Fang, Y. Liao, Q. Yu, X. Chen, and K. Wang: *Applied Physics Letters*, 82 (2003) 1703.
- [106] J. Reif, F. Costache, M. Henyk, and S. Pandelov: *Applied Surface Science*, 197 (2002) 891.
- [107] F. Costache, M. Henyk, and J. Reif: *Applied Surface Science*, 186 (2002) 352.
- [108] C. Hnatovskya, R. S. Taylor, P. P. Rajeev, E. Simova, V. R. Bhardwaj, D. M. Rayner, and P. B. Corkum: *Applied Physics Letters*, 87 (2005) 14104.
- [109] T. Jia, H. Chen, M. Huang, F. Zhao, J. Qiu, R. Li, Z. Xu, X. He, J. Zhang, and H. Kuroda: *Physics Review B*, 72 (2005) 125429.
- [110] A. Borowiec and H. Haugen: *Applied Physics Letters*, 82 (2003) 4462.
- [111] T.Q. Jia, F.L. Zhao, M. Huang, H.X. Chen, J.R. Qiu, R.X. Li, Z.Z. Xu, and H. Kuroda: *Applied Physics Letters*, 88 (2006) 111117-1.

- [112] T. Tomita, K. Kinoshita, and S. Matsuo: CLEO/Pacific Rim 2005. Pacific Rim Conference on Lasers and Electro-Optics (2005) p.1744.
- [113] T. Tomita, K. Kinoshita, S. Matsuo, and S. Hashimoto: Applied Physics Letters, 90 (2007) 153115-1.
- [114] S. Juodkazis, K. Nishimura, H. Okuno, Y. Tabuchi, S. Matsuo, S. Tanaka, and H. Misawa: Proceedings of SPIE - The International Society for Optical Engineering (2007) p.67320B-1.
- [115] "The MEMS Handbook" ed. by Mohamed Gad-el-Hak, (CRC Press, New York, 2002).
- [116] J.S. Shor, A.D. Kurtz, I. Grimberg, B.Z. Weiss, and R.M. Osgood: Journal of Applied Physics, 81 (1997) 1546.
- [117] K. Zekentes, I. Zergoiti, A. Klini, and G. Constantindis : Materials Science Forum, 527-529 (2006) 1119.
- [118] N. Aoki, K. Sugioka, K. Obata, T. Akane, T. Takahashi, S.H. Cho, H. Kumagai, K. Toyoda, and K. Midorikawa: The 4th Pacific Rim Conference on Lasers and Electro-Optics, 2001.
- [119] J.P. Desbiens and P. Masson: Sensors and Actuators A, 136 (2007) 554.
- [120] T. Anderson, F. Ren, S.J. Pearton, M.A. Mastro, R.T. Holm, R.L. Henry, C.R. Eddy, Jr., J.Y. Lee, K-Y. Lee, and J. Kim: Journal of Vacuum Science Technology B, 24 (2006) 2246.
- [121] T.J. Anderson, F. Ren, L. Covert, J. Lin, S.J. Pearton, T.W. Dalrymple, C. Bozada, R.C. Fitch, N. Moser, R.G. Bedford, and M. Schimpf: Journal of Electronic Materials, 35 (2006) 675.

- [122] Y. Dong 2003 Ph.D. Thesis, Mechanical Engineering, Iowa State University.
- [123] Y.H. Tang, T.-K. Sham, D. Yang, and L. Xue: *Applied Surface Science*, 252 (2006) 3386.
- [124] A. Chauhan, W. Moran, S. Ge, W. Si, and H.J. White: *Scripta Materialia*, 52 (2005) 735.
- [125] Balooch M., Tench R. J., Siekhaus W. J., Allen M. J. and Connor A. L., *Appl. Phys. Lett.*, 57 (1990) 1540.
- [126] M. Tabbal, A. Said, E. Hannoun, and T. Christidis: *Applied Surface Science*, 253 (2007) 7050.
- [127] C. Ghica, C. Ristoscu, G. Socol, D. Brodoceanu, L.C. Nistor, I.N. Mihailescu, A. Klini, C. Fotakis, *Appl. Surf. Sci.* 252 (2006) 4672.

CHAPTER 3 EXCIMER LASER ABLATION AND MICROMACHINING OF SINGLE CRYSTAL 4H-SiC AND 6H-SiC

A paper submitted to *Applied Physics A*

Saurabh Gupta, Ben Pecholt and Pal Molian

Abstract

A 248 nm, 23 ns pulsed excimer laser was used to compare the ablation characteristics of single crystal wafers of 4H-SiC and 6H-SiC over a wide range of energy fluence (0.8 – 25 Jcm⁻²). Photothermal models based on Beer-Lambert equation using thermal diffusivity and absorption coefficient; energy balance; and heat transfer were presented to predict the ablation mechanisms. Micromachining of trenches was demonstrated at 7 J/cm² to illustrate the potential of UV laser ablation. Results indicate that the ablation process is characterized by two well-defined threshold fluences: (a) decomposition threshold ~ 1 Jcm⁻² and (b) melting threshold ~ 1.5 Jcm⁻² for both polytypes. Contrary to expectations, the ablation rate increased marginally with energy fluence. Four types of ablation mechanisms – chemical decomposition, vaporization, explosive boiling and plasma shielding – either singly or in combination are believed to occur as a function of energy fluence. The predictions of photothermal models were not in agreement with the experimental data implying that a complex interplay among various physical phenomena occurs during ablation. Micromachined trench exhibited ripple patterns, microcracks and recast layers, most of which could be eliminated by a subsequent chemical cleaning process.

1. Introduction

Silicon carbide (SiC) is being used as a semiconductor or insulator in high-temperature and harsh chemical environments due to its exceptional properties such as wide bandgap, chemical inertness, thermal stability and mechanical strength. SiC finds a number of applications in the fields of power electronics, microelectronics and micro-electro-mechanical-systems (MEMS). Physical and chemical sensors, micromotors and resonators are some examples of SiC-based MEMS devices that are designed to operate in heat, chemical and radiation environments [1-3]. High-temperature pressure sensors are particularly attractive for automotive (fuel engines), manufacturing (down-hole drilling operations), energy (petrochemical refineries) and environmental (HVAC systems) applications. A single crystal SiC-based sensor diaphragm with piezoresistors can withstand the dynamic pressure changes encountered in such harsh environments. However, machining of such thin diaphragms remains as a formidable challenge.

Amongst 200 or more polytypes of SiC [4] only three types -- 3C-SiC, 6H-SiC, and 4H-SiC -- could be grown in single crystalline form for use in microelectronics and MEMS devices. The rigid process control requirements in the single crystal growth techniques for obtaining defect-free 3C-SiC wafer [5] prevented its commercial availability. On the other hand, single crystalline 4H and 6H wafers are readily available in various sizes (ranging from 50.8 mm - 100 mm).

Conventional fabrication of SiC for MEMS applications includes Reactive Ion Etching (RIE), Electron Cyclotron Resonance (ECR), and Deep Reactive Ion Etching (DRIE) which suffer from poor etch selectivity, slow etch rates and require the use of masks in the

etch field [6, 7]. Laser ablation is emerging as an alternative technique, offering a clean, simple and maskless method with higher etch rates. In fact, etch rates ranging from 0.47-1.8 $\mu\text{m}/\text{pulse}$ have been achieved using nanosecond pulsed lasers on 4H-SiC polytypes [8-10]. SiC has high optical absorption at UV wavelengths [11] and shows nearly linear correlation between the number of pulses and ablation depth [12]; this makes UV lasers as excellent choices for micromachining of SiC-based MEMS devices.

In the nanosecond or longer pulse regime, when the incident photons have sufficient energy to overcome the bandgap, single-photon absorption occurs, which causes the jumping of electrons from the valence band to the conduction band. It may be noted that the photon energy corresponding to 248 nm (5 eV) is much higher than the bandgaps of 4H-SiC (3.26 eV) and 6H-SiC (3.03 eV); this in turn facilitates single-photon absorption through direct electronic interaction with the bandgap of SiC. The excited electrons relax down to the bottom of conduction band, resulting in the emission of phonons. As more electrons jump to the conduction band, the phonon energy increases, leading to the lattice disorder, bond breaking and subsequent ablation [13]. This process, however, is not sufficient to cause direct bond scission, ionization or atomic emission in SiC as the minimum energy required to break the bonds, i.e. the sum of electron affinity (~ 4.0 eV) and bandgap energy (~ 3 eV), is greater than the energy corresponding to a photon (5 eV) [13, 14]. The bond scission is supposed to be caused by cascade excitation through localized electron states [15].

In this paper, we report the ablation behavior of single crystal 4H-SiC and 6H-SiC wafers when subjected to 23 ns pulsed, 248 nm wavelength excimer laser. The ablation mechanisms were identified as a function of energy fluence. Furthermore, trenches

were demonstrated to show the capability of excimer laser micromachining in fabricating sensor diaphragms.

2. Experimental Details

Single crystalline wafers of the types 4H and 6H (n-type semiconductor, nitrogen dopant density $\sim 10^{17}/\text{cm}^3$, silicon face polished/epi ready) with 50 mm diameter and 250 μm thick were procured from Cree, Inc (NC, USA). The wafer has less usable surface area (50%) than Cree's standard research grade (70%). Table 1 lists the electronic, thermal and optical properties of these two polytypes relevant to laser micromachining.

A 248 nm (KrF) excimer laser (Lambda Physik Model 110i) was employed to study the ablation characteristics and for micromachining purpose. Figure 1 shows a photograph of the excimer laser system, the specifications of which are listed in Table 2.

Table 1: Physical properties of single crystal SiC polytypes

Property	4H-SiC	6H-SiC	Reference
Reflectivity at 248 nm	0.26	0.3	[16, 17]
Absorption Coefficient at 248 nm (m^{-1})	[†] 6×10^5	5×10^6	[18-20]
Thermal Diffusivity, m^2/sec	1.7×10^{-4}	2.2×10^{-4}	[21]
Thermal Conductivity, W/m-K	370	490	[21]
Density, kg/m^3	3200	3200	[22]
Specific Heat, J/kg-K	690	690	[23]

[†] Interpolated from Reference [19]

Table 2: Specifications of laser used in this investigation

Wavelength	Max. pulse energy	Pulse width	Max. rep rate	Max. average power	Beam size	Beam profile
248 nm	300 mJ	23 ns	100 Hz	30 W	12 x 23 mm	Multimode



Figure 1. Photograph of Excimer laser system (Lambda Physik)

Figure 2 shows the schematic diagram of beam delivery unit used with the excimer laser system. The large beam was passed through a beam delivery unit consisting of 200 mm x 100 mm telescope lens, adjustable razorblade aperture, 90° turning mirror and 100 mm image lens. The telescope lenses are arranged in a standard telecentric (afocal) configuration and serve the purpose of increasing the energy density on the aperture by a factor of four. The turning mirror redirects the laser beam to the workpiece. The image lens is used to project the aperture on the workpiece at a given demagnification ratio which is 7x in this study. The demagnification, M is defined as $M = O/I$ where O is the distance from the aperture to the image lens and I is the distance from the image lens to the workpiece.

The laser pulse energy and repetition rate were varied from 10 mJ to 200 mJ and 1 Hz to 50 Hz respectively for ablation. The spot size was approximately 250 μm x 100 μm . The energy fluence was varied between 0.8 Jcm^{-2} to 25 Jcm^{-2} . All experiments were carried out in an atmosphere where N_2 gas was directly flowing over the exposed surface so that it can mitigate the formation of SiO_2 caused by the oxidation of SiC surface. Ablation depths and profiles were obtained using a Zygo optical profilometer.

The energy fluence and repetition rate were set constant at 7 Jcm^{-2} and 10 Hz respectively for micromachining trenches. The spot size on the sample was increased to approximately $1500 \mu\text{m} \times 500 \mu\text{m}$. The sample was held stationary with respect to laser beam, thereby reducing the possibility of any ramp features that may occur on the surface due to relative motion of the beam. Following laser micromachining, the samples were cleaned using $\text{HCl:H}_2\text{O:H}_2\text{O}_2$ (1:1:1) for 5 minutes and then treated with $\text{HF:H}_2\text{O}$ (1:1) for 7 minutes. The samples were examined in scanning electron microscope (SEM) for debris, feature size and geometry.

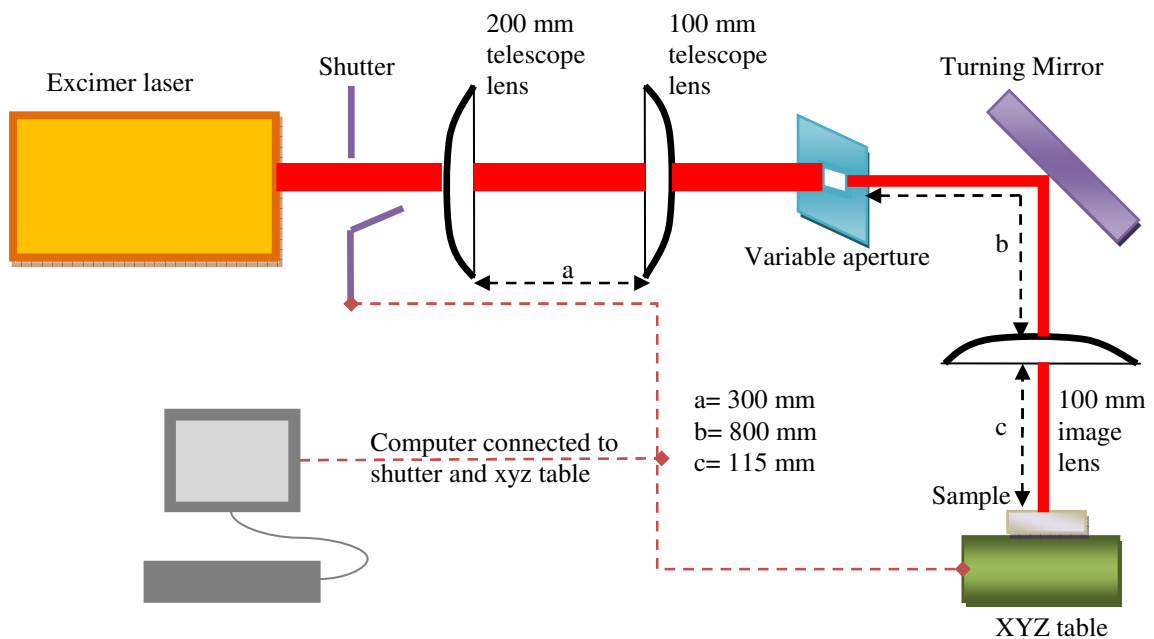


Figure 2: A schematic diagram of beam delivery unit used with the excimer laser

3. Results and Discussion

3.1 Ablation Characteristics

Laser ablation of materials in the UV region may be classified as photothermal or photochemical or a combination of both depending on the material's thermal diffusivity, pulse duration, and absorption coefficient [24, 25]. If thermal penetration depth $L_e = 2(\kappa t)^{1/2}$ is greater than optical absorption depth $L_o = \alpha^{-1}$, thermal ablation dominates (where t is the pulse duration in seconds, κ is the thermal diffusivity, and α is the absorption coefficient of the material). Otherwise, photochemical ablation governs. Using properties given in Table 1 (300 K), L_e and L_o for both polytypes were calculated and listed in Table 3 showing the dominance of photothermal ablation.

Table 3: Calculated values of L_e and L_o with 248 nm excimer laser at 300K

Polytype	4H-SiC	6H-SiC
Thermal penetration depth (L_e)	~ 4 μm	~ 4.5 μm
Optical absorption depth (L_o)	~ 1.7 μm	~ 0.2 μm

Ablation rate (depth of material removed per pulse) was measured for both polytypes using 1 Hz for 50 pulses (Figure 3). The ablation rate follows an exponential curve that agrees with the previous work by Reitano et al using XeCl excimer laser (308 nm) ablation of 6H-SiC crystals [26]. The ablation rate fluctuated very little above a fluence of 15 Jcm^{-2} , indicating a saturation point. The ablation curve can be divided into three different regimes based on the changes in slope, indicating a distinctive mechanism in each region. In this study, it was difficult to measure accurately the ablation depths for fluences below 3 Jcm^{-2} due to very small depths and formation of recast layers that mask the ablated zone. Three-dimensional surface map and depth profiles for both polytypes are shown in Figures 4 and 5

respectively, and it can be seen that the ablation rate does not change significantly when the fluence was increased from $0.8 - 1.25 \text{ Jcm}^{-2}$. Furthermore, the bottom surface of 6H-SiC was observed to be more irregular relative to 4H-SiC (Figure 5). However, based on our experimental data at lower fluences, it was observed that ablation rate increases considerably $\sim 0.01 \mu\text{m}/\text{pulse}$ after a certain threshold. The corresponding fluence was interpolated to be ($\sim 1.6 \text{ Jcm}^{-2}$) for 4H-SiC and ($\sim 1.9 \text{ Jcm}^{-2}$) for 6H-SiC. A higher bandgap and presence of fewer Si-C bilayers in the unit cell of 4H-SiC are believed to be responsible for a lower fluence than that of 6H-SiC.

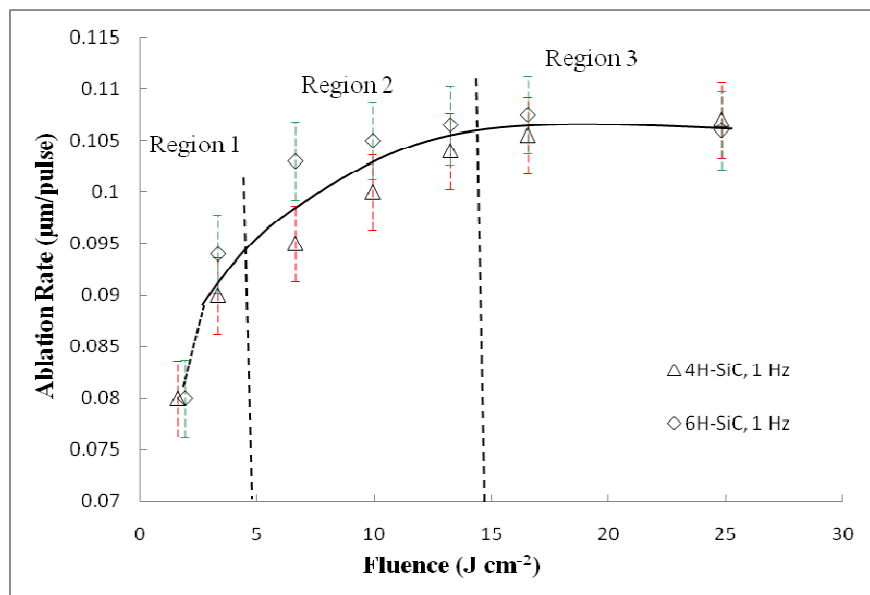


Figure 3: Ablation rate as a function of fluence for SiC

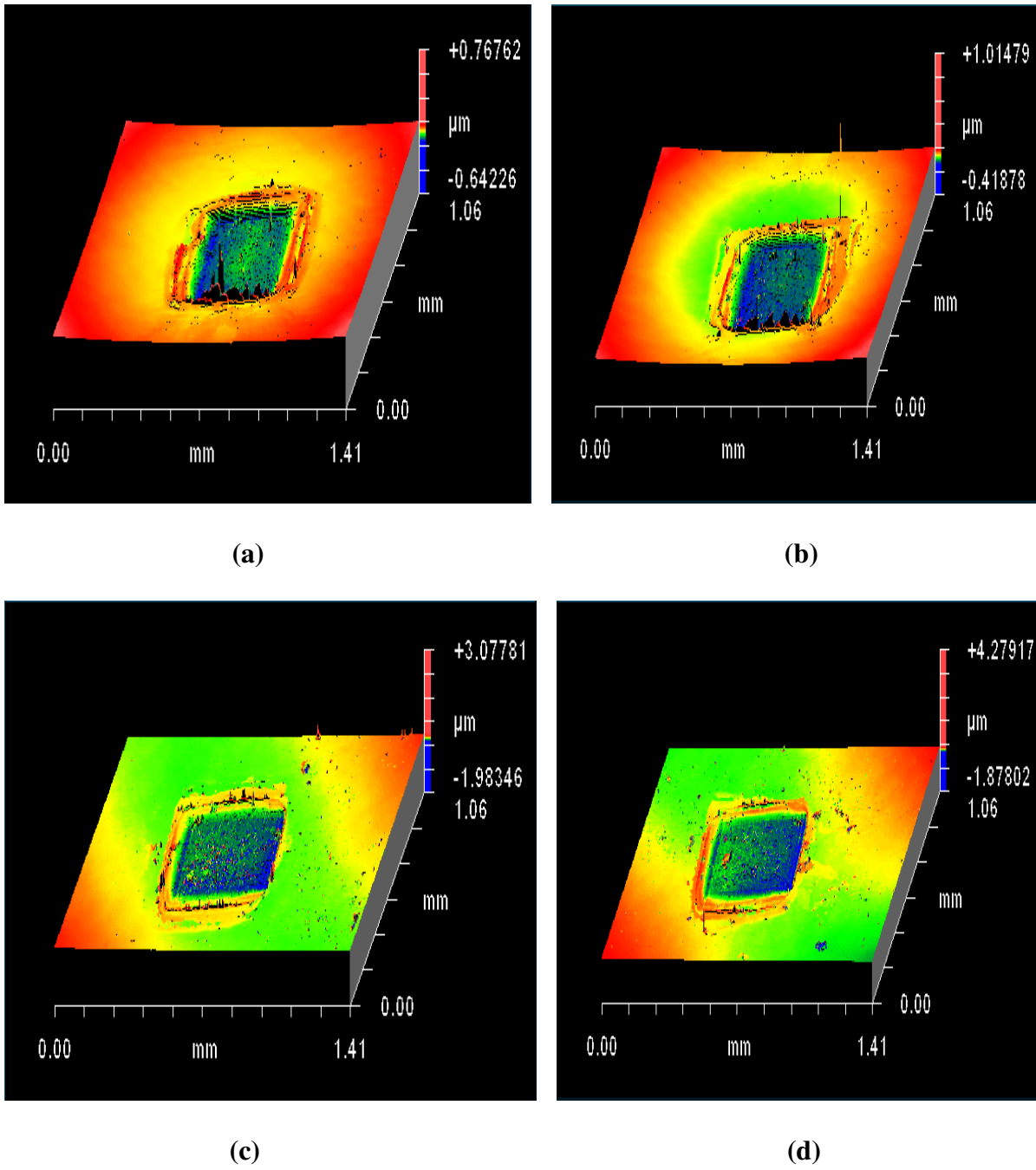


Figure 4: Surface map for (a) 4H-SiC, 0.85 Jcm⁻², (b) 4H-SiC, 1.24 Jcm⁻², (c) 6H-SiC, 0.85 Jcm⁻²; and (d) 6H-SiC, 1.24 Jcm⁻²

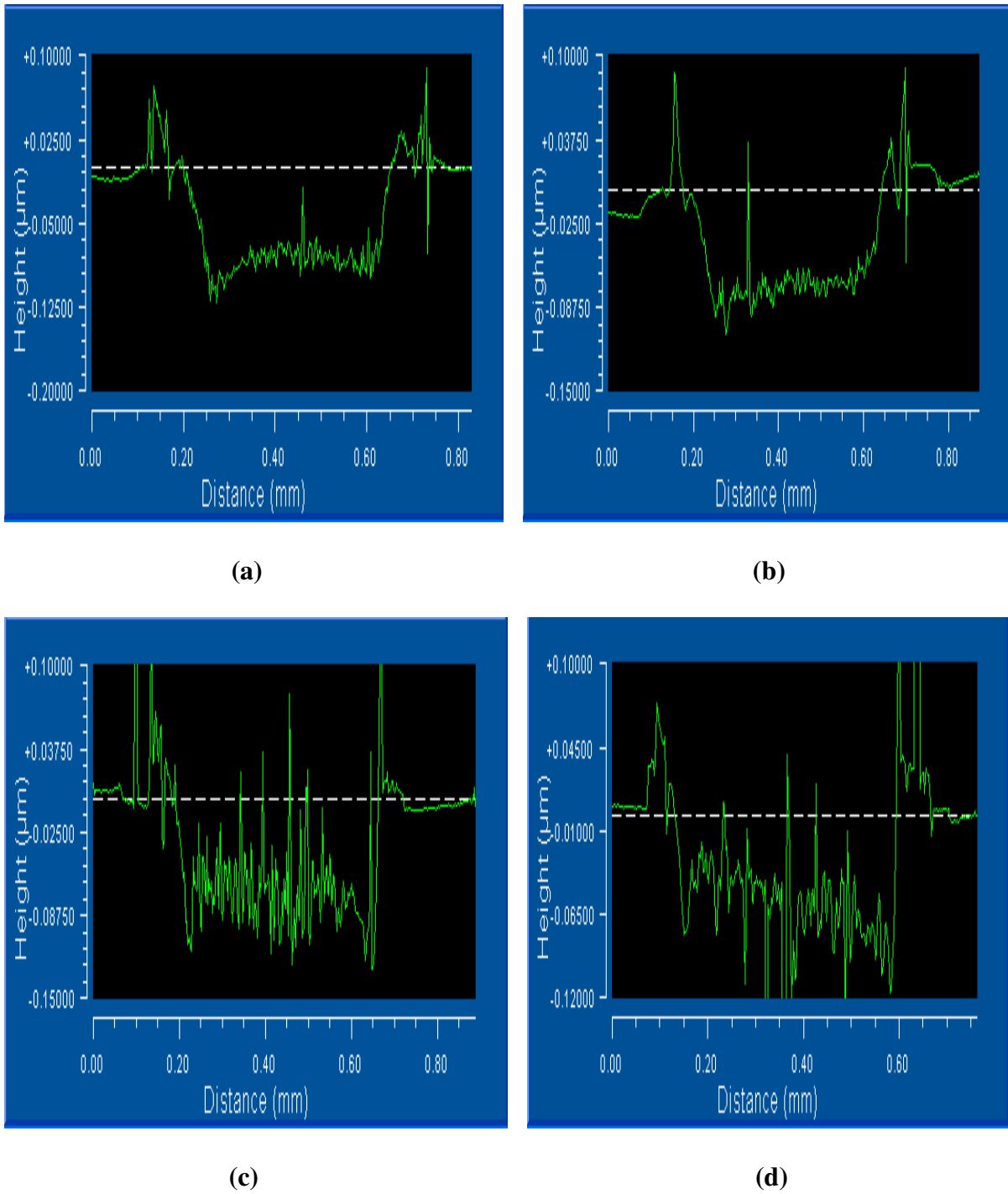


Figure 5: Surface profile for (a) 4H-SiC, 0.85 Jcm⁻², (b) 4H-SiC, 1.24 Jcm⁻², (c) 6H-SiC, 0.85 Jcm⁻²; and (d) 6H-SiC, 1.24 Jcm⁻²

Ablation depth as a function of number of pulses was also measured for both polytypes and results are compared as shown in Figure 6. Ablation rate was found to be linear and nearly identical for both SiC. Such linear relationship was also noted in a previous investigation [12] and is in accordance with the single-photon absorption mechanism which does not account for any incubation effects. The error bars indicate a negative ablation depth which corresponds to surface elevation at low pulses.

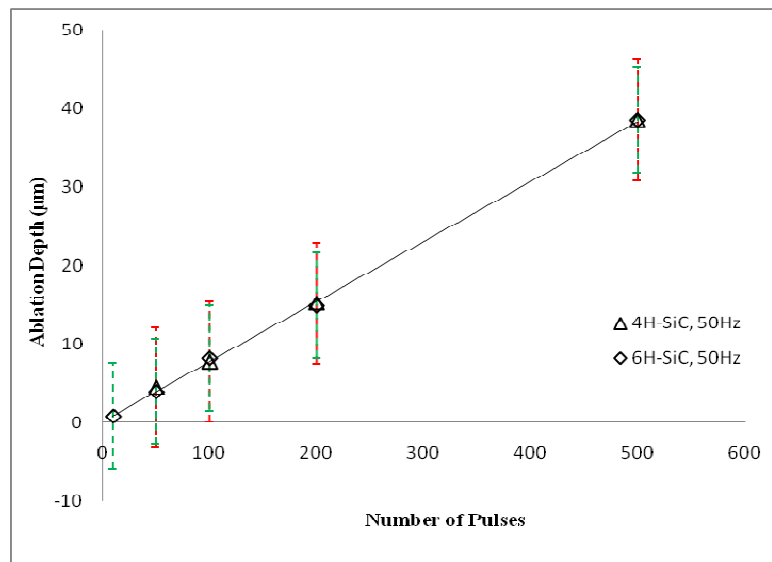


Figure 6: Ablation Depth vs Number of Pulses for SiC using 8 J cm^{-2} at 50 Hz

A. Heat Diffusion Model:

The heat diffusion properties of a material can play a significant role in determining its ablation rate with ns pulses since thermal diffusion takes place at a time scale much shorter than nanoseconds [27]. It reduces the temperature at the focal spot (machining spot) which also lowers the accuracy of micromachining operation and melts an area that is much larger than the laser spot size. Moreover, the thermal penetration depth, L_e , is directly proportional to the diffusivity (κ) of the material, as reported in an earlier section. At this point, it is

important to note that κ is temperature dependent, and so should be L_e . Thus, it is essential to consider thermal diffusion when defining the ablation rate as a function of fluence. The ablation depth per pulse can be expressed by modifying the Beer Lambert law (in terms of L_e) as [28]:

$$D = 2(\kappa t)^{1/2} \ln \frac{F_i}{F_t} \quad (1)$$

Thermal diffusivity for SiC varies with temperature according to the relation given as $\kappa = \frac{146}{(T-207)} \text{ cm}^2/\text{s}$ for $300 < T < 2300 \text{ K}$ [23]. An average value based on this relation was used for thermal diffusivity in this study wherever applicable. The ablation depth was calculated using equation (1), and results were compared with experimental data as shown in Figure 7. The calculated results are observed to be much higher than the experimental data; this overestimation could be due to the simplifications in the heat diffusion model which assumes that the whole diffusion zone is subjected to temperatures higher than the vaporization, and neglects energy losses due to plasma formation and reflection at the surface.

B. Effective Absorption Model:

It has been reported that assuming absorbed laser energy and thermal energy distribution are independent of each another, a new term called effective absorption coefficient (α_{eff}) can be defined as [29]:

$$\alpha_{\text{eff}} = [\alpha^{-1} + 2(\kappa t)^{1/2}]^{1/2} \quad (2)$$

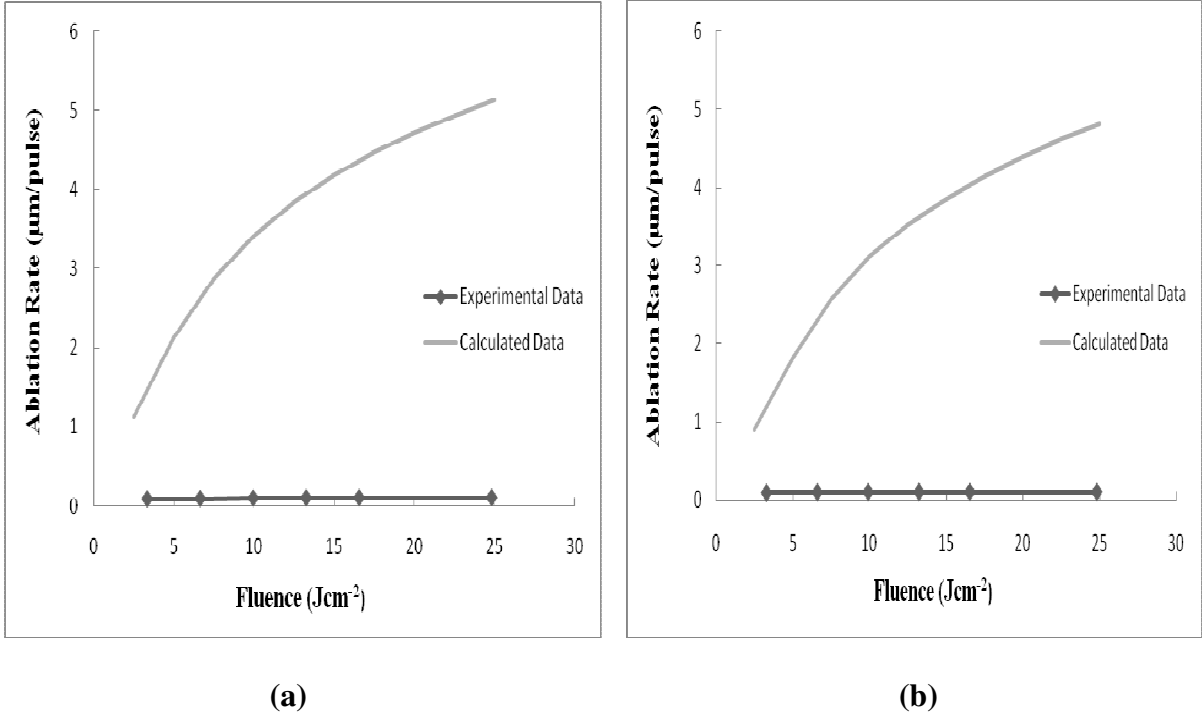


Figure 7: Comparison of experimental and calculated ablation rate based on heat diffusion model for (a) 4H-SiC; (b) 6H-SiC

Thus, substituting the value of α_{eff} in Beer-Lambert equation, the modified expression for ablation depth per pulse can be written as:

$$D = [\alpha^{-1} + 2(\kappa\tau)^{1/2}]^{1/2} \ln \frac{F_i}{F_t} \quad (3)$$

The ablation depth was calculated using equation (3), and the results were compared with the experimental data as shown in Figure 8. The calculated results are much higher than those obtained in the previous model; the increase is, however, more pronounced in 4H-SiC. This behavior is primarily attributed to a higher absorption coefficient of 6H-SiC compared to that of 4H-SiC, since the average value of thermal diffusivity is same for both polytypes above room temperature.

In both models A and B, the assumption that the process lasts only as long as the pulse duration (t) may lead to this overprediction. The maximum temperature rise can occur at longer ' t ' particularly for higher depths [30]. We now turn our attention to the other photothermal models that could give a better correlation between the ablation rate and incident fluence.

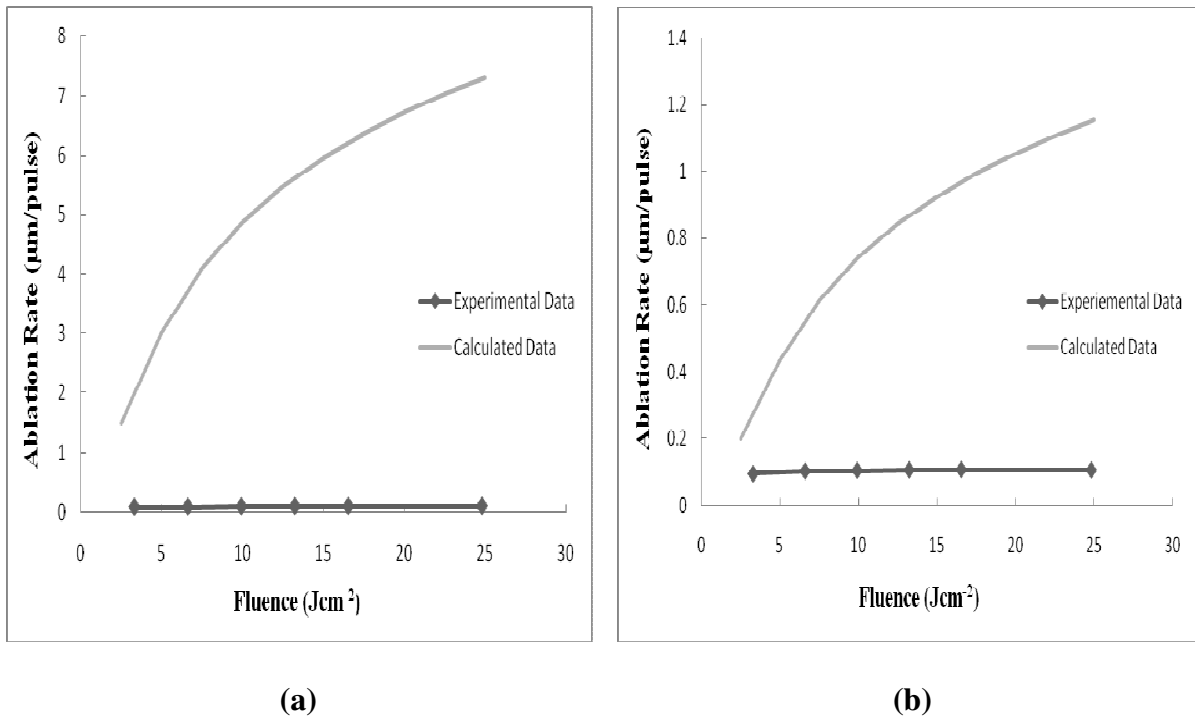


Figure 8: Comparison of experimental and calculated ablation rate based on effective absorption model for (a) 4H-SiC; (b) 6H-SiC

C. Energy Balance Model:

In order to understand the ablation mechanism corresponding to three regimes in Figure 4, it is imperative to know how the laser energy is distributed to the bulk and vapor phase. This distribution strongly depends on optical and thermodynamic properties of the irradiated material as well as the laser parameters used. The laser energy (E) incident on the target

surface increases the target temperature by an amount ΔT , governed by the simplest form of (adiabatic) energy conservation equation as $E = mC_p \Delta T$, where m is the irradiated mass and C_p is the specific heat of target material. The above equation can be modeled to estimate the temperature rise (ΔT) with the fluence increase (F) [31]:

$$\Delta T = \frac{(1 - R) F}{\rho C_p (2 \kappa t)^{1/2}} \quad (4)$$

where R is the reflectivity and ρ is the density of the target material.

Figure 9 shows the temperature distributions for both the polytypes corresponding to our experimental fluence range based on equation 4. These temperatures are in close agreement with a heat transfer model shown in the next section.

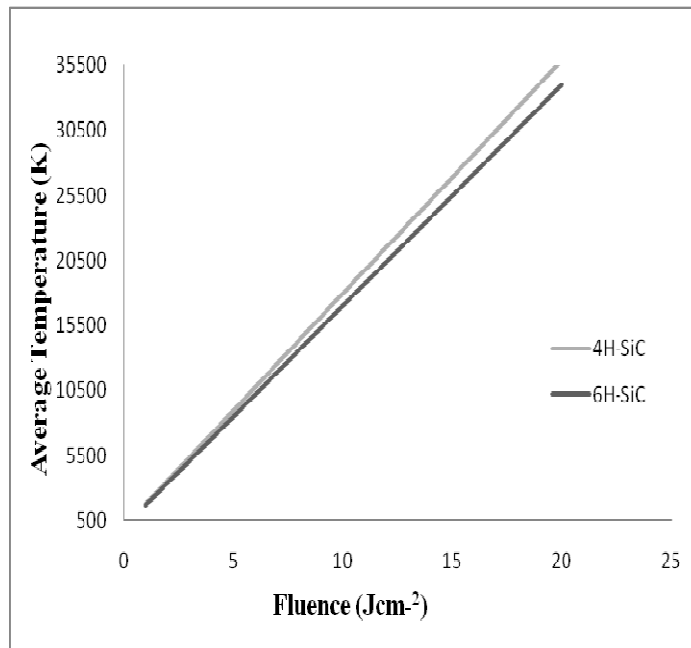


Figure 9: Plot showing distribution of the average temperatures of the ablated zone as a function of fluence based on energy balance model for both SiC

D. Heat Transfer Model:

It has been reported that the rate at which heat is transferred within a material depends on the temperature gradient and thermal conductivity of the material [32, 33]. The losses due to heat conduction are considerable for all materials at all fluences. The absorbed power density can be modeled as the heat flux into the SiC surface and the temperature distribution $T(x,t)$ can be estimated by solving the heat transfer equation for a semi-infinite solid in one-dimension, written as [34]:

$$T(x,t) = \frac{I_0}{k} \sqrt{\frac{4\kappa t}{\pi}} \times \left(e^{-x^2/4\kappa t} - x \sqrt{\frac{\pi}{4\kappa t}} \operatorname{erfc}\left(\frac{x}{\sqrt{4\kappa t}}\right) \right) \quad (5)$$

where I_0 is absorbed power density at the surface and k is the thermal conductivity of material.

It is important to note that both thermal conductivity and diffusivity in the above equation are temperature-dependent. Therefore, an average value of both the quantities was calculated using the data in Table 1, and the following relationship: $\kappa = \frac{146}{(T-207)} \text{cm}^2/\text{s}$ for

$300 < T < 2300 \text{ K}$ and $k = \frac{611}{(T-115)} \text{Wcm}^{-1}\text{K}^{-1}$ for $300 < T < 2300 \text{ K}$ [23]. Temperatures were

calculated from the surface to the depth ($= L_e$). The results, shown in Figure 10, appear to be in good agreement with the energy balance model. Moreover, there is a good similarity in the temperature distribution for both the polytypes. We now turn our attention to detail the ablation mechanism in the three different regimes.

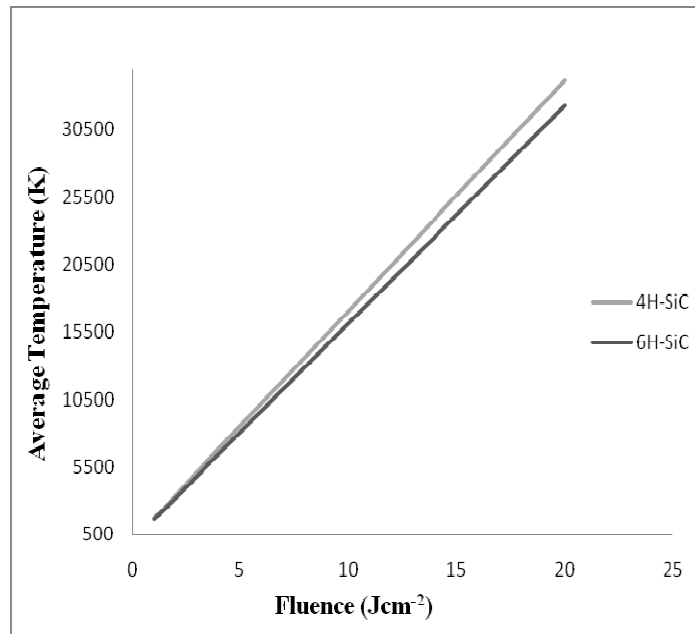


Figure 10: Plot showing distribution of average temperature of the ablated zone as a function of fluence based on heat transfer model for both SiC

Region 1 ($\leq 5 \text{ Jcm}^{-2}$)

Decomposition Mechanism ($< 1.25 \text{ Jcm}^{-2}$)

It has been reported that SiC decomposes into silicon gas and solid carbon at temperatures ranging from 1600 K to 2400 K, and the carbon may then react further with SiC and silicon gas to form other vapor species such as SiC_2 and Si_2C [35, 36]. For this temperature range, the fluence range was determined using both energy balance and heat transfer models at which decomposition occurs. The corresponding fluence values are listed in Table 4. The results indicate that SiC decomposes well below a fluence of 1.25 Jcm^{-2} .

Table 4: Estimation of fluence range at which SiC decomposes

Fluence (J cm⁻²)	* Temperature (K) based on Energy Balance model	* Temperature (K) based on Heat Transfer model
1	1730	1640
1.1	1920	1835
1.2	2100	1950
1.25	2340	2280

*** Average temperatures for both polytypes**

Vaporization Mechanism (1.25 – 5 Jcm⁻²)

It is a well known fact that when a high-power laser beam (laser intensity $\geq 10^8$ W/cm²) irradiates on a target surface, laser energy is absorbed by the target and vapor is formed. Several models have been reported that consider the vaporization characteristics of semiconductors with nanosecond pulsed lasers [34, 37, 38]. In a study done on silicon melting using a nanosecond pulsed laser, the relaxation time (τ_m) at which melting occurs is given by [38]:

$$\tau_m = \left(\frac{3(T_m - T_0)^2 c \rho k}{4I_0^2} \right) \quad (6)$$

where c is the heat capacity, ρ is the density, k is the thermal conductivity, T_m is the melting temperature and T_0 is the initial temperature of the target material. Using the values given in Table 1 and assuming T_m for carbon as equal to 4000 K [39, 40], τ_m was plotted as a function of fluence (Figure 11). It can be observed that the decomposition products begin to melt at fairly low fluences as predicted in the previous research [26]. The relaxation time, τ_m decreases rapidly as the fluence reaches a value ~ 5 Jcm⁻² indicating the extent of melting and subsequent vaporization in this region. To validate our experimental data, τ_m was set equal to the pulse duration time (23 ns) and an approximate melting threshold fluence was determined

to be $\sim 1.5 \text{ Jcm}^{-2}$ for both polytypes. Threshold fluence in our experimental data corresponds to melting threshold. It can, therefore, be inferred that ablation mechanism in Region 1 is primarily driven by melting of carbon followed by vaporization of carbon and silicon species which are formed as a result of SiC decomposition.

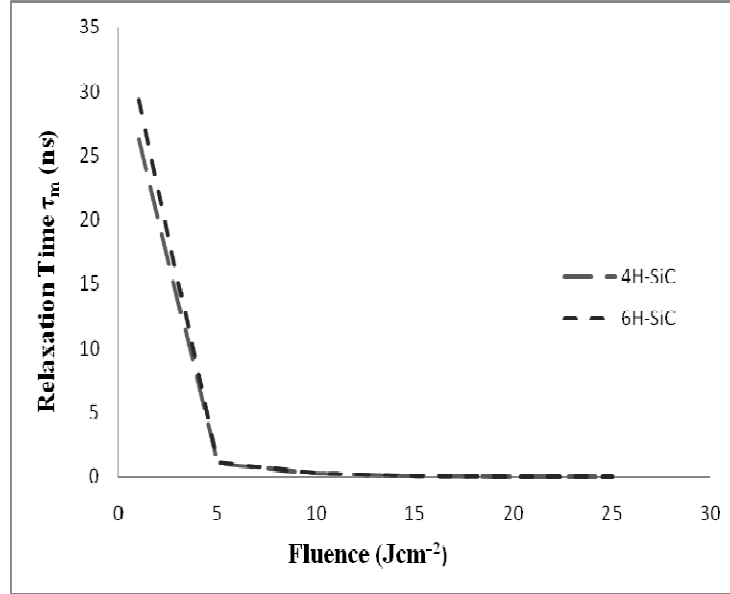


Figure 11: Relaxation time (τ_m) as a function of laser fluence for both SiC polytypes

To determine the ablation rate in Region 1, we calculate the evaporation rate of the melt under the influence of laser fluence. The evaporation rate $G(T)$ can be expressed as a function of temperature (T) given by the equation:

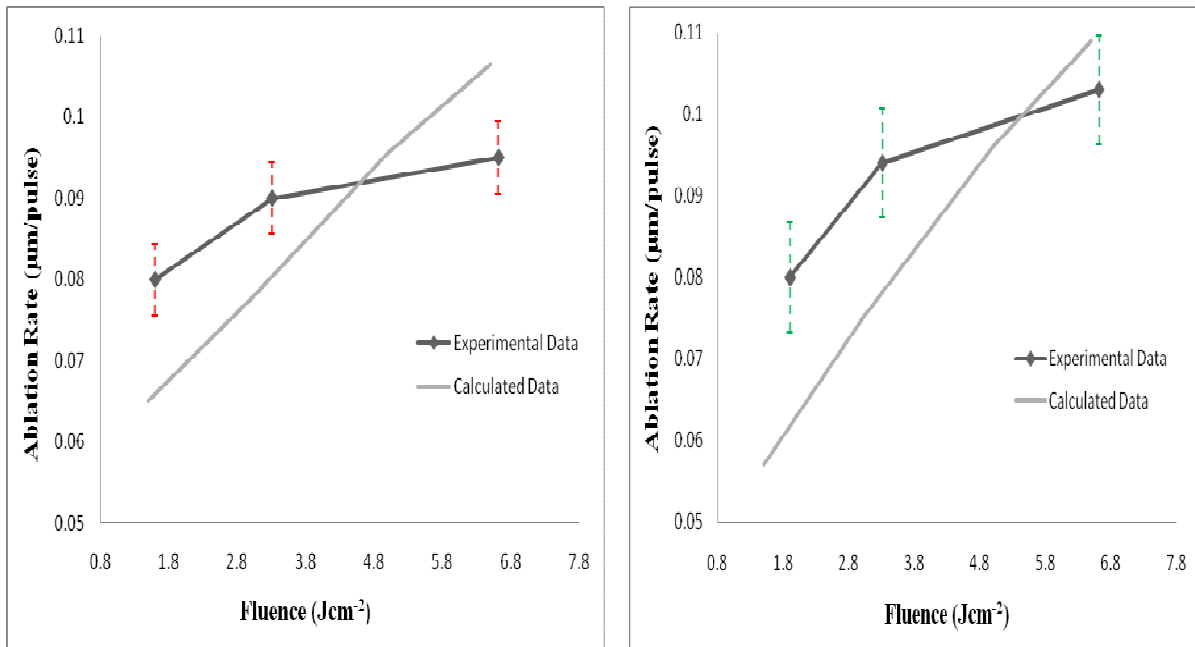
$$G(T) = p_v(T) \left(\frac{M}{T} \right)^{1/2} \quad (7)$$

where p_v is the vapor pressure and M is the molecular weight of the material.

The vapor pressure above the surface is given by the Clausius-Clapeyron equation as [41, 42]:

$$p_v = p_0 \exp \left[\frac{M \Delta H_v(T_b)}{k_b} \left(\frac{1}{T_b} - \frac{1}{T} \right) \right] \quad (8)$$

where $\Delta H_v(T_b)$ is the vaporization enthalpy at boiling temperature (T_b), k_b is the Boltzmann constant and p_0 is atmospheric pressure taken as 1 atm. The value for enthalpy formation of Si was used as the vaporization enthalpy. The results were compared with experimental data as shown in Figure 12. The model underestimates the experimental data for fluences ($< 5 \text{ Jcm}^{-2}$) that could be due to the evaporation of carbon which was not considered. At higher fluences, however, the experimental data was lower than that predicted by equation (7) which can be attributed to the development of a recoil pressure due to evaporated material [34].



(a)

(b)

Figure 12: Comparison of experimental and calculated ablation rate in Region 1 for (a) 4H-SiC; (b) 6H-SiC

Region 2 ($5 \text{ Jcm}^{-2} - 15 \text{ Jcm}^{-2}$)

It has been reported that one of the underlying mechanisms causing ablation of semiconductors using nanosecond pulsed lasers is explosive boiling or phase explosion [34, 43-45]. Explosive boiling occurs when the surface temperature of the ablated material reaches its thermodynamic critical temperature value (T_c). The critical temperature of SiC, however, is taken as 5000 K (critical temperature of Si) in an ablation study of SiC with a 248 nm excimer laser [43]. The energy balance and heat transfer models indicate that at $\sim 5 \text{ Jcm}^{-2}$, the decomposition products of SiC reach T_c . Explosive boiling of Si occurs above this fluence range and drives the ablation in this region. Consequently, large vapor bubbles are formed in the superheated melt layer which receives large density fluctuations near the critical state ($\sim 0.84 T_c$) [46, 47]. The rapid expansion of these vapor bubbles results in homogeneous nucleation that leads to the violent ejection of mass in the form of particulates that increases the ablation rate [48]. An estimation was made for the laser irradiance needed to induce explosive boiling in superheated liquid silicon using heat transfer model (equation 5). I_0 was evaluated for $T(x,t) = 0.84 T_c$. The thermal properties of silicon were taken from References [49, 50]. The fluence was computed to be $\sim 2 \text{ Jcm}^{-2}$ which is less than the experimental value of $\sim 5 \text{ Jcm}^{-2}$. The differences could be attributed to the negligence of carbon removal and the formation of plasma which absorbs a portion of laser energy incident on the target. Plasma effect can, however, be minimized by a shielding gas that has high ionization potential such as helium [51].

The thickness of melt layer can be approximated as equal to the critical radius (r_c) of the vapor bubble at which it will explode as given by the expression [44, 52, 53]:

$$r_c = \frac{2\sigma}{p_v(T_l) \exp\{v_l[p_l - p_v(T_l)]/R_v T_l\} - p_l} \quad (9)$$

where σ is the surface tension that ranges from 0.14 – 0.73 N/m [44], $v_l = 1/\rho_l$ (density of superheated liquid), p_l is the pressure of liquid silicon layer approximated to be 0.54 p_v [44], T_l is the temperature of superheated liquid approximated to be 0.84 T_c [54, 55] and R_v is the gas constant.

The critical radius was estimated to be in the range of 2.25 – 10 μm as shown in Figure 13. The critical diameter of the bubble is much larger than the thermal penetration depth for silicon ($\sim 2 \mu\text{m}$). Therefore, it can be inferred that the bubble cannot grow to its critical size during the laser pulse, and will burst preventing the homogeneous nucleation. It has been suggested that the vapor bubbles take a characteristic time (τ_c) to grow to the critical size (r_c) [53, 56, 57]. The expression for τ_c can be written as [57]:

$$\tau_c = r_c \left\{ \frac{2}{3} \left[\frac{T_l - T_{sat}(p_l)}{T_{sat}(p_l)} \right] \frac{L_{ev} \rho_v}{\rho_l} \right\}^{1/2} \quad (10)$$

where $T_{sat}(p_l)$ is the saturation temperature at the superheated liquid pressure determined from Clausius-Clapeyron equation and L_{ev} is the latent heat of vaporization for silicon.

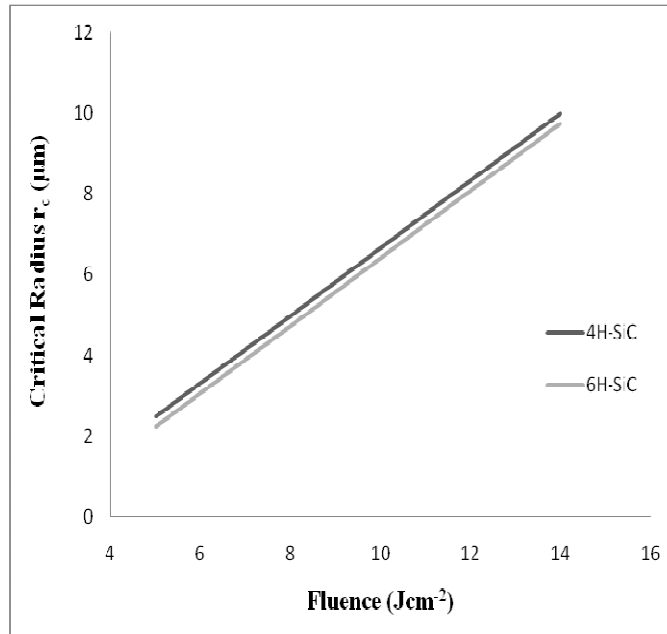


Figure 13: Critical Radius as a function of fluence in Region 2 for both SiC

The characteristic time was estimated to be in the range of 150 – 500 ns. Assuming upper bound limit as the characteristic time delay (500 ns), it can be stated that the homogeneous nucleation can take place in Region 2 after ~ 20 pulses in this study. To validate our model, we approximate the experimental ablation rate based on the calculated results shown in Figure 14. It can be observed that the ablation rates are still larger than the experimental data. This could be due to the underestimation of T_c and negligence of energy losses due to plasma shielding.

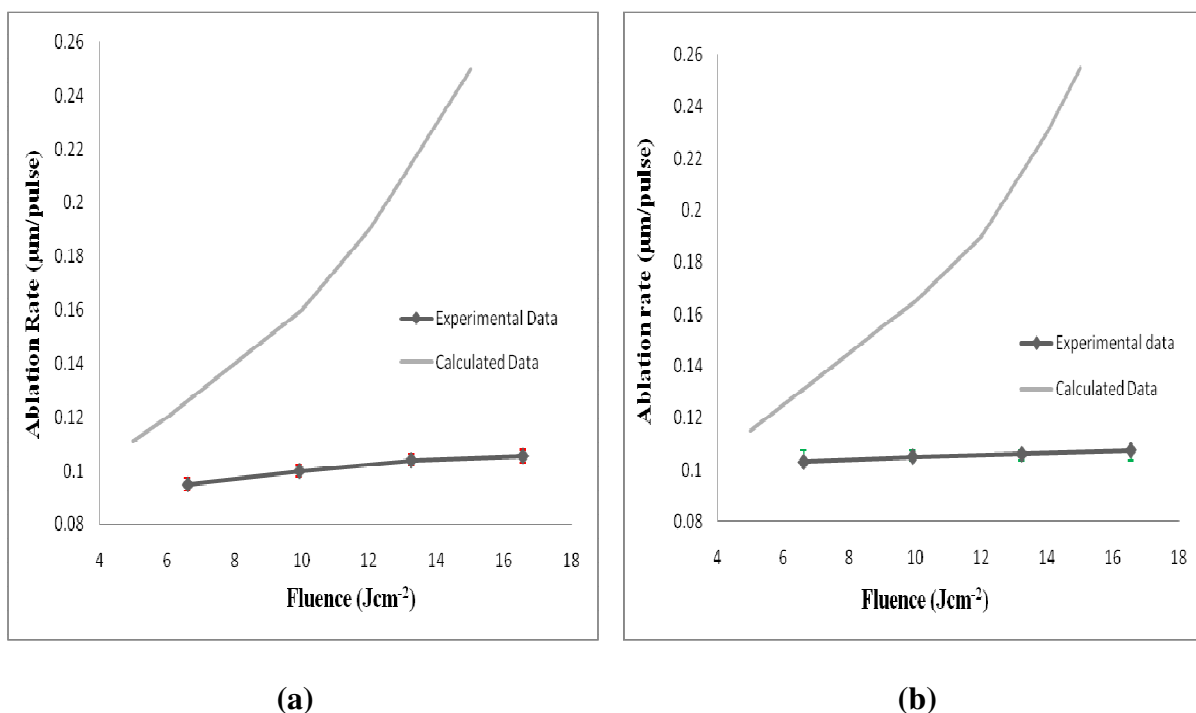


Figure 14: Comparison of experimental and calculated ablation rate in Region 2 for (a) 4H-SiC; (b) 6H-SiC

Region 3 (15 Jcm⁻² – 25 Jcm⁻²)

It has been reported that at high laser power intensities (0.5 GW/cm² - 10 GW/cm²), which corresponds to the fluence range in Region 3, the surface temperature of the material may still increase, however, its contribution to the ablation process is not so pronounced [58]. This supports our experimental data and temperature models. The impact of plasma shielding in this region is so large that a significant amount of laser energy is screened off from reaching the target surface. In fact, Chen et al reported that the fraction of laser energy absorbed by the plasma drastically increases from approximately 1% to 48%, with laser irradiance varying from 0.19 GW/cm² to 0.9 GW/cm² [59]. The two dominant mechanisms for the absorption of laser light are: inverse Bremsstrahlung and photoionization of excited atoms [58-60]. A

theoretical prediction of the degree of plasma absorption near this fluence range is, however, difficult due to computational complexities and lack of material properties.

3.2 Machining Results

Figures 15a to 15d shows the profiles and features of excimer laser micromachined trench measuring 1.5 mm x 0.5 mm (120 μm deep, approximately) in 6H-SiC using 85 mJ (7 Jcm^{-2}) at 10 Hz. The presence of recast layers along the sidewall and micro-cracks along the outer edge can be clearly seen. When removing large amount of material for deep structures, the debris re-deposition was very pronounced due to ejected material and re-condensed vapor that forms a loosely adhered film on the surface. SiC decomposes to Si and C at high temperatures and recombines to form highly volatile species as Si_2C and SiC_2 [35]. Phase transition and/or repeated heating and cooling of this layer promotes cracking [61]. The fine debris field was found at a distance of 500 to 700 μm in some instances, and coarse debris was found to have formed near the machined areas. The presence of cracks, recast layers, and ripple patterns (discussed in the next section) illustrates adverse thermal damages associated with UV laser micromachining, and are attributed to vaporization and explosive boiling mechanisms. Post processing such as chemical cleaning may become necessary to eliminate the loosely attached debris as shown in Figure 16.

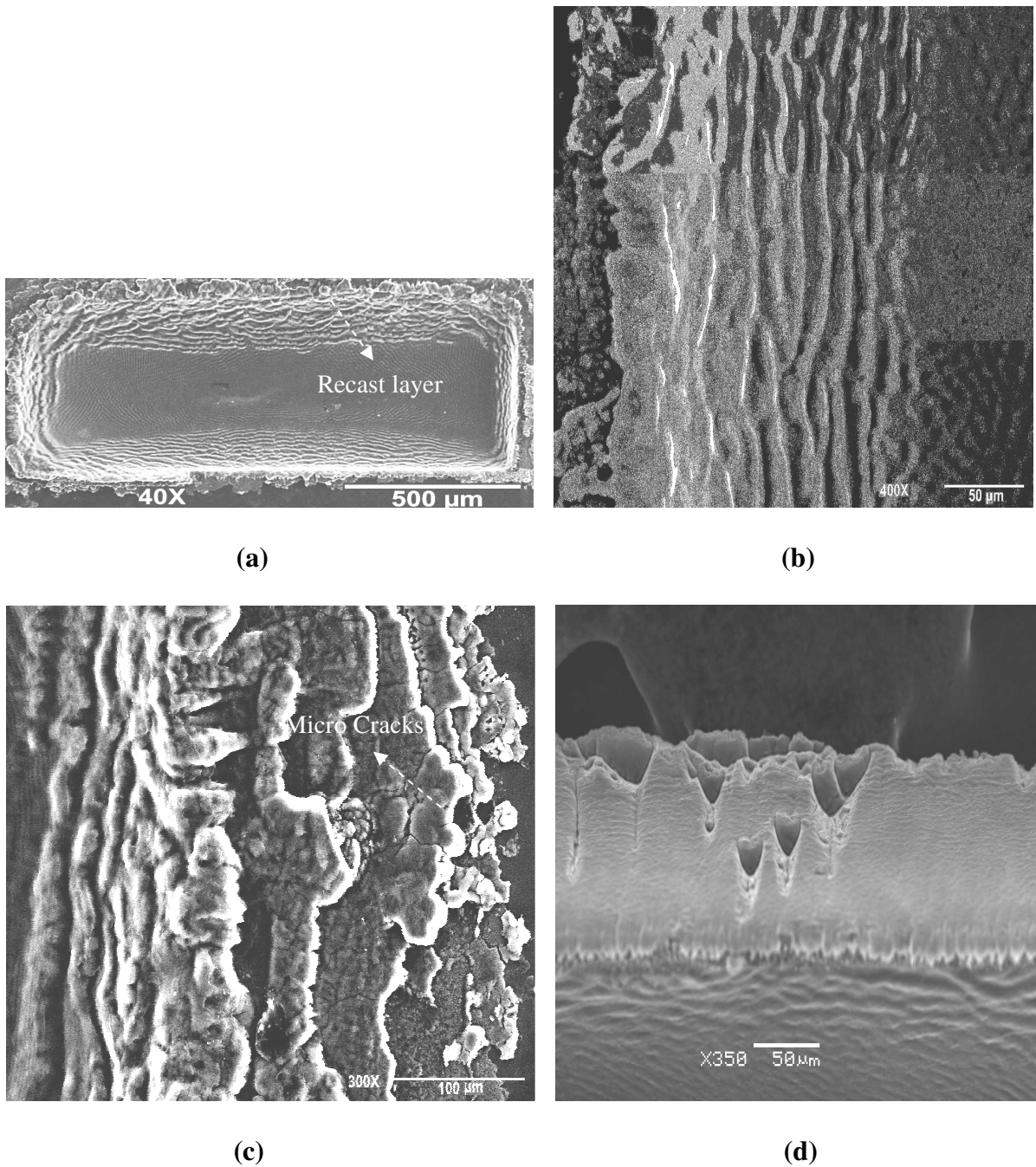


Figure 15: Excimer laser micromachined micro-trench in 6H-SiC showing (a) Cross-sectional view (b) Sidewall (c) Micro-cracks along the outer edge; and (d) Recast layers along the sidewall

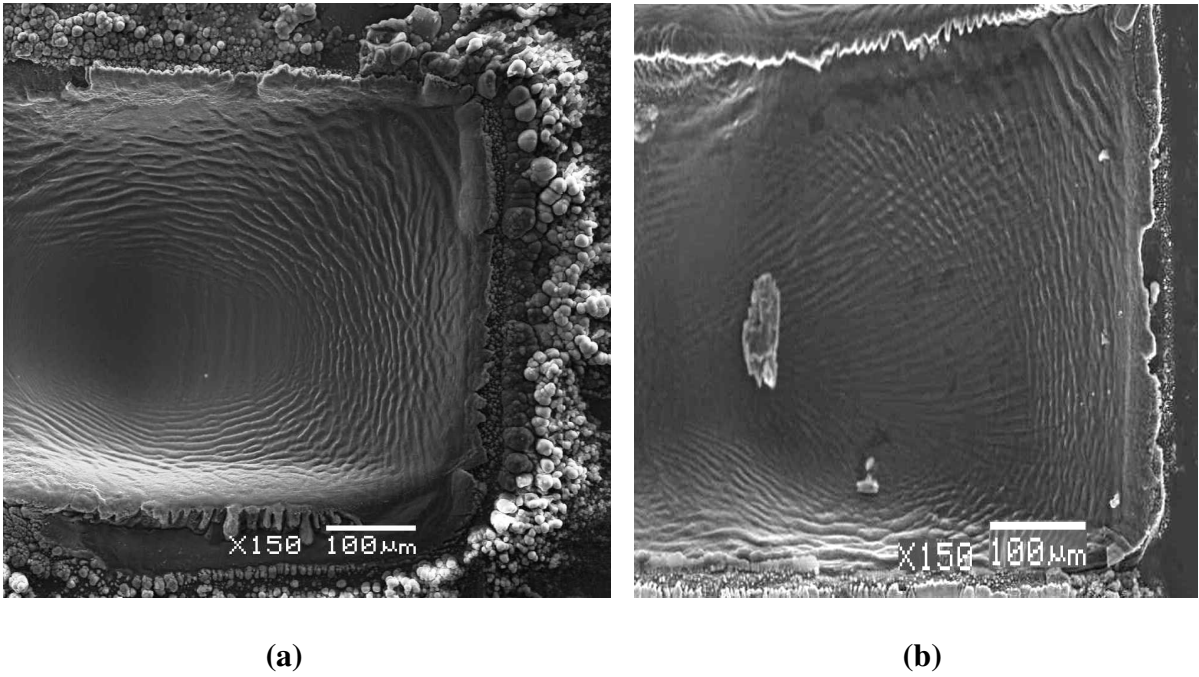


Figure 16: Micro-trench machined in 6H-SiC using 85 mJ at 10 Hz: (a) without post-processing; (b) with post-processing

Figure 17 is the magnified view of the bottom regions of both SiC using 7 Jcm^{-2} with 800 pulses at 10 Hz which display the presence of laser-induced surface structures (also called ripples). Many investigations have shown that laser irradiation over a broad range of wavelengths can create ripple patterns on many different semiconductors, metals, dielectrics, and polymers [62-67]. Based on these studies, such structures can be divided into two categories: (i) resonant periodic structures (RPS) that depend on the wavelength, polarization, and incidence angle of laser radiation, and have a periodicity (Λ) close to its wavelength (λ) [63, 66]. The periodicity can be calculated, with an accuracy of few percent, from Rayleigh's diffraction condition, as:

$$\Lambda = \frac{\lambda}{n_0 [1 \pm \sin\theta]} \quad (12)$$

where n_0 is the index of refraction of the incident medium, and θ is the angle of incidence relative to the surface normal.

(ii) non-resonant periodic structures (NRPS) that are neither related to the wavelength nor to the degree and direction of polarization of the incident beam. NRPS was most probably reported for the first time by Bastow et al. [67]. Structures with a period $\Lambda \sim 10 \mu\text{m}$ were seen in the laser irradiation zone as a result of ruby laser pulses ($\lambda = 0.694 \mu\text{m}$, $\tau_p = 10 \text{ ns}$). More thorough investigations of NRPS have been reported in References [68-70] using non-polarized radiation generated by CO_2 laser sources ($\tau_p = 1.7 \text{ ns}$), and in Reference [71] using XeCl excimer laser ($\lambda = 0.308 \mu\text{m}$, $\tau_p = 30 \text{ ns}$). All of these studies reveal that these structures are independent of wavelength, target material, beam polarization, and details of surface roughness. The exact mechanism through which NRPS occur, however, is not yet fully understood.

The periodicity of ripple patterns observed in our study is of the order (5-10 μm) which is much larger than the wavelength used (0.248 μm), suggesting that NRPS is the operative mechanism. Recently, similar results were observed on SiC using a 248 nm excimer laser [43]. Ursu et al. postulated that NRPS occurs due to the instabilities evolving at the plasma-target interface that cause self-organization of the melt [71]. Other researchers have reported that the presence of a Si/SiO₂ interface in the excimer laser processed part is responsible for the observation of periodic structures [72, 73].

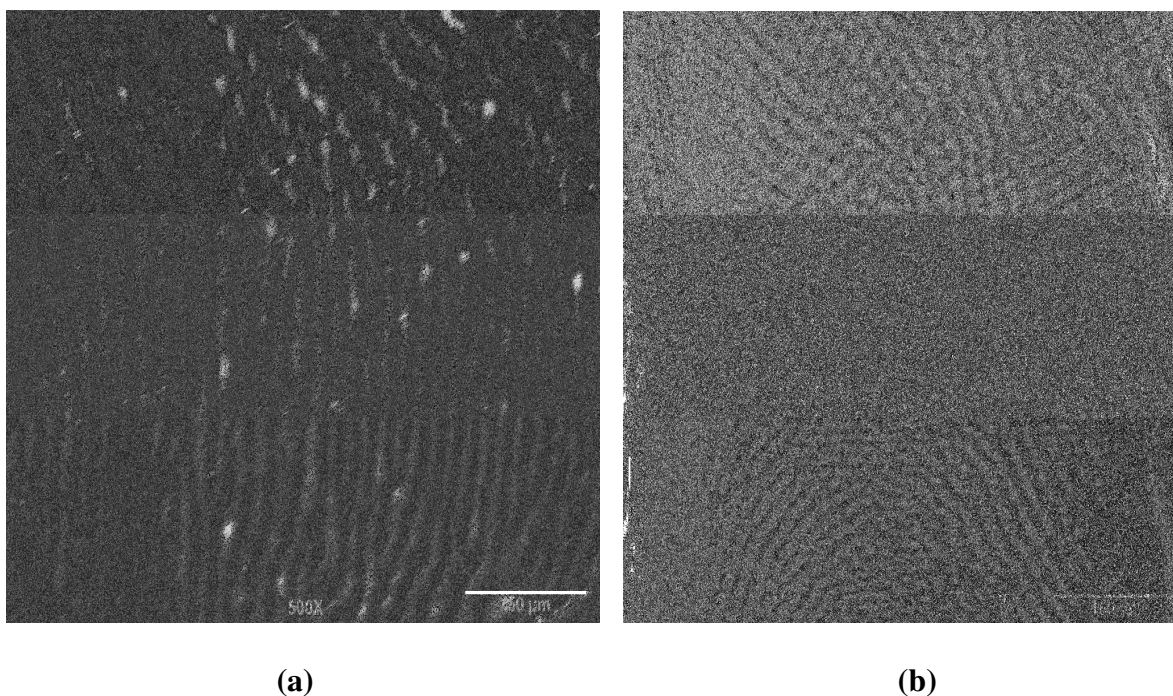


Figure 17: Bottom of a micromachined surface showing ripple patterns in (a) 4H-SiC; (b) 6H-SiC

4. Conclusion

Pulsed laser ablation (at 248 nm) of single crystals of both 4H-SiC and 6H-SiC produced nearly identical ablation characteristics. The increase in ablation rate for energy fluences in the range $0.5 - 1.25 \text{ Jcm}^{-2}$ was not pronounced unlike that of Si. Photothermal processes dominated the ablation in both polytypes. The ablation process began with the decomposition of SiC at fairly low fluences (ranging from $1 - 1.25 \text{ Jcm}^{-2}$) and then at fluences in the range $1.25 - 5 \text{ Jcm}^{-2}$ driven by vaporization of silicon and carbon species formed as a result of SiC decomposition. For fluences $> 5 \text{ Jcm}^{-2}$, explosive boiling (or phase explosion) is believed to occur. At $\sim 15 \text{ Jcm}^{-2}$, the ablation rate reaches a saturation point due to extensive plasma shielding. No single model could explain the ablation behavior of both the polytypes (taking into account its thermodynamic and optical properties), and it is unlikely that such a model

can be developed due to unavailability of their temperature-dependent properties and interplay of various mechanisms. To our knowledge, this is the first time that the ablation characteristics of single crystal 4H-SiC and 6H-SiC were compared over the wide range of fluence.

Micromachining of SiC with the excimer laser is accompanied by the formation of recast layers, micro-cracks, and ripple patterns. Post processing improved the quality of machined features and minimized the thermal damage via chemical cleaning. Thus, excimer laser micromachining is a promising technology in fabricating high quality SiC structures.

Acknowledgement

This material is based in part upon work supported by the National Science Foundation under Grant Number CMMI-0619115. Any opinions, findings, and conclusions or recommendations expressed in this material are those of the authors and do not necessarily reflect the views of the National Science Foundation.

References

- [1] M. Östling, S. M. Koo, C. M. Zetterling, S. Khartsev, A. Grishin: *Thin Solid Films* **469-470**, (2004) p 444.
- [2] Y. Dong, C. Zorman, P. Molian: *J. Micromech. Microeng.* **13**, (2003) p 680.
- [3] D. J. Young, D. Jiangang, C. Zorman, W. H. Ko: *Sensors Journal, IEEE* **4**, (2004) p 464.
- [4] N. W. Jepps, T. Page: *Progress in Crystal Growth and Characterization*, ed. by P. Krishna (Pergamon Press, Oxford, 1983).

- [5] D. Méndez, A. Aouni, D. Araújo, E. Bustarret, G. Ferro, Y. Monteil: *Mat. Sci. For.* **483-485**, (2005) p 555.
- [6] J. Zhang, K. Sugioka, S. Wada, H. Tashiro, K. Toyoda, K. Midorikawa: *Appl. Surf. Sci.* **127-129**, (1998) p 793.
- [7] M. Mehregany, C. Zorman: *Thin Solid Films* **355-356**, (1999) p 518.
- [8] S. J. Pearton, C.R. Abernathy, B.P. Gila, F. Ren, J.M. Zavada, Y.M. Park : *Solid-State Electronics* **48**, (2004) p 827.
- [9] C. Palma, C. Sapia: *Journal of Electronic Materials* **29**, (2000) p 607.
- [10] S. Kim, B.S. Bang, F. Ren, J. D'Etremont, W. Blumenfeld, T. Cordock, S.J. Pearson : *Journal of Electronic Materials* **33**, (2004) p 477.
- [11] M. Schlaf, D. Sands, P.H. Key: *Appl. Surf. Sci.* **154-155**, (2000) p 83.
- [12] K. Zekentes, I. Zergioti, A. Klini, G. Constantindis: *Mat. Sci. For.* **527-529**, (2006) p 1119.
- [13] A. Battula, S. Theppakuttai, S. Chen: *J. Microlith. Microfab. Microsys.* **5**, (2006) 011009-1.
- [14] J. Zhang , K. Sugioka, S.Wada, H. Tashiro, K. Toyoda: *Appl. Phys. A* **64**, (1997) p 367.
- [15] N. Itoh: *Nucl. Instr. Meth. B* **122**, (1997) p 405.
- [16] W. R. L. Lambrecht, B. Segall, W. Suttrop, M. Yoganathan, R.P. Devaty, W.J. Choyke, J.A. Edmond, J.A. Powell, M. Alouani: *Appl. Phys. Lett.* **63**, (1993) p 2747.
- [17] S. Logothetidis, J. Petalas: *J. Appl. Phys.* **80**, (1996) p 1768.
- [18] S. G. Sridhara, R. P. Devaty, W. J. Choyke: *J. Appl. Phys* **84**, (1998) p 2963.

- [19] T. V. Blank, Y. A. Goldberg, E. V. Kalinina, O. V. Konstantinov, A. O. Konstantinov, A. Hallén: *Semicond. Sci. Technol.* **20**, (2005) p 710.
- [20] H. R. Philipp, E. A. Taft: *Silicon Carbide - A High Temperature Semiconductor*, ed. by J. R. O'Connor, J. Smiltens (Pergamon Press, Oxford, London, New York, Paris 1960).
- [21] *Properties of Advanced Semiconductor Materials*, ed. by M.E. Levinshtein, S.L. Rumyantsev, M.S. Shur (John Wiley and Sons, New York 2001).
- [22] *Process Technology for Silicon Carbide*, ed. by C.-M. Zetterling (INSPEC, London 2002).
- [23] O. Nilsson, H. Mehling, R. Horn, J. Fricke, R. Hofmann, S.G. Muller, R. Eckstein, D. Hofmann: *High Temperatures-High Pressures* **29**, (1997) p 73.
- [24] J. -P. Desbiens, P. Masson: *Sensors and Actuators A* **136**, (2007) p 554.
- [25] A. A. Tseng, Y.-T. Chen, K. -J. Ma: *Opt. Lasers Eng.* **41**, (2004) p 827.
- [26] R. Reitano, P. Baeri, *Nuclear Instruments and Methods in Physics Research B* **116**, (1996) p 369.
- [27] D. von der Linde, K. Sokolowski-Tinten, J. Bialkowski: *Appl. Surf. Sci.* **109-110**, (1997) p 1-10.
- [28] *Micromachining of Engineering Materials*: ed. by J. McGeough, Marcel Dekker, Inc. (New York, Basel) (2002) pp. 219- 221.
- [29] N. P. Furzikov, *Appl. Phys. Lett.* **56**, (1990) p 1638.
- [30] H. S. Carslaw, J. C. Jaeger: *Conduction of Heat in Solids*, 2nd ed. (Clarendon, Oxford 1959).

- [31] M.F. Von Allmen and S.S. Lau: Laser Annealing of Semiconductors, ed. by J.M. Poate and J.W. Mayer (Academic Press, New York 1982).
- [32] J. F. Ready: Effects of High-Power Laser Radiation (Academic Press, New York 1971).
- [33] N. Ozisik: Heat Conduction (Wiley, New York 1993).
- [34] J. H. Yoo, S. H. Jeong, R. Greif, R.E. Russo: J. Appl. Phys. **88**, (2000) p 1638.
- [35] J. J. Kim, D. J. Katz: United States Patent **4649002**, Kennecott Corporation, Ohio (1987).
- [36] Y. Song, F. W. Smith: Appl. Phys. Lett. **81**, (2002) p 3061.
- [37] Z. Duanming, L. Dan, L. Zhihua, G. Li, T. Xinyu, L. Li, F. Ranran, H. Dezhi, L. Gaobin: Appl. Surf. Sci. **253**, (2007) p 6144.
- [38] L. Dan, Z. Duanming: Chin. Phys. Lett. **25**, (2008) p 1368.
- [39] T. Gorelik, S. Urban, F. Falk, U. Kaiser, U. Glatzel: Chem. Phys. Lett. **373**, (2003) p 642.
- [40] A. I. Savvatimskiy: Carbon **43**, (2005) p 1115.
- [41] D. Bauerle: Laser Processing and Chemistry (Springer-Verlag, Berlin New York 2000).
- [42] S. Amoruso: Appl. Phys. A **69**, (1999) p 314.
- [43] F. Neri, F. Barreca, S. Trusso: Diamond and Related Materials **11**, (2002) p 273.
- [44] J. H. Yoo, S. H. Jeong., X. L. Mao, R. Greif, R. E. Russo: Appl. Phys. Lett. **76**, (2000) p 783.
- [45] V. Craciun, N. Bassim, R. K. Singh, D. Craciun, J. Hermann, C. Boulmer-Leborgne: Appl. Surf. Sci. **186**, (2002) p 288.
- [46] M. M. Martynyuk: Sov. Phys. Tech. Phys. **19**, (1974) p 793.

- [47] M. M. Martynyuk: Sov. Phys. Tech. Phys. **21**, (1976) p 430.
- [48] K.H. Song, X. Xu: Appl. Surf. Sci. **127-129**, (1998) p 111.
- [49] H. R. Shanks, P. D. Maycock, P. H. Sidles, G. C. Danielson: Phys. Rev. **130**, (1963) p 1743.
- [50] C. J. Glassbrenner, G. A. Slack: Phys. Rev. **134**, (1964) A 1058.
- [51] W. H.-Xing, X. Chen: Journal of Physics. D, Appl. Phys. **36**, (2003) p 2230.
- [52] R. C. Reid: Am. Sci. **64**, (1976) p 146.
- [53] V. P. Carey: Liquid-Vapor Phase Phenomena (Hemisphere, Washington 1992).
- [54] A. Miotello, R. Kelly: Appl. Phys. A **69**, (1999) S67.
- [55] R. Kelly, A. Miotello: Appl. Surf. Sci. **96-98**, (1996) p 205.
- [56] Q. Lu, S. S. Mao, X. Mao, R. E. Russo: Appl. Phys. Lett. **80**, (2002) p 3072.
- [57] R. E. Russo, X. L. Mao, H. C. Liu, J. H. Yoo, S. S. Mao: Appl. Phys. A **69 [Suppl.]**, (1999) S887.
- [58] A. Bogaerts, Z. Y. Chen, R. Gizbels, A. Vertes: Spectrochim. Acta B **58**, (2003) p 1867.
- [59] Z. Y. Chen, A. Bogaerts: J. Appl. Phys. **97**, (2005) 063305.
- [60] J. G. Lunney, R. Jordan: Appl. Surf. Sci. **941**, (1998) p 127.
- [61] M. U. Islam, G. McGregor, G. Campbell: United States Patent **5138130**, National Research Council of Canada, California (1992).
- [62] J. C. Koo, R. E. Slusher: Appl. Phys. Lett. **28**, (1976) p 614.
- [63] J. E. Sipe, J. F. Young, J. S. Preston, H. M. Van Driel: Phys. Rev. B **27**, (1983) p 1155.
- [64] D. J. McCulloch, S. D. Brotherton: Appl. Phys. Lett. **66**, (1995) p 2060.
- [65] Y. Dong, P. Molian: Appl. Phys. Lett. **84**, (2004) p 10.

- [66] X. J. Wu, T. Q. Jia, F. L. Zhao, M. Huang, N. S. Xu, H. Kuroda, Z. Z. Xu: Appl. Phys. A **86**, (2007) p 491.
- [67] T. J. Bastow: Nature **222**, (1969) p 1058.
- [68] Surface studies with Laser, ed. by F. R. Aussenegg, A. Leitner, M. E. Lippitsch (Springer Series in Chemical Physics, Berlin-Springler 1983).
- [69] S. J. Thomas, R. F. Harrison, J. F. Figueira: Appl. Phys. Lett. **40**, (1982) p 200.
- [70] R. G. Caro, M. C. Gower: J. Quant. Elect. **QE-18**, (1982) p 1380.
- [71] I. Ursu, I. N. MihBilescu, A. L. Popa, A. M. Prokhorov, V. P. Ageev, A. A. Gorbunov, V. I. Konov: J. Appl. Phys. **58**, (1985) p 3909.
- [72] J. J. Yu, Y. F. Lu: Appl. Surf. Sci. **154-155**, (2000) p 670.
- [73] G. K. Giust, T. W. Simpson: Appl. Phys. Lett. **70**, (1997) p 26.

CHAPTER 4 PICOSECOND PULSED LASER ABLATION AND MICROMACHINING OF 4H-SiC WAFERS

A paper submitted to *Applied Surface Science*

Saurabh Gupta, Ben Pecholt and Pal Molian

Abstract

Ultra-short pulsed laser ablation and micromachining of n-type, 4H-SiC wafer was performed using a 1552 nm wavelength, 2 picosecond pulse and 5 μJ pulse energy erbium-doped fiber laser with an objective of rapid etching of diaphragms for pressure sensors. Ablation rate, studied as a function of energy fluence, reached a maximum of 20 nm per pulse at 10 mJ/cm^2 , which is much higher than achievable by the femtosecond laser. Ablation threshold of 2 mJ/cm^2 agrees well with the prediction of Coulomb explosion (CE) model of material removal. Scanning electron microscope images supported the CE mechanism by revealing very fine particulates, smooth surfaces and absence of thermal effects including melt layer formation. It is hypothesized that defect-activated absorption and multiphoton absorption mechanisms gave rise to a charge density in the surface layers required for CE and enabled material expulsion in the form of nanoparticles. Trenches and holes micromachined by the picosecond laser exhibited clean and smooth edges and non-thermal ablation mode for pulse repetition rates less than 250 kHz. However carbonaceous material and recast layer were noted in the machined region when the pulse repetition rate was increased 500 kHz. A comparison with femtosecond pulsed lasers show the promise that picosecond lasers are more efficient and cost effective for creating sensor diaphragms and via holes in 4H-SiC.

1. Introduction

Ultra-short pulsed (USP) lasers are emerging as micromachining tools for difficult-to-etch materials. USP lasers are those that have pulse durations less than few picoseconds causing greater absorption depth than heat diffusion length in most materials and limiting the transfer of electron energy to the lattice. Consequently there are reduced thermal effects leading to high spatial resolution, absence of contamination, negligible heat-affected zone and formation of nanoscale features [1]. The capability of USP lasers to precisely carve out the material forming holes with diameters less than 10 μm was demonstrated in a comparative study of ablation by nanosecond and USP lasers [2]. Unlike nanosecond pulsed lasers, USP lasers give rise to multiphoton absorption resulting very small absorption volume, improved energy coupling, reduced threshold energy fluence and transition from stochastic to deterministic ablation.

Silicon carbide (SiC) is an excellent semiconductor for devices that operate under extreme conditions such as high-temperature and harsh chemical environments. Among over 250 crystalline polytypes of SiC, 4H-SiC is the most preferred type due to its availability in various wafer sizes and defect-less single-crystal growth. 4H-SiC is also well known for its attractive properties such as wide bandgap, chemical inertness, high thermal conductivity, high field breakdown strength and high carrier saturation velocity [3]. While 4H-SiC has already proven its value for high power and high frequency devices, it has also superior characteristics required for MEMS-NEMS, biomedical sensors, optics, UV detectors and thermal dissipation systems.

The chemical stability of 4H-SiC makes it difficult to perform microfabrication processes such as etching, oxidation and ion implantation. Reactive ion etching, photoelectrochemical etching, inductively coupled plasma and electron cyclotron resonance methods are used to etch 4H-SiC but at very low rates [3-5]. For example, a maximum etch rate of 0.97 $\mu\text{m}/\text{min}$ was achieved in an inductively coupled reactor using SF_6 -based gas mixtures. Furthermore the etch selectivity of SiC to Si and SiO_2 is poor. Microfabrication of MEMS devices or *via* holes for high-frequency electronic devices require deep etching (up to 400 μm) and, consequently, high etch rate processes are desired. Deep reactive ion etching (DRIE) is one such process that produced good uniformity, smooth surfaces and high etch rates (1.35 $\mu\text{m}/\text{min}$) and enabled the etch selectivity ratio to be about 50 with the aid of a nickel mask under high etch rate conditions [6]. DRIE also produced *via* holes to a depth of 330 μm in 4H-SiC substrates [6].

Femtosecond pulsed laser micromachining of various polytypes of bulk and thin film SiC was investigated to improve the etch rate as well as feature quality in applications like micromotors, resonators, microgrippers etc. [7-11]. However, the demands of industrial manufacturing for fast, precise micromachining are better met by the robust, reliable, high repetition rate and high power picosecond lasers. For example, Mound Laser uses 8 W, 10 ps laser to micromachine SiC wafers as large as 300 mm x 300 mm and with features as small as a few microns [12]. In this paper, we report the effects of picosecond laser on the ablation and micromachining of 4H-SiC useful to make pressure sensor diaphragms and cantilevers for MEMS devices.

2. Experimental Details

Single crystalline wafers of the type 4H-SiC (n-type semiconductor, silicon face polished/epi ready) with 50 mm diameter and 250 μm thick were procured from Cree, Inc (NC, USA). The wafer has less usable surface area (>50%) than Cree's standard research grade (>70%). A 1552-nm wavelength erbium-doped fiber laser (USP laser, Raydiance, CA) was employed for micromachining. Figure 1 shows a photograph of table-top USP laser system while Table 1 lists its specifications. The beam was directed to the sample surface through a Mitutoyo microscope objective (20X, 0.4 NA) for a spot size 250 μm .



Table 1. Specifications of USP laser used in this work

Pulse energy	Pulse width	Repetition rate	Average power	Beam size	Beam profile
5 μJ	2 ps	500 kHz max	2.5 W	5 mm	TEM ₀₀

Figure 1: Photograph of USP laser (Raydiance Inc., CA, USA)

Two types of experiments were conducted: *1) Ablation*: In the first set of experiments, the beam was focused on the wafer surface using a pulse energy 5 μJ for a spot diameter of 250 μm and then scanned at a speed of 24 mm/sec for various pulse repetition rates of 500, 250, 125, 31, 7.8, 2, 0.5 kHz in ambient environment. In the second set of experiments, the energy fluence was varied by defocusing the beam every 10 μm from the focal point and then used to machine five lines at a scan rate of 24 mm/sec and pulse frequency of 125 kHz (Figure 2). The spot sizes for defocused beams were calculated based on Gaussian beam propagation equation:

$$w(z) = w_0 [1 + (z/z_R)^2]^{1/2} \quad (1)$$

where $w(z)$ is the spot radius, w_0 is the focused beam spot radius, z is the distance from the focal point and z_R is the Rayleigh range given by $z_R = \pi w_0^2/\lambda$.

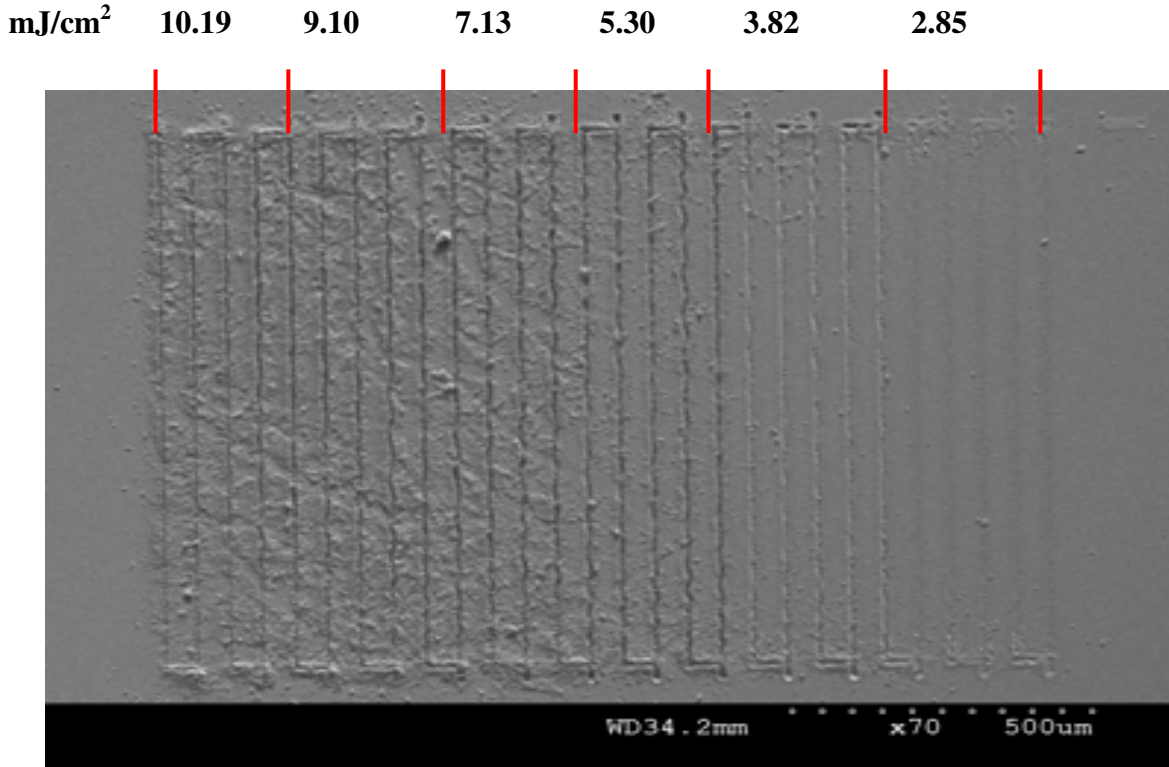


Figure 2: Picosecond laser ablated lines with varying energy fluence

The spot diameters were calculated as 250, 262, 296, 344, 404 and 468 μm . The corresponding energy fluences were 10.19, 9.10, 7.13, 5.30, 3.82 and 2.85 mJ/cm^2 . The ablation rate was then calculated by measuring the depth and dividing it by the number of pulses that occurred in the spot size for each energy fluence; 2) *Micromachining experiments:* Trenches and holes are produced using pulse energy of 2.5 μJ , repetition rate 50 kHz and scan rate 24 mm/sec which are found as the optimum parameters established from the ablation tests. Trenching was done with small Δz steps. Nitrogen was used as an assist gas to

purge across the ablated region to remove the debris. The samples were then ultrasonically cleaned. Following laser micromachining, the samples were examined in scanning electron microscope. An optical profilometer was used to measure the ablation depths.

3. Results and Discussion

3.1 Ablation

Figure 3 is a plot of ablation rate *versus* energy fluence based on multi-pulse ablation experiments. The ablation rate increases exponentially with energy fluence followed by saturation. Femtosecond pulsed (1026 nm, 400 fs) laser ablation of single crystalline 3C-SiC wafer exhibits similar behavior but the ablation rates are much lower [11] than those shown in Figure 3 for the same energy fluence.

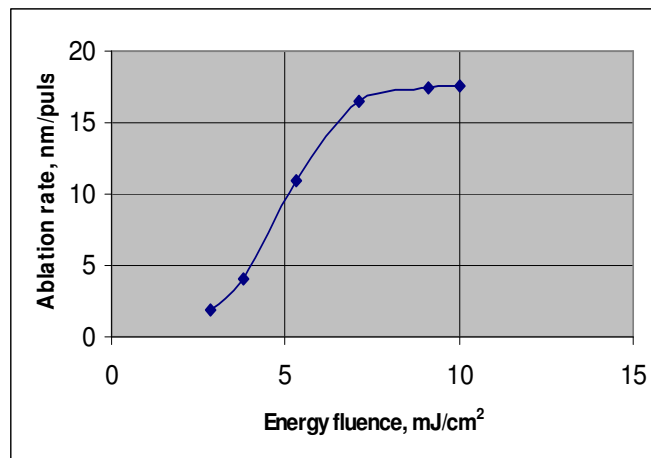


Figure 3: Ablation rate versus fluence for 4H- SiC

In the present study, the ablation threshold was determined as 2 mJ/cm². Zoppel et al observed a higher ablation threshold of 60 mJ/cm² for 3C-SiC with 1026 nm, 400 fs-laser [11]. The difference is partly attributed to the pulse duration effects on electron heating. Figure 4 shows a 500 μm wide channel produced in 4H-SiC (5 μJ/pulse) where the

accumulation of debris on the ablated area hinders the ablation process. There is no major difference in the ablation features between 500, 250, and 125 kHz except some minor thermal damage at repetition rates exceeding 250 kHz. USP lasers differ fundamentally from nanosecond pulsed lasers in the ablation process. While the nanosecond pulsed laser involves linear excitation to generate substantial heat for ablation, the USP laser ablates the material *via* a non-linear, multiphoton ionization mechanism.

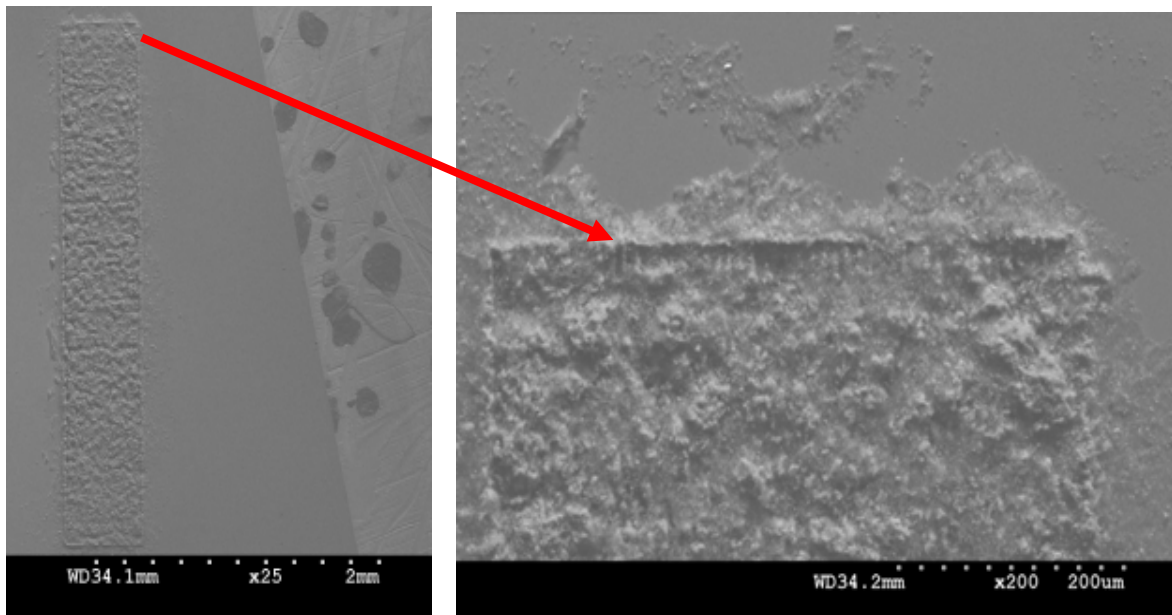


Figure 4: Laser ablated region (5 $\mu\text{J}/\text{pulse}$, 125 kHz, 24 mm/sec, defocused beam size 500 μm)

The linear absorption coefficient of 4H-SiC corresponding to 1552 nm (0.8 eV) light is low on the order of 50 cm^{-1} [13, 14]. The ablation depth may be calculated from the following linear absorption equation:

$$Z = \alpha^{-1} \ln (F/F_{\text{th}}) \quad (2)$$

where α = absorption coefficient, F is energy fluence and F_{th} is threshold. Application of equation (2) yields much lower ablation rates than obtained in the experiments (for example 0.002 nm per pulse as opposed to 10 nm per pulse at 5 mJ/cm^2), suggesting that multiphoton and defect/impurity-activated absorptions are the major contributors to the ablation rate. Alternatively thermal diffusion might play some role. However thermal diffusion distance, calculated from $(4\kappa t)^{1/2}$ where $\kappa = 1.7 \text{ cm}^2 \text{ s}^{-1}$ [15] for 4H-SiC and $t = 2 \text{ (} 10^{-12} \text{) s}$, is $13.6 \text{ (} 10^{-6} \text{) cm}$ which is substantially lower than optical absorption depth ($2 \times 10^{-2} \text{ cm}$), inferring that thermal diffusion effects are indeed negligible.

Laser ablation can be conveniently divided into two types [16]. One is “strong ablation” that involves large amount of material removal through thermal vaporization and is most common with nanosecond laser pulses for energy fluences above threshold. Two is a non-thermal “gentle ablation” associated with ultra-short laser pulses that has the ability to precisely control the material removal in nanoscale through Coulomb explosion (CE) mechanism. Gentle ablation usually occurs at or near threshold and results in excellent surface quality with no evidence of melt zone [17, 18]. In CE mechanism, the USP laser pulse rapidly evacuates the electrons from the surface region leading to the formation of positively charged ions in the near-surface layers that in turn electrostatically repel each other causing ejection of material [19, 20]. Typical requirements for CE are pulsed laser beam with pulse width in the range of 10 picoseconds to 10 femtoseconds and laser intensity in the range of 10^{10} W/cm^2 to 10^{13} W/cm^2 [16].

CE has been demonstrated in USP laser ablation of dielectrics such as aluminum oxide and semiconductors like Si [17, 18]. The criterion for CE to occur is that the

electrostatic force due to the surface charge density must exceed the bonding force [19]. Based on a number of calculations, it is found that the typical surface charge density must be greater than $10^{22}/\text{cm}^3$; this is achievable in dielectric materials irradiated by a typical UPS laser because of multiphoton absorption mechanism that triggers avalanche photoionization [17]. However, such a high charge density is argued not to be reachable in semiconductors due to charge reneutralization phenomenon [19]. Hence a strong linear absorption becomes necessary for CE to occur in semiconductors without the requirement of avalanche photoionization [16]. The laser wavelength selected for ablation must correspond to one of the peaks in the semiconductor's linear optical absorption spectrum in order to maximize the electron generation. The carrier density, N_e , is given by the following expression [16]:

$$dN_e/dt = [\alpha + \alpha_D(N_e)] I \quad (3)$$

where α is the linear absorption coefficient, $\alpha_D(N_e)$ is the Drude carrier absorption and I is the laser intensity. The application of the above expression in the present study [α is 50 cm^{-1} , α_D is taken as negligible, $I = 5 \text{ GW}/\text{cm}^2$, $t = 2 \text{ ps}$, $\lambda = 1552 \text{ nm}$ (0.8 eV)] yields a carrier density of $10^{10}/\text{cm}^3$ attesting that there is no possibility for CE to occur. However one must note that optical absorption spectra in semiconductors are normally dominated by transitions from the valence to the conduction bands [14]. Strong defect-related absorption bands are quite possible. In other words, the optical absorption near the band edge was a function of the specific 4H-SiC [13]. For example, well-defined absorption ‘‘bands’’ were observed below 1eV due to the defect structure in n-type doped 4H-SiC with carrier concentrations in the range 10^{17} to 10^{19} per cm^3 [14]. In addition, these samples showed a Drude-like absorption at low energies (<1 eV). Hence, despite our calculations of carrier density not exceeding the

threshold density by several orders of magnitude, the phenomenon of CE cannot be ruled out because the effects of defect- activated absorption and multiphoton absorption mechanisms are not known.

Based on scanning electron microscope observations of ablated regions such as presence of very fine debris including nanoparticles and absence of thermal damage, we believe that the material removal mechanism is CE. In addition, the fundamental energy calculations shown below for ablation threshold validate our hypothesis that CE is the most likely mechanism of material removal.

Threshold fluence for the energetic electrons to escape the solid and produce a strong charge separation field necessary for CE of the surface layers [20] is determined by the electron energy T_e reaching the sum of the atomic binding energy and the ionization energy of the material. Solution to the electron temperature equation yields the following expression [16]:

$$(1 - R) I_{th} \tau_p \approx 3/8 \times N_{at} / \alpha \times (E_b + I_p) \quad (4)$$

For 4H-SiC ($N_{at} = 10^{19}$ atoms/cm³) at 1552 nm, the reflectivity is roughly 20%. The binding energy is $E_b \approx 0.02$ eV/atom, and the ionization potential is $I_p \approx 0.124$ eV [21]. The threshold fluence is then estimated using equation (4) as $I_{th} \tau_p \approx 2.16$ mJ/cm². This estimate agrees well with our experimental finding of threshold (2 mJ/cm²).

3.2 Micromachining

Figure 5 shows a few holes in 4H-SiC produced in the non-thermal ablation regime of USP laser micromachining. The holes are conical with about 10 μ m in diameter. The key problem is the debris accumulating in the holes. A gas jet with high flow rate must be used to prevent

the debris from interfering with the laser beam. Similar to the present study, an array of *via* holes exhibiting smooth side walls and no thermal effect was drilled in 3C–SiC using a 300 fs, 1040 nm wavelength laser [11]. The drilling speeds in both studies were many times (10 to 100) faster than that of RIE.

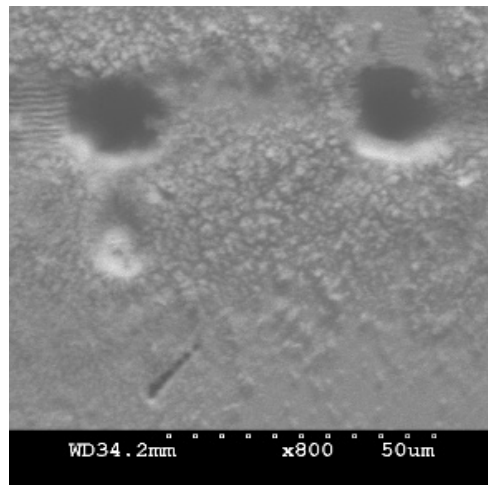


Figure 5: USP laser drilled holes in 4H-SiC

Figure 6 shows a 2 mm by 0.2 mm trench produced at 2.5 $\mu\text{J}/\text{pulse}$ and 50 kHz using a defocused beam pattern. The depth is approximately 26 μm for a total of five laser passes; each pass removed approximately 5 μm . Greater depths can be easily obtained with more passes. The sidewalls are smooth and the edges appear to be quite sharp. However, the debris accumulates at both ends of the trench (Figure 7a) that could not be removed with the purge gas. The bottom of the trench appears to be quite smooth (Figure 7b) with no evidence of melt formation, micro-cracks or other thermal damages. By comparison, nanosecond pulsed excimer laser micromachining of 3C-SiC resulted in a bottom area is undulated or corrugated [11].

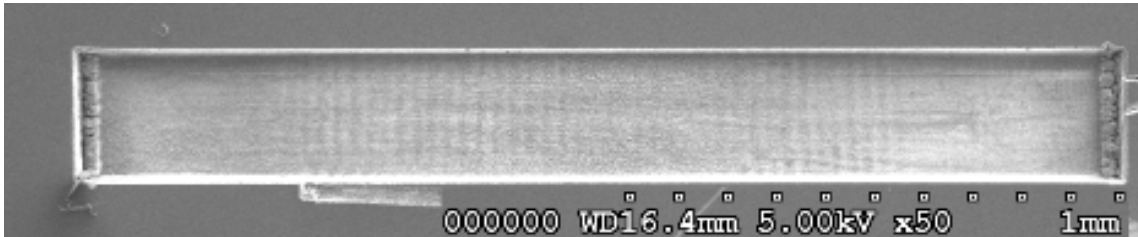


Figure 6: 4H-SiC ablated at 50 kHz, with N₂ flow placed 2 mm from ablation zone

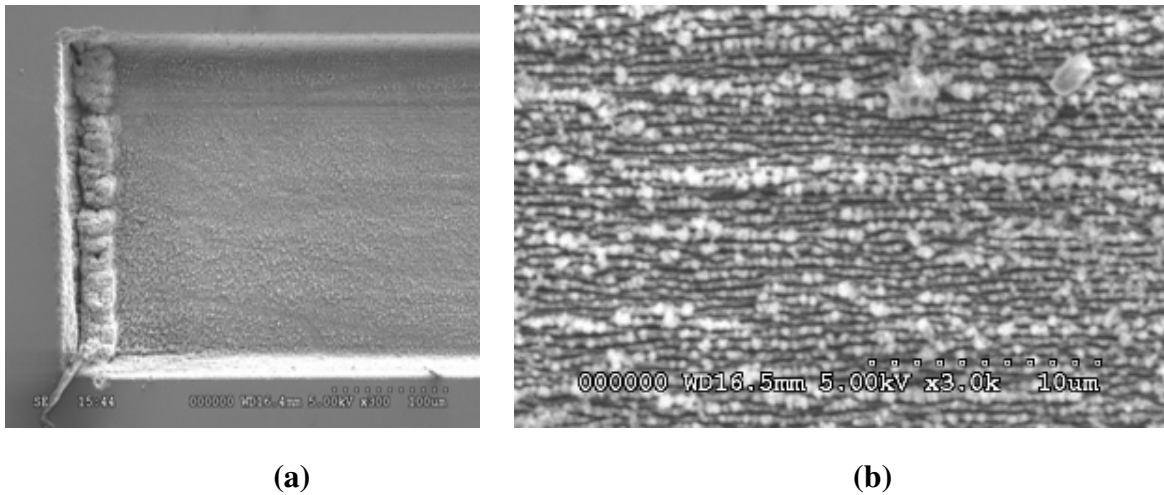


Figure 7: (a) Magnified view of one end of Figure 6; (b) Bottom of SiC trench appearing smooth

An interesting observation was thermal effect in micromachining when the repetition rate was made above 250 kHz. If the machining was performed with a focus above the material surface at 500 kHz, a black compound (Figure 8) has appeared in the ablation zone; this is identified as carbonaceous material formed due to thermal decomposition of SiC. Furthermore when the focal area of the beam was moved closer to the surface, thermal effect is more pronounced by replacing the black compound with a white, snow-like material that is believed to be the recast layer of SiC; this layer could not be expelled by the use of assist gas.

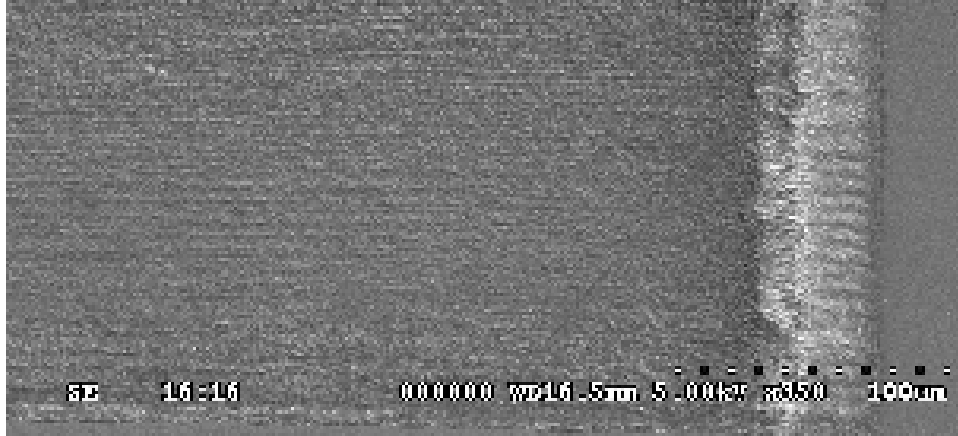


Figure 8: Formation of decomposed carbon products when the beam was focused above the surface at 500 kHz

4. Conclusions

A 5 μJ , 2 ps pulsed laser was used to ablate and micromachine 4H-SiC wafer in non-thermal mode. Ablation depth per pulse was in the range of 1-18 nm depending on the energy fluence and ablation threshold was 2 mJ/cm^2 . Thermal effects were not observed until the repetition rate exceeded 250 kHz. Trenches of 26 μm deep and holes of 10 μm diameter were machined with very clean edges and smooth bottom surface. Recast layer and carbonaceous material began to appear in the micromachined regions when the pulse repetition rate exceeded 250 kHz. Coulomb explosion mechanism is believed to account for the material removal where defect-activated and multiphoton absorption mechanisms of picosecond-SiC interactions generated the Coulomb explosion threshold charge densities. Picosecond pulsed laser ablation is thus more effective than femtosecond pulsed laser in terms of ablation rate and nanosecond pulsed laser in terms of cleanliness and thermal effects.

Acknowledgement

This material is based in part upon work supported by the National Science Foundation under Grant Number CMMI-0619115. Any opinions, findings, and conclusions or recommendations expressed in this material are those of the authors and do not necessarily reflect the views of the National Science Foundation.

References

1. M.D. Shirk and P. A. Molian. "A Review of ultrashort pulsed laser ablation of materials," Journal of Laser Applications, 10, 1, (1998), 18-28.
2. J. Jandeleit, A. Horn, R. Weichenhain, E.W. Kreutz, R. Poprawe, Applied Surface Science 127–129, (1998), 885–891.
3. Silicon Carbide, A Review of Fundamental Questions and Applications to Current Device Technology, edited by W. J. Choyke, H. Matsunami, and G. Pens, Academic Press, New York, 1997.
4. P. Leerungnawat, D. C. Hays, H. Cho, S. J. Pearton, R. M. Strong, C.-M. Zetterling, and M. O' stling, J. Vac. Sci. Technol. B 17, (1999), 2050.
5. F. A. Khan and I. Adesida, Appl. Phys. Lett. 75, (1999), 2268.
6. P. Chabert, N. Proust, J. Perrin, and R. W. Boswell, Appl. Phys. Lett. 76, (2000), 2310.
7. Y. Dong and P. Molian, "Femtosecond pulsed micromachining of single crystalline 3C-SiC structures based on a laser-induced defect-activation process," Journal of Micromechanics and Microengineering, 13, (2003), 680-685.

8. Y. Dong and P. Molian, "Femtosecond pulsed laser ablation of 3C-SiC thin film on silicon" Applied Physics A 77, (2003) 839-836.
9. Y. Dong, P. Molian, C. Zorman and M. Mehregany, 2002. "High-energy femtosecond pulsed laser micromachining of thin film deposited Si in self-focused air medium," Journal of Laser Applications, 14, 4, (2002), 221-230.
10. Y. Dong, R. Nair, R. Molian and P. Molian, "Femtosecond-pulsed laser micromachining of a 4H-SiC wafer for MEMS pressure sensor diaphragms and via holes," Journal of Micromechanics and Microengineering, 18, 3, (2008), 035022.
11. S. Zoppel, M. Farsari, R. Merz, J. Zehetner, G. Stangl, G. A. Reider and C. Fotakis, "Laser micromachining of 3C-SiC single crystals," Microelectronic Engineering, 83, 4-9, 2006, 1400-1402.
12. <http://www.mdatechnology.net/update.aspx?id=a5188>, "An attempt to micromachine SiC wafers using picosecond laser at Mound Laser& Photonics Center (Miamisburg, Ohio)", Accessed: June 2008.
13. M. Manasreh, K. Miller, Q. Zhou, Z. Feng, J. Chen and I. T. Ferguson, "Optical absorption of doped and undoped bulk SiC," Silicon Carbide--Materials, Processing and Devices, MRS Proceedings Volume 640, H5.23.
14. S. Limpijumnong, W. L. Lambrecht, S. N. Rashkeev, and B. Segall, Physical Review, 59, 20, (1999), 12890.

15. Goldberg Yu., Levinshtein M.E., and Romyantsev S.L. in Properties of Advanced Semiconductor Materials GaN, AlN, SiC, BN, SiC, SiGe . Eds. Levinshtein M.E., Romyantsev S.L., Shur M.S., John Wiley & Sons, Inc., New York, 2001, 93-148.
16. W. Chism, "Method of direct coulomb explosion in laser ablation of semiconductor structures," US Patent 20070293057, 12/20/2007.
17. W. G. Roeterdink et al., "Coulomb explosion in femtosecond laser ablation of Si(111)," Appl. Phys. Lett. 82, (2003) 4190.
18. R. Stoian et al., "Coulomb explosion in ultrashort pulsed laser ablation of Al₂O₃," Phys. Rev. B, 62, (2000), 13167-13173.
19. N. M. Bulgakova et al., "Model description of surface charging during ultra-fast pulsed laser ablation of materials," Appl. Phys. A 79, (2004), 1153-1155.
20. E. G. Gamaly et al., "Ablation of solids by femtosecond lasers: ablation mechanism and ablation thresholds for metals and dielectrics," Phys. of Plasma, 9, (2002), 949-957.
21. Properties of SiC, Edited by G.L. Harris, 1995, published by IET, ISBN:0852968701.

CHAPTER 5 FINITE ELEMENT ANALYSIS OF SINGLE CRYSTAL 6H-SiC DIAPHRAGM FOR HIGH-TEMPERATURE MEMS PRESSURE SENSORS

Nomenclature

a	length of the plate (m)	α	coefficient of linear thermal expansion (/K)
b	width of the plate (m)	P	applied pressure (N/m ²)
t	thickness of the plate (m)	σ	principal stress (N/m ²)
w	deflection of plate (m)	ε	principal strain
E	Young's Modulus (N/m ²)	τ	shear stress (N/m ²)
G	shear Modulus (N/m ²)	γ	shear strain
ν	Poisson's ratio	σ_{VM}	Von Mises stress (N/m ²)
ρ	mass density (kg/m ³)	σ_Y	yield stress (N/m ²)

1. Introduction

Micro-Electro-Mechanical-System (MEMS) sensors have grown into a multi-billion dollar industry due to their small size, excellent performance, low cost and high volume production. Silicon-based MEMS pressure sensors currently serve large markets for pressure sensing in moderate temperature applications, with the most advanced devices operating up to about 600 K [1]. There is an emerging and growing demand for MEMS pressure sensors to function accurately and reliably at temperatures higher than 700 K in mechanically and chemically harsh environments such as in many energy conversion and emission control applications [2]. For example, MEMS sensors are highly sought after for measuring engine exhaust streams in corrosive, high-temperature environments (>850 K) or monitoring extreme pressures (both high and low) in industrial applications. Specifically, Siemens Westinghouse Power Generation is seeking technologies that produce sensors for use at 1000 K that should have

the potential of being commercially deployed in electric power generation systems in the 1 MW to 1500 MW power output range prior to 2015. In the automotive industry, requirements for improved fuel efficiency and reduced emissions over the next 5 – 10 years create numerous opportunities for such devices. Similarly, energy needs are making additional opportunities for pressure sensors that can operate at higher temperatures and in chemically reactive environments. Some examples are fuel cells (particularly reformers), coal-based power generation plants, and down-hole drilling operations.

Silicon Carbide (SiC)-based MEMS pressure sensors can fulfill the requirements of working in hostile and harsh environments such as high temperature, high pressure, high vibration, high noise, or corrosive chemicals due to SiC's exceptional mechanical, electrical, chemical and thermal properties [3-4]. SiC also exhibits excellent piezoresistive effect and is compatible with CMOS process (allowing for integration with CMOS circuits). In fact, 6H-SiC piezoresistive pressure sensors have already been fabricated by using a combination of DRIE (Deep Reactive Ion Etching) and electrochemical etching methods and are capable of operating at 650 K and pressures ranging from 0.175 MPa to 7 MPa [5-6]. Despite such benefits, etching of SiC and fabrication of high-temperature contact and pad materials remains to be tedious and time-consuming.

Figure 1 shows a cross-sectional view of a potential pressure sensor consisting of: a) a MEMS diaphragm integrated with SiC-piezoresistor; b) electronics chip; and c) AlN packaging. It is based on the piezoresistive effect which describes the change in electrical resistance of the material due to applied mechanical stress. Therefore, it is vital to calculate the relationship between stress distribution in the elastic diaphragm and pressure applied as it

will control the output voltage. The performance of a sensor is greatly related to the diaphragm thickness [7]. It has been reported that thin diaphragms have greater impact on the maximum deflection than on the maximum bending stress [8]. The design of a sensor diaphragm also depends on the processing conditions. For example, at low operating pressure ($P < 30$ kPa) thin diaphragms are needed while at higher operating pressures ($P > 35$ MPa) the use of thicker diaphragms are recommended [8]. Additionally, rectangular diaphragms induces higher maximum bending stresses and lowest maximum deflections, compared to diaphragms with other geometries, which make them favorable from mechanical strength point of view. Table 1 list the effect of diaphragm geometry on maximum stress and deflection in a diaphragm of same thickness, area, and applied pressure [8].

Table 1: Effect of diaphragm geometry on maximum stress and deflection

Geometry of diaphragm	Maximum stress	Maximum deflection
Circular	Low	Highest
Rectangular ($a/b = 2$)	Higher	Low
Square	Highest	Higher

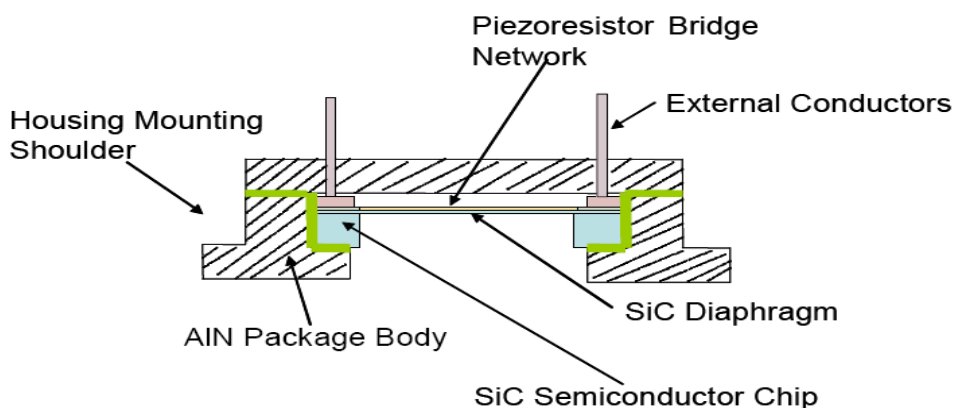


Figure 1: Cross-section of a planned pressure sensor

In this study, we report the finite element analysis (FEA) that establishes a correlation between deflection and pressure of 6H-SiC bulk micromachined diaphragms fabricated by a 248 nm pulsed excimer laser for the temperatures ranging from 300 – 1000 K. The purpose is to determine the stress and strain distributions, the most optimized areas for the placement of piezoresistors, and the areas for maximum displacement in a high temperature-pressure environment. The results will be used as an input for fabrication of prototype sensor.

2. Excimer Laser Micromachining

A single crystal 6H-SiC wafer (n-type semiconductor, nitrogen dopant density ranging from $\sim 10^{17}/\text{cm}^3$, silicon face polished/epi ready) with 50 mm diameter and 250 μm thick, procured from Cree Inc. (NC, USA) was used for micromachining. A 248 nm (23 ns) pulsed excimer laser was used to fabricate the sensor diaphragm measuring 4 mm x 1.5 mm x 0.05 mm. The energy fluence and repetition rate used was 7 Jcm^{-2} and 10 Hz respectively. A positioning table capable of moving in X and Y axes was used to attain the desired geometry. The experiments were carried out in an atmosphere where N_2 gas was directly flowing over the exposed surface so that it can mitigate the formation of SiO_2 caused by the oxidation of SiC surface. Figure 2 shows the SEM image of the micromachined diaphragm.

A critical issue in pressure sensors could be the edge quality or flatness of the diaphragm affecting its sensitivity. It has been reported that a three-dimensional function representing the flatness of diaphragm should be incorporated in the sensitivity

analysis [9]. Both the bottom and side walls of laser micromachined diaphragm have irregularities.

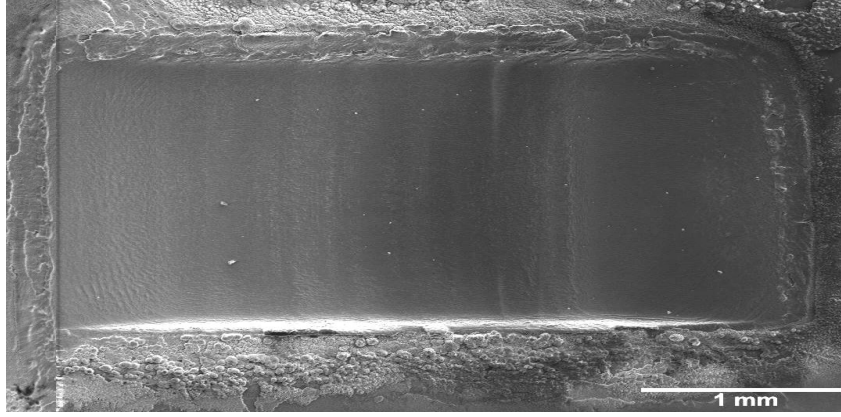


Figure 2: SEM image of 6H-SiC sensor diaphragm

Figure 3 shows the surface texture of the bottom region of the diaphragm. The non-uniformity of the bottom surface is attributed to the occurrence of non-resonant periodic structures associated with nanosecond laser micromachining [10, 11]. It has been reported that the surface undulations induce pressure changes through frictional effect [12, 13]. The pressure gradient is given by the expression [13]:

$$\frac{dP}{dx} \propto m^{\square} f D_f \quad (1)$$

where m^{\square} is the mass flow rate, f is the frictional factor, and D_f is the flow diameter.

A schematic representation of the diaphragm subjected to applied pressure is shown in Figure 4. Since the effective area (A) through which pressure is applied is relatively small, the mass flow rate can be assumed constant. Moreover, the periodicity of undulations in Figure 3 is of the order 5 – 10 μm , which can be neglected. Based on this assumption, a uniform pressure flow is considered in the analysis.

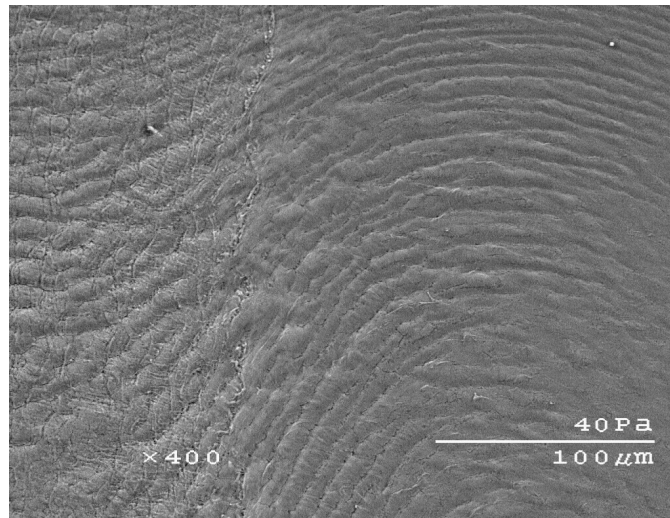


Figure 3: Bottom surface of micromachined 6H-SiC showing irregularities

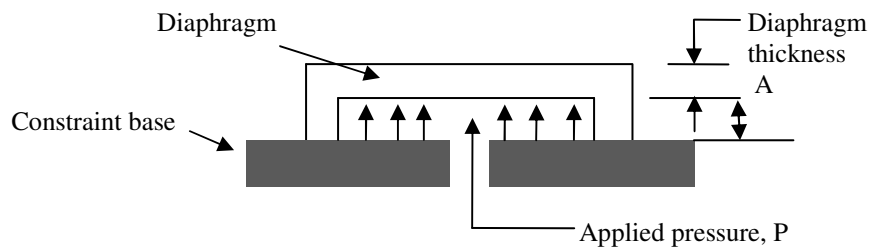


Figure 4: Schematic of a SiC die for a pressure sensor

3. Material Properties

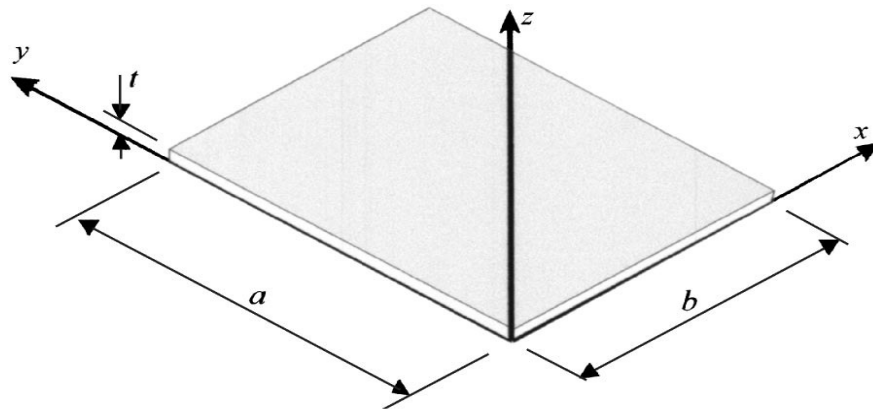
Table 2 lists the material properties of 6H-SiC considered in this study. The values are taken at 300 K and assumed to be constant with increase in temperature up to 1000 K. Additionally, material properties are assumed to be isotropic as it has been suggested that the variation of stress at any given location is within 3% when using 3-D anisotropic properties for FEM analysis [14].

Table 2: Material properties of single crystal 6H-SiC

Property	Value	Units	Reference
E	4.5×10^{11}	N/m ²	[15]
ν	0.18	–	[15]
G	1.9×10^{11}	N/m ²	[16]
ρ	3.2×10^3	kg/m ³	[17]
α	4.5×10^{-6}	/K	[17]
σ_Y	21×10^9	N/m ²	[18]

4. Mathematical Formulation of the Problem

The classical plate theory is traditionally used to explain the analysis of micromachined diaphragms. It has been reported that, however, small deflection theory is appropriate for deflections less than 1/5 of diaphragm thickness while for deflections up to three times the diaphragm thickness, large deflection theory should be used [19]. In our analysis, we assumed small deflection theory because of thicker diaphragm. Figure 5 shows the coordinate system and dimensions of the diaphragm considered as a rectangular plate which is held at four edges.

**Figure 4: Co-ordinate system and dimensions of a rectangular plate**

The basic equation expressing the relationship between the applied pressure and its deflection is represented by [20]:

$$\nabla^4 w = \frac{\partial^4 w}{\partial x^4} + 2 \frac{\partial^4 w}{\partial^2 x \partial^2 y} + \frac{\partial^4 w}{\partial y^4} = \frac{P}{D} \quad (2)$$

where $D =$ flexural rigidity of the plate cross-section $= \frac{Et^3}{12(1-\nu^2)}$.

The boundary conditions for the plate are:

$$w = 0, \frac{\partial w}{\partial y} = 0 \text{ for } x = 0; x = b$$

$$w = 0, \frac{\partial w}{\partial x} = 0 \text{ for } y = 0; y = a$$

For rectangular plates, the maximum resultant displacement at the mid surface is given by [20]:

$$w_{\max} = \frac{16P}{\pi^6 D} \sum_{m=1}^{\infty} \sum_{n=1}^{\infty} \frac{(-1)^{\frac{m+n-1}{2}}}{m n \left[\frac{m^2}{a^2} + \frac{n^2}{b^2} \right]^2} \quad (3)$$

The above equation is a rapidly converging series, and a satisfactory approximation is obtained by considering only the first term of the series provided a/b is small [20]. Therefore, equation (3) reduces to:

$$w_{\max} = \frac{16P}{\pi^6 D} \frac{1}{\left(\frac{1}{a^2} + \frac{1}{b^2} \right)^2} \quad (4)$$

In this study, $a/b = 2.67$ that gives an error of $< 5\%$ [20].

4.1 Stress-Strain Relationship:

In the case of thin plates i.e when the dimension of the body in z direction is small, the problem can be classified as the state of plane stress [21]. This implies that the stress components $\sigma_z = \tau_{xz} = \tau_{yz} = 0$. At room temperature, the stress-strain relationship is given by the expression [21]:

$$\begin{pmatrix} \sigma_x \\ \sigma_y \\ \tau_{xy} \end{pmatrix} = [K] \begin{pmatrix} \varepsilon_x \\ \varepsilon_y \\ \gamma_{xy} \end{pmatrix} \quad (5)$$

$$\text{where } [K] = \frac{E}{1-\nu^2} \begin{pmatrix} 1 & \nu & 0 \\ \nu & 1 & 0 \\ 0 & 0 & \frac{1-\nu}{2} \end{pmatrix}$$

However, if the change in temperature of the surrounding $\Delta T(x,y)$ is considered, equation (5)

$$\text{gets modified as } \sigma = K(\varepsilon - \varepsilon_0), \text{ where } \varepsilon_0 = \begin{pmatrix} \alpha\Delta T \\ \alpha\Delta T \\ 0 \end{pmatrix} [21].$$

It is to be noted that for isotropic materials, the temperature rise results in a uniform principal strain which depends on the coefficient of linear thermal expansion of the material, and therefore there is no thermal component of shear strain.

The standard expressions for stresses based on the thermo-elastic theory are written as [19, 21]:

$$\begin{aligned}
\sigma_x &= -\frac{E}{1-\nu^2} \left[\frac{\partial^2 w}{\partial x^2} + \nu \frac{\partial^2 w}{\partial y^2} \right] - \frac{E \alpha \Delta T}{1-\nu} \\
\sigma_y &= -\frac{E}{1-\nu^2} \left[\frac{\partial^2 w}{\partial y^2} + \nu \frac{\partial^2 w}{\partial x^2} \right] - \frac{E \alpha \Delta T}{1-\nu} \\
\tau_{xy} &= -2G \frac{\partial^2 w}{\partial x \partial y}
\end{aligned} \tag{6}$$

Equation (6) can be used to determine the von Mises stress (σ_{VM}) which is used as a criterion

to predict the onset of failure in the materials. It can be written as: $\sigma_{VM} \leq \sigma_Y$.

where $\sigma_{VM} = \sqrt{I_1^2 - 3I_2}$.

For plane stress, I_1 and I_2 are given by the expressions [21]:

$$\begin{aligned}
I_1 &= \sigma_x + \sigma_y \\
I_2 &= \sigma_x \sigma_y - \tau_{xy}^2
\end{aligned}$$

It has been reported that for rectangular plates with all edges fixed, the maximum stresses occur at the center of the longer sides as given by [8]:

$$(\sigma_x)_{\max} = \beta \frac{Pb^2}{t^2} \tag{7}$$

where β is the coefficient whose value is approximated as 0.5 for a/b ratio > 2 [8].

5. FEM Methodology

The diaphragm was modeled using *SolidWorks* and analysis was performed using *COSMOSWorks*. The diaphragm was held fixed by putting a restraint (along all axes) at the four corner faces as shown in Figure 6. In order for simulation results to be accurate, proper mesh type should be selected and mesh size should be set to as small as possible. We have selected a second order tetrahedral solid element having 10 nodes (4 corner nodes and 1 node

at the middle of each edge) with minimum size ~ 0.075 mm. In total, 9550 elements and 18530 nodes were used for the analysis. The temperature and pressure was varied from 300 – 1000 K, and 0.7 – 7 MPa respectively.

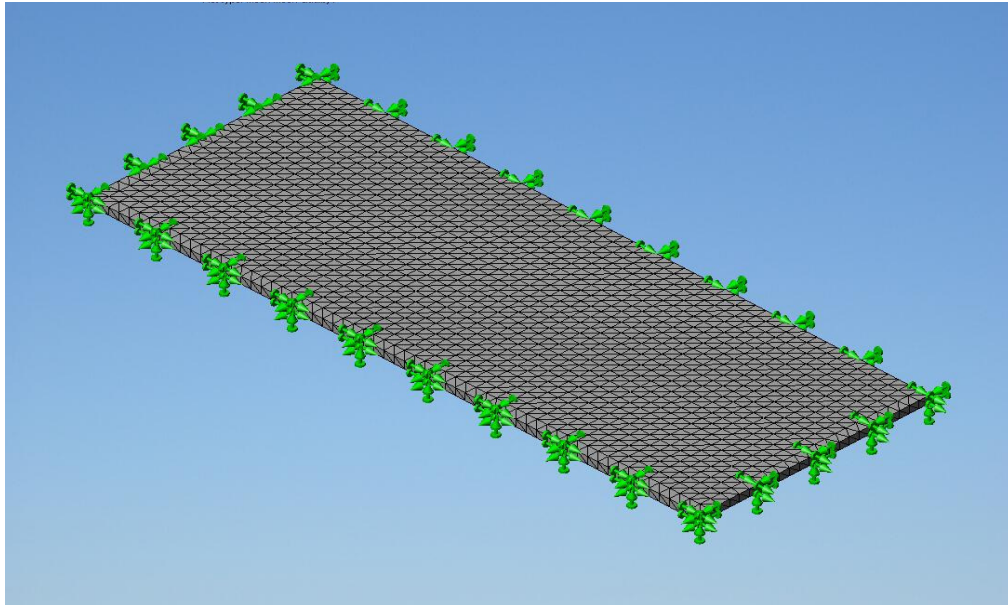
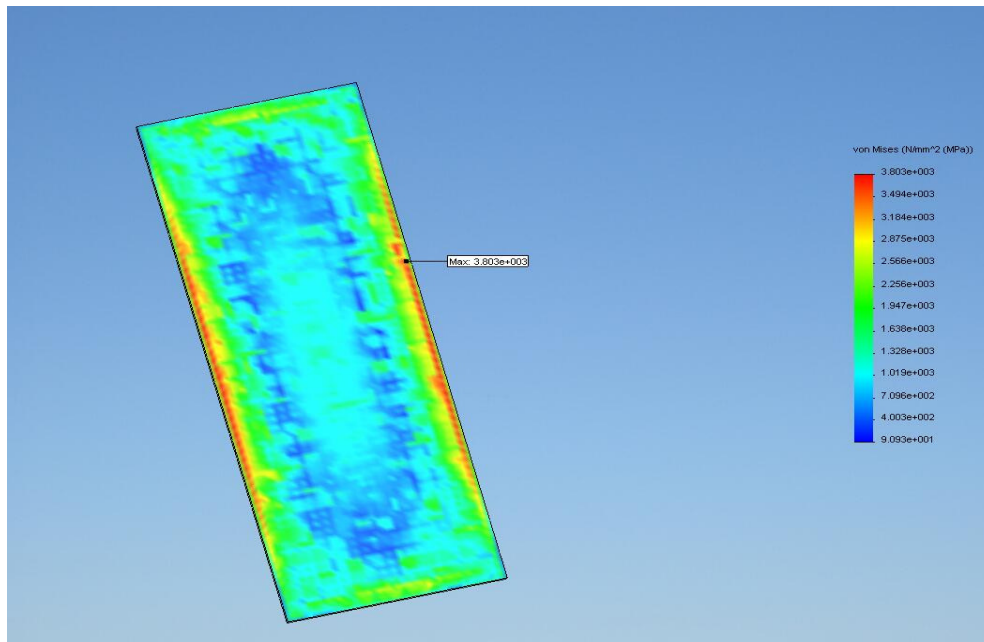


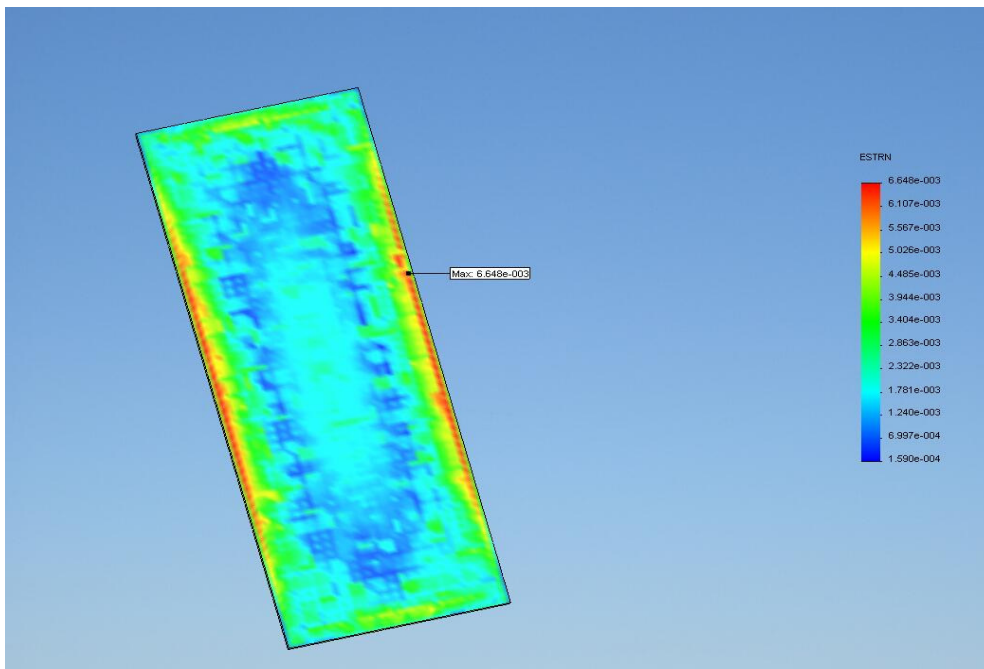
Figure 6: Meshed plot showing restraints at the bottom surface

6. Analysis

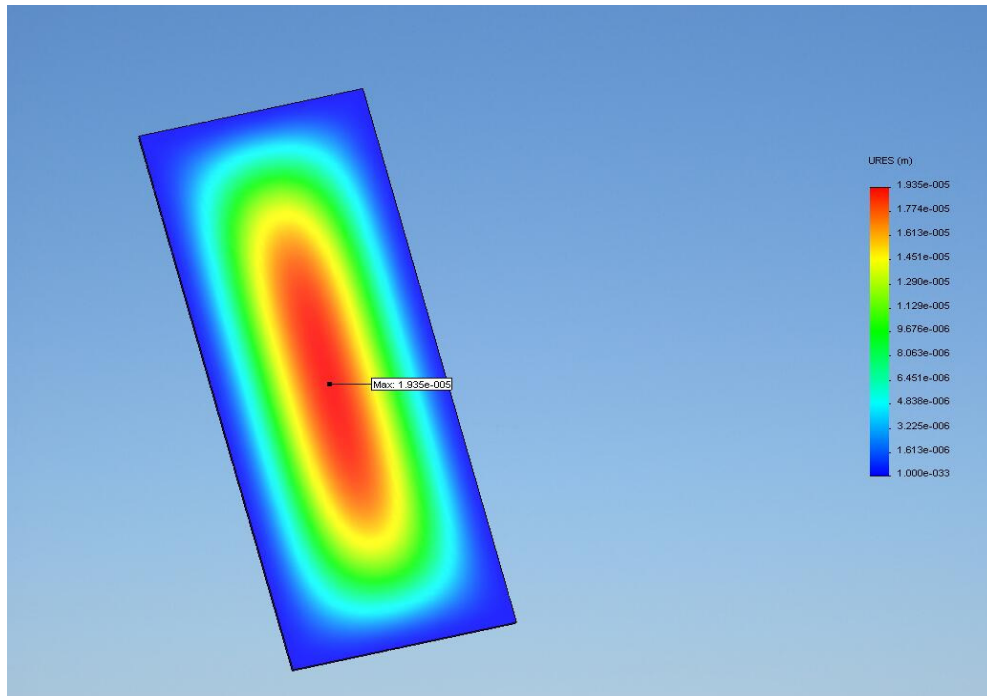
Figures 7a – 7c shows the stress, strain and displacement distribution along the diaphragm (~ 50 μm thick) when a pressure of 7 MPa is applied uniformly along a direction normal to the top face at 1000 K. The analysis shows that the maximum stress or strain occurs along the periphery of the bulging diaphragm, whereas the maximum resultant displacement is maximum at the center (~ 21 μm). However, sensitive piezoresistors should be placed in the areas where stress or strain is large, to obtain maximum efficiency from the sensors. In our analysis, the von Mises stress does not exceed the yield stress, indicating no failure. Figure 8 shows the stress distribution along the longer and shorter edge of the diaphragm.



(a)



(b)

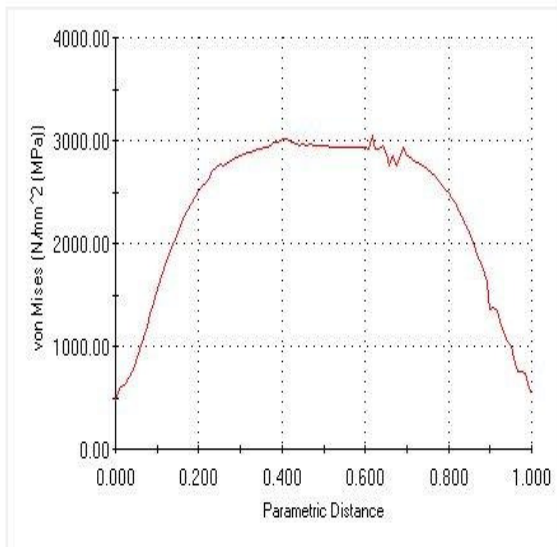


(c)

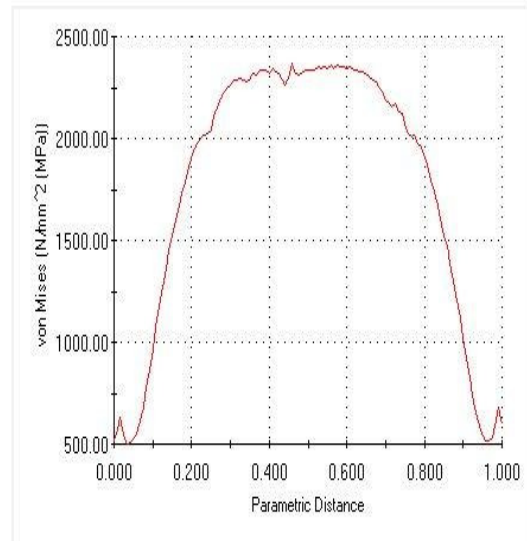
Figure 7: 6H-SiC diaphragm showing a) Stress distribution; b) Strain distribution; and c) displacement distribution

Plot type: Static nodal stress in the mid plane along the longer edge

Plot type: Static nodal stress in the mid plane along the shorter edge



— von Mises [N/mm² (MPa)]



— von Mises [N/mm² (MPa)]

(a)

(b)

Figure 8: Stress distribution in the diaphragm along the a) longer edge; b) shorter edge

In order to check the validity of our analysis, the maximum stresses based on analytical equation (7) were computed and compared with the FEA data at 300 K. The results are shown in Figure 9 and appear to be in good agreement with each other.

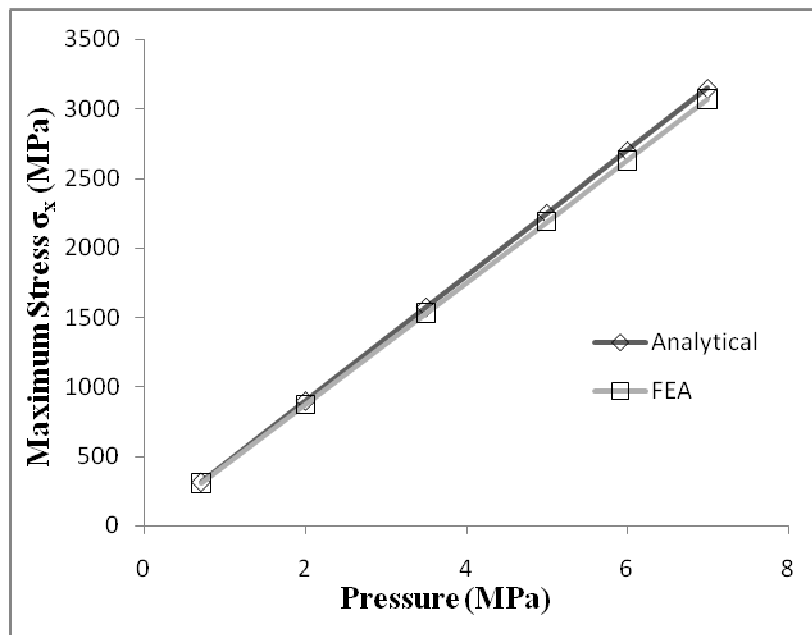
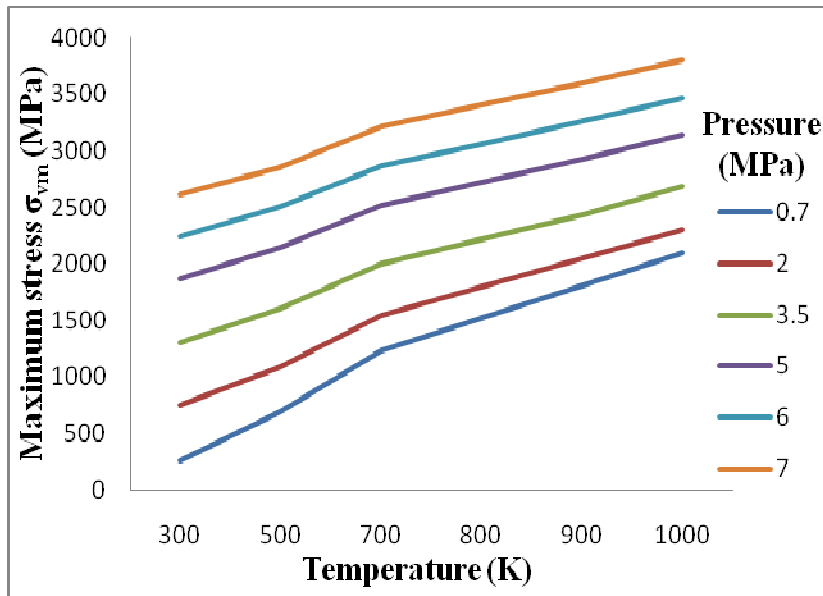


Figure 9: Plot showing comparison of maximum stresses based on equation (6) and FEM data at 300 K

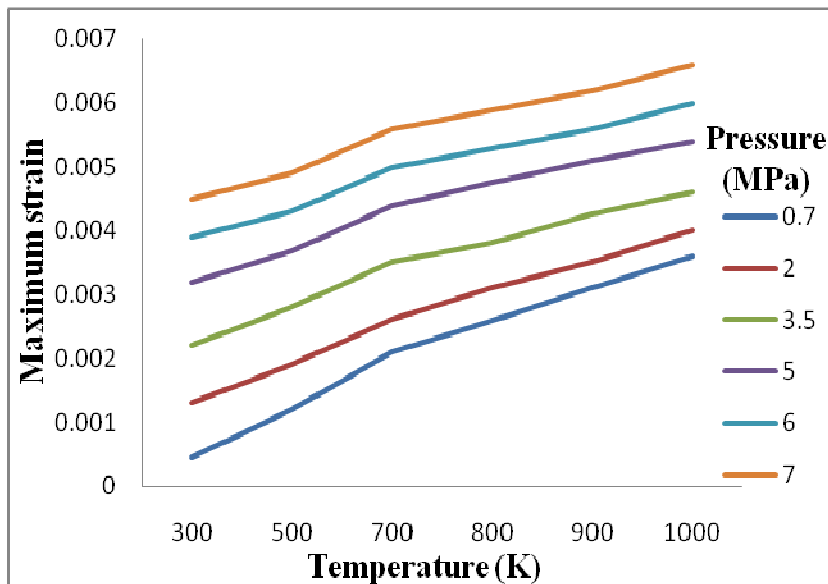
6.1 Effect of Pressure and Temperature

Figures 10a – 10c show the two-dimensional representation of maximum stress, strain and displacement of the 6H-SiC diaphragm with temperature and pressure. It can be observed that the maximum stress and strain increases rapidly with increase in pressure at lower temperatures (< 700 K). At higher temperatures, however, the slope of the curve changes

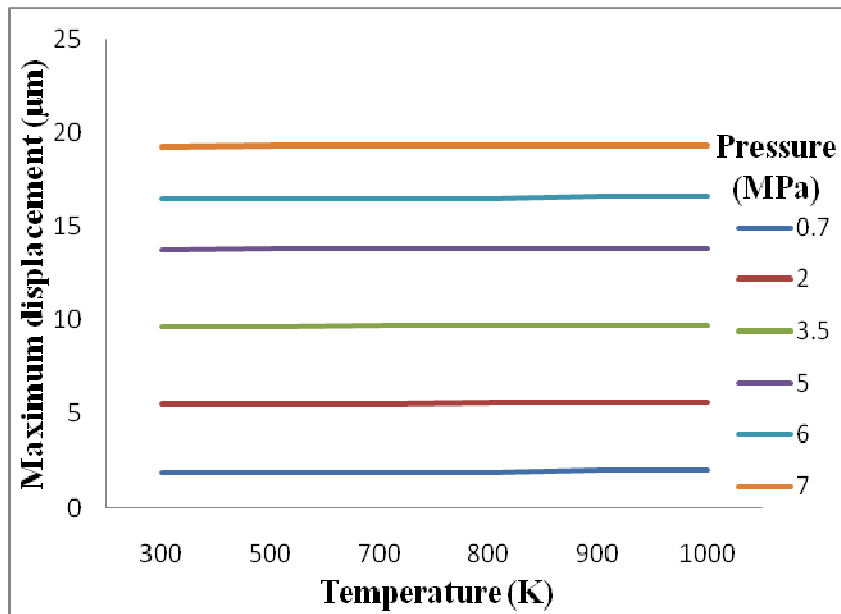
which can be attributed to the dominance of thermal component of stress or strain in equation (6). On the other hand, the resultant maximum displacement shows negligible change due to the temperature effects, and is directly proportional to the applied pressure as given by equation (2) considering 'E' as constant.



(a)



(b)



(c)

Figure 10: Plot showing relationship between a) maximum Von Mises stress; b) maximum strain; and c) maximum displacement with temperature and pressure for 6H-SiC diaphragm.

7. Conclusion

Finite element analysis of single crystal 6H-SiC diaphragm with dimensions 4 mm x 1.5 mm x 0.05 mm was performed for pressures and temperatures ranging from 0.7 to 7 MPa and 300 to 1000 K respectively, to determine the stress, strain and displacement distributions. The maximum von Mises stress was computed as 3.8 GPa which is well below the yield stress, indicating that the diaphragm will not fail by yielding. A distinctive relationship between maximum stress or strain was observed at higher temperatures (> 700 K) whereas the changes in maximum resultant displacement are insignificant due to temperature effects.

Acknowledgement

This material is based in part upon work supported by the National Science Foundation under Grant Number CMMI-0619115. Any opinions, findings, and conclusions or recommendations expressed in this material are those of the authors and do not necessarily reflect the views of the National Science Foundation.

References

- [1] S.M. Sze, ed., *Semiconductor Sensors*, Wiley & Sons, New York, USA (1994).
- [2] S. Maley, R. Romanosky, and Z-Y. Chen, *Sensors and Controls Workshop: Summary Report*, DOE/NETL, November (2001).
- [3] M. Mehregany, C.A. Zorman, N. Rajan, C.H. Wu, "Silicon Carbide MEMS for harsh environments," *Proceedings of the IEEE*, 86 (8), (1998), p. 1594.
- [4] M. Mehregany, C.A. Zorman, "SiC MEMS: opportunities and challenges for applications in harsh environments," *Thin Solid Films*, 355-356, (1999), p. 518.
- [5] A.A. Ned, F. Masheeb, A.D. Kurtz, and G. Beheim, "Leadless SiC Pressure Sensors for High Temperature Applications", 47th International Instrumentation Symposium, Denver, CO (2001).
- [6] A. Ned, A. Kurtz, G. Beheim, F. Masheeb and S.Stefanescu, "Improved SiC Leadless Pressure Sensors for High Temperature, Low and High Pressure Applications," Kulite Semiconductor Products, Inc. Twenty-First Transducer Workshop Lexington, Maryland, June 22-23, (2004).
- [7] Shih-Chin Gong, "Effects of pressure sensor dimensions on process window of membrane thickness", *Sensors and Actuators A* 112 (2004) pp 286–290.

- [8] Tai-Ran Hsu, “MEMS and Microsystems: Design, Manufacture, and Nanoscale Engineering”, 2nd ed. (2008) John Wiley & Sons (NJ, USA), pp. 378-382.
- [9] Z. Dibi, A. Boukabache, P. Pons, “Combined effect of the membrane flatness defect and real dimensions gauges on the sensitivity of a silicon piezoresistive pressure sensor”, Proc. IEEE Sens. 2 (2002) pp 990–993.
- [10] Surface studies with Laser, ed. by F. R. Aussenegg, A. Leitner, M. E. Lippitsch (Springer Series in Chemical Physics, Berlin-Springler 1983).
- [11] I. Ursu, I. N. MihBilescu, A. L. Popa, A. M. Prokhorov, V. P. Ageev, A. A. Gorbunov, V. I. Konov: J. Appl. Phys. 58, (1985) p. 3909.
- [12] Giulio Croce and Paola D’Agaro, “Numerical simulation of roughness effect on microchannel heat transfer and pressure drop in laminar flow”, J. Phys. D: Appl. Phys. 38 (2005) pp 1518–1530.
- [13] Satish G. Kandlikar, Derek Schmitt, Andres L. Carrano and James B. Taylor, “Characterization of surface roughness effects on pressure drop in single-phase flow in minichannels, Physics of Fluids 17, (2005) 100606-1.
- [14] K. Chen, A. Ayon, and S. Spearing, “Controlling and Testing the Fracture Strength of Silicon on the Mesoscale,” Journal of the American Ceramic Society, Vol. 83, No. 6, (2000) pp. 1476-84.
- [15] Ling Yin, Eric Y. J. Vancoille, Kuppuswamy Ramesh and Han Huang, Int. J. Machine Tools and Manufacture, Vol. 44 (2004) pp 607-615.

- [16] Tairov, Yu.M., V.F. Tsvetkov, in *Handbook on Electrotechnical Materials* Eds. Koritskii, Yu.V., V.V. Pasynkov, B.M. Tareev, **Vol.3**, Sec.19, "Semiconductor Compounds A^{IV} B^{IV}", Energomashizdat, Leningrad, 1988, pp 446-471.
- [17] *Properties of Advanced Semiconductor Materials*, ed. by M.E. Levinshtein, S.L. Rumyantsev, M.S. Shur (John Wiley and Sons, New York 2001).
- [18] Kurt E. Petersen, "Silicon as a Mechanical Material", Proc. IEEE Vol. 70 (5), 1982 p 420.
- [19] E. Suhir, *Structural Analysis in Microelectronic and Fiber-Optic Systems, Volume I*, Van Nostrand Reinhold (1991).
- [20] S. Timoshenko and S. Woinosky-Krieger, *Theory of Plates and Shells*, McGraw Hill Classic Textbook Reissue (1987).
- [21] *Introduction to Finite Elements in Engineering*, T. R. Chandrupatla and A. D. Belegundu, 3rd ed. (Prentice Hall, New Jersey, 2002).

CHAPTER 6 GENERAL CONCLUSION

The systematic investigations revealed that single crystal SiC is an excellent material to be used in high-temperature MEMS pressure sensors. Pulsed laser micromachining offers several benefits over traditional microfabrication methods for difficult to fabricate materials. The accuracy of the micromachined features is greatly related to the laser wavelength and pulse width. A study of the laser ablation behavior is very important in determining the optimum processing parameters. The study demonstrated that pulsed laser micromachining occupies a unique position as a microfabrication technique offering higher etch rates, better quality of micromachined features (controlled diaphragm thickness, profile), and process flexibility with respect to changes in design.